

EFFECTS OF CRACK-CRYSTALLITE INTERACTION  
ON THE FRACTURE BEHAVIOR OF A CORDIERITE GLASS-CERAMIC

by

Robert M. Morena

Dissertation submitted to the Faculty of the  
Virginia Polytechnic Institute and State University  
in partial fulfillment of the requirements for the degree of  
DOCTOR OF PHILOSOPHY  
in  
Materials Engineering Science

APPROVED:

\_\_\_\_\_  
D. P. ~~H~~ Hasselman, Chairman

\_\_\_\_\_  
J. J. ~~B~~ Brown, Jr., Co-Chairman

\_\_\_\_\_  
N. S. ~~E~~ Eiss, Jr.

\_\_\_\_\_  
G. V. Gibbs

\_\_\_\_\_  
W. R. Hibbard, Jr.

\_\_\_\_\_  
K. Niihara

March, 1982  
Blacksburg, Virginia

## ACKNOWLEDGMENTS

1. I wish to thank my chairman, Professor D. P. H. Hasselman, for the assistance and cooperation he has extended me. Dr. Hasselman's many insights into the fracture behavior of brittle materials proved invaluable in this research effort.

2. My thanks, also, to my co-advisor, Professor J. J. Brown, Jr. for his valuable experimental suggestions regarding heat-treatment, quantitative microscopy, etc. Appreciation is also expressed to both Professors Hasselman and Brown, as well as to the other members of my committee, Dr. N. S. Eiss, Jr., Dr. G. V. Gibbs, Dr. W. R. Hibbard, Jr., and Dr. K. Niihara, for the considerable time and effort which each has expended in serving on my Graduate Committee.

3. During the course of this research, financial support has been received by me from a variety of sources including a graduate teaching assistantship, a Pratt Presidential Fellowship, a Virginia Mining and Mineral Resources Research Institute Fellowship, and graduate student fee waivers. I wish to gratefully acknowledge all those who made this support possible, with special mention given to Dr. J. J. Brown.

4. I would like to draw special attention to the following:

a. My wife, Marie Bryhan, for proof-reading this Dissertation, and more important, for showing me that indeed the robin does have two songs ("cheerio-cheerio", and "hey-baby, hey-baby").

- b. Suresh Baskaran, Janice Corr, and Karl Wiedemann, for assistance with the tedious job of sample polishing.
- c. Larry Bentsen and Anuradha Venkateswaran, for many helpful and supportive discussions.
- d. Koichi Niihara, for stimulating talks on everything from fracture mechanics to the Japanese predilection for scalding baths.
- e. Dr. J. L. Lytton, for assistance in keeping an always-quarrelsome SEM in operating condition.
- f. The secretarial staff of the Materials Engineering Department, especially Barbara Johnson and Jeanne Warner, for the many favors done me.

5. Finally, this Dissertation is dedicated to Dr. H. T. Smyth, Department of Ceramics, Rutgers University, whose several undergraduate courses in glass science and phase equilibria first introduced me to the broader horizons of ceramic engineering.

TABLE OF CONTENTS

	<u>Page</u>
ACKNOWLEDGMENTS . . . . .	ii
LIST OF FIGURES . . . . .	vii
LIST OF TABLES . . . . .	x
I. BACKGROUND . . . . .	1
A. Introduction and Overall Objective . . . . .	1
B. Mechanical Behavior of Brittle Materials . . . . .	2
C. Crack-Crystallite Interactions: Influence of Stress Concentration . . . . .	9
D. Crack-Crystallite Interactions: Effects Which Interfere with Crack Propagation . . . . .	18
E. Crack-Crystallite Interactions: The Flaw Introduction Process . . . . .	22
F. Indentation Fracture in Brittle Materials . . . . .	26
G. The Glass-Ceramic Process . . . . .	37
H. Objectives of the Research Program . . . . .	45
II. EXPERIMENTAL PROCEDURE . . . . .	47
A. Sample Preparation and Preliminary Characteriza- tion . . . . .	47
1. Material . . . . .	47
2. Sample Geometry and Heat-Treatment . . . . .	49
3. Sample Polishing . . . . .	50
4. Quantitative Microscopy . . . . .	51
5. Phase Identification . . . . .	55
6. Bulk Density . . . . .	55
7. Young's Modulus . . . . .	56
B. Surface Damage . . . . .	56
1. Introduction and Measurement of Surface Damage . . . . .	56
2. Strength Behavior . . . . .	59

TABLE OF CONTENTS (CONT'D)

	<u>Page</u>
III. EXPERIMENTAL RESULTS . . . . .	64
A. Preliminary Characterization . . . . .	64
1. Phase Identification and Microstructural Analysis . . . . .	64
2. Young's Modulus and Bulk Density . . . . .	68
3. Quantitative Microscopy . . . . .	70
B. Surface Damage . . . . .	72
1. Effect of Experimental Method on Measured Crack Size . . . . .	72
2. Indentation Parameters for the Original Glass and Samples with the Fine- Precipitate Microstructure . . . . .	78
3. Indentation Parameters for Samples with the Large-Crystallite Microstructure . . . . .	83
4. Crack-Crystallite Interaction in the Transition Region . . . . .	95
5. Fracture Toughness - Standard Test Samples . .	98
6. Fracture Toughness of the Cordierite Glass- Ceramic . . . . .	103
7. Strength Behavior . . . . .	112
8. Vicker's Hardness: Effect of Heat-Treatment . .	120
IV. DISCUSSION . . . . .	123
A. Crack Pinning . . . . .	123
B. Toughening in the Composite Regime . . . . .	125
C. Strength Behavior . . . . .	129
1. Effect of Crystallization . . . . .	129
2. The Constant Strength Region for the Large- Crystallite Samples . . . . .	131
3. The Slope of the Strength Loss Curve . . . . .	137
D. Comments on Measurement of Fracture Toughness of Brittle Materials . . . . .	140
E. Residual Stress Effects and the Determination of Fracture Toughness by the Indentation Method . . . . .	141

TABLE OF CONTENTS (CONT'D)

	<u>Page</u>
F. Crystallization Effects on Vicker's Hardness . . . . .	145
G. Microstructural Design for Optimal Resistance to Surface Damage . . . . .	146
H. Suggestions for Future Work . . . . .	148
V. CONCLUSIONS . . . . .	150
VI. LITERATURE CITED . . . . .	152
VITA . . . . .	160
ABSTRACT	

## LIST OF FIGURES

		<u>Page</u>
Figure 1.	Schematic illustration of deformation fields during indenter contact in elastic-plastic indentation model (adapted from ref. 57) . . . . .	29
Figure 2.	Location of tensile fields (darkened regions) during indentation loading cycle (adapted from ref. 49) . . . . .	30
Figure 3.	Top and cross-sectional views around Vicker's indent assuming: a, median cracks; and b, Palmqvist cracks. The plastic zone appears as the stippled region . . . . .	31
Figure 4.	Nucleation and crystallization rates for a glass-ceramic as functions of temperature . . . . .	43
Figure 5.	Measurement of free path distances for mean free path determination using radial grid technique . . . . .	54
Figure 6.	Biaxial flexure apparatus used to determine strength . . . . .	60
Figure 7.	Electron micrographs of cordierite glass ceramic initially heat-treated at 820°C for 2h followed by further treatment at a, 905°C for 8h; b, 1200°C for 8h; c, 1100°C for 1h; and d, 1100°C for 2h . . . . .	67
Figure 8.	SEM micrographs showing indentation cracks for cordierite glass-ceramic for: a, original glass; and b, specimen heat-treated at 820°C/2h plus 1000°C/8h . . . . .	79
Figure 9.	Crack size as a function of indenter load for cordierite glass-ceramic for: a, original glass; and specimens heat-treated at b, 820°C/2h and 820°C/2h plus 905°C/8h; c, 820°C/2h plus 1000°C/8h (strength series); and d, 820°C/2h plus 1000°C/8h and 820°C/2h plus 1100°C/1h . . . . .	82
Figure 10.	SEM micrographs of cordierite glass-ceramic heat-treated at 820°C/2h plus 1150°C/8h showing indentation crack at indenter load of: a, 75g; b, 100g; c, 500g; and d, 1000g . . . . .	87

LIST OF FIGURES (CONT'D)

	<u>Page</u>
Figure 11. Crack size as a function of indenter load for cordierite glass-ceramic given an initial heat-treatment of 820°C/2h followed by further treatment at: a, 1100°C/2h; b, 1100°C/8h; c, 1150°C/8h; d, 1150°C/8h (strength series); e, 1200°C/8h (strength series); and f, 1260°C/8h (strength series) . . . . .	89
Figure 12. Frequency histogram of crack size for cordierite glass-ceramic heat-treated at 820°C/2h plus 1150°C/8h for indenter loads of 50, 125, and 1000g. The 125g. load for this sample corresponds to the start of the transition region . . . . .	94
Figure 13. SEM micrographs of crack-crystallite pinning in the transition region for cordierite glass-ceramic heat-treated at 820°C/2h followed by subsequent heat-treatment at: a and b, 1100°C/8h; and c and d, 1200°C/8h . . . . .	96
Figure 14. Explanation for decreasing Palmqvist crack size occurring with increasing indentation load in the transition region for the large-crystallite cordierite glass-ceramic samples: a, median crack size and half-diagonal length as functions of load for 820°C/2h plus 1150°C/8h sample; and b, schematic showing effect of pinning on Palmqvist crack size, $\ell$ . . . . .	97
Figure 15. Average number of crystallites intercepted before pinning commences as a function of crystallite size for cordierite glass-ceramic samples displaying a transition region . . . . .	100
Figure 16. Fracture toughness in the high-load regime for the large-crystallite samples of the cordierite glass-ceramic as a function of: a, mean free path; and b, average crystallite size for the dispersed phase . . . . .	111

LIST OF FIGURES (CONT'D)

	<u>Page</u>
Figure 17. Fracture toughness of cordierite glass-ceramic for original glass and samples heat-treated for 8h at indicated temperatures following initial heat-treatment at 820°C/2h . . . . .	113
Figure 18. Average fracture toughness as a function of indenter load for cordierite glass-ceramic heat-treated at 820°C/2h plus 1260°C/8h . . . . .	114
Figure 19. Fracture stress as a function of indenter load for the cordierite glass-ceramic for: a, original glass; and samples heat-treated at 820°C/2h followed by 8 hour growth treatment at: a, 1000°C; b, 1150°C; c, 1200°C; and d, 1260°C . . . . .	117
Figure 20. SEM micrographs of fracture surfaces of the cordierite glass-ceramic for: a, the original glass; and b, a sample heat-treated at 820°C/2h plus 1260°C/8h . . . . .	130
Figure 21. Schematic of fracture stress-load relation for material with dual-regime fracture toughness: a, initial flaw size model; and b, stable crack growth model . . . . .	136

LIST OF TABLES

		<u>Page</u>
TABLE I.	Internal Stresses Present in a Two-Phase Composite After Cooling . . . . .	11
TABLE II.	Young's Modulus and Bulk Density for Various Heat-Treatments of Cordierite Glass-Ceramic . . . . .	69
TABLE III.	Microstructural Parameters of Dispersed Phase for Various Crystallization Heat-Treatments of Cordierite Glass-Ceramic . . . . .	71
TABLE IV.	Effect of Etching Time in 5% HF on Size of Indent Cracks in Original Glass of Cordierite Glass-Ceramic . . . . .	73
TABLE V.	Effect of Post-Indentation Time on Size of Indent Cracks in Original Glass of Cordierite Glass-Ceramic . . . . .	75
TABLE VI.	Experimental Indentation Data for Cordierite Glass-Ceramic for the Original Glass and the Fine-Precipitate Samples . . . . .	80
TABLE VII.	Linear Regression Analysis of Palmqvist Crack Size as a Function of Load for Cordierite Glass-Ceramic for the Original Glass and the Fine-Precipitate Samples . . . . .	84
TABLE VIII.	Experimental Indentation Data for Cordierite Glass-Ceramic for the Large-Crystallite Samples . . . . .	85
TABLE IX.	Linear Regression Analysis of Palmqvist Crack Size as a Function of Load for Cordierite Glass-Ceramic for the Large-Crystallite Samples . . . . .	93
TABLE X.	Indentation Parameters Across the Transition Region for the Large-Crystallite Samples of Cordierite Glass-Ceramic . . . . .	99
TABLE XI.	Indentation Parameters and Fracture Toughness Values for Soda-Lime-Silica Glass . . . . .	102

LIST OF TABLES (CONT'D)

	<u>Page</u>
TABLE XII. Comparison of Fracture Toughness Round-Robin Results on Commercially Heat-Treated Cordierite Glass-Ceramic . . . .	104
TABLE XIII. Fracture Toughness Values for Cordierite Glass-Ceramic . . . . .	106
TABLE XIV. Toughness and Microstructure Data for the Large-Crystallite Samples of the Cordierite Glass-Ceramic . . . . .	110
TABLE XV. Strength Values as Function of Indenta- tion Load for Original Glass and Crystallized Samples of Cordierite Glass-Ceramic . . . . .	115
TABLE XVI. Linear Regression Analysis of Strength- Load Behavior for Original Glass and Crystallized Samples of Cordierite Glass-Ceramic . . . . .	119
TABLE XVII. Vicker's Hardness Value at 1000 Grams for Cordierite Glass-Ceramic . . . . .	121
TABLE XVIII. Examination of Various Toughness Models Appropriate to Brittle Composites . . . . .	126
TABLE XIX. Calculated Residual Stress Effects on Crack Size for Two Samples of the Cordierite Glass- Ceramic . . . . .	134
TABLE XX. Comparison of Fracture Toughness Values Calculated for Several Samples of Cordie- rite Glass-Ceramic . . . . .	143

## I. BACKGROUND

### A. Introduction and Overall Objectives

In response to rising technological demands, a host of new ceramic materials have been developed for many applications (such as cutting tools or turbine blades), where previously the use of brittle materials was not even contemplated. Many of these new materials are actually composite structures in that they consist of dispersed crystalline particles bonded together by either a glassy or fine-grained crystalline matrix.

Composites often will exhibit thermal, mechanical, and electrical properties quite different from, and frequently superior to, the single phase materials from which they were fabricated. Because of the microstructural complexity of many composites, model structures have frequently been selected as suitable materials to investigate the effect of microstructure and other composite variables on properties relevant to the new applications. One type of model ceramic composite includes glass-crystal composites which may be made either by the vacuum hot-pressing of glass and crystalline powders, or by the glass-ceramic process in which a glass is made to undergo controlled crystallization by careful time-temperature heat-treatment.

It is perhaps with the study of mechanical properties that the use of these various types of glass-crystal composites as model structures has received the most emphasis. A considerable amount of data (which will be discussed in the succeeding Sections) indicate, in general, that the mechanical performance of glass-crystal composites

is vastly superior to that of the base glass which serves as the matrix. Two examples, among many, will serve to illustrate this contention:

(i) The bending strengths of silicate glasses following a standard surface treatment is not especially composition-sensitive and is given by McMillan (1) as  $55-70 \text{ MNm}^{-2}$ ; following controlled crystallization, strength values in excess of  $100 \text{ MNm}^{-2}$  (and in several instances greater than  $250 \text{ MNm}^{-2}$ ) may be typically realized for a large group of glass-ceramic systems (1).

(ii) Strength loss following surface damage is a characteristic feature of ceramic materials, however, strength decreases following abrasion were found to be nearly three times as great on a relative basis for a glass than for its glass-ceramic counterpart (2).

These examples strongly suggest that the addition of dispersed particles to a previously homogeneous brittle material interferes with, and strongly impedes, the flaw introduction and propagation processes typical of all brittle materials. It will be the general intent of this Dissertation to investigate the nature of the flaw-dispersed phase interaction in a model brittle matrix-particulate composite, specifically a glass-ceramic.

## B. Mechanical Behavior of Brittle Materials

Before any consideration may be given of the role played by the dispersed phase in influencing the mechanical properties of glass-ceramics and other brittle composites, a general treatment of the mechanical behavior of brittle materials is appropriate. Glass-ceram-

ics, as well as glasses and conventional polycrystalline ceramic materials, behave in a brittle fashion at room temperature because completely linear and essentially recoverable stress-strain behavior to fracture is manifested in macroscopic loading situations. This behavior is in marked contrast to that of most metal systems where slip-related, ductile processes constitute a major, large scale energy-absorbing mechanism that serves to initiate non-recoverable, permanent deformation during load application.

Closely associated with this concept of brittleness is the extreme flaw sensitivity of ceramic materials, that is, their vulnerability to sudden failure arising from stress concentrations occurring at defect sites introduced in the material by, among other ways, seemingly insignificant surface contact. It is this extreme flaw sensitivity that is responsible for the poor resistance to impact and sudden temperature changes exhibited by ceramic materials. Additionally, the presence of these flaws and their subsequent evolution into well-defined, propagating cracks upon imposition of a tensile stress is widely believed to account for observed strengths of brittle materials that are 3 to 4 full orders of magnitude lower than values calculated from bond strength-based theoretical considerations.

Inglis (3) was the first to demonstrate that stress concentrations associated with crack tip geometry may result in local levels of stress which can be substantially higher than the global value of stress applied to the material. For an elliptical, two dimensional crack oriented with its major axis normal to the direction of applied

tensile stress, Inglis obtained the following expression for the stress,  $\sigma_{\max}$ , developed at the crack tip:

$$\sigma_{\max} = \sigma_{\text{appl}} [1 + 2(c/\rho_t)^{\frac{1}{2}}] \quad (\text{I-1})$$

where  $\sigma_{\text{appl}}$  is the applied stress,  $c$  is the half-length of the crack's major axis, and  $\rho_t$  is the radius of curvature at the crack tip. Since  $c > \rho_t$  for an elliptical configuration, the multiplier or stress concentration effect from the bracketed term will cause the theoretical fracture stress to be reached locally at the crack tip, well before  $\sigma_{\text{appl}}$  reaches this value.

Drawing on Inglis' crack tip model, Griffith (4) speculated that a brittle material contains an inherent population of fine cracks. Using an energy balance approach to analyze fracture processes, Griffith expressed the total potential energy of a system under stress and containing cracks as the sum of two opposing effects: elastic strain energy, which provides the driving force for crack propagation, and the thermodynamic surface energy, which is the work required to create a new unit of crack surface area.

Using this energy approach, Griffith postulated that cracks will start to propagate when an incremental increase in crack length lowers the potential energy of the system. For a two-dimensional, semi-elliptical edge crack, located in a thick plate of infinite extent, and oriented with its long dimension normal to the direction of a uniformly-applied tensile stress, Griffith showed that crack propagation will commence when the applied tensile stress is equal to  $\sigma_f$ ,

the critical tensile stress required for failure:

$$\sigma_f = \left( \frac{2E\gamma_s}{(1-\nu^2)\pi c} \right)^{1/2} \quad (\text{I-2})$$

where E is Young's modulus,  $\gamma_s$  is the surface free energy,  $\nu$  is Poisson's ratio, and c is the crack size. Equation I-2, known as the Griffith criterion for fracture, can be made applicable to other flaw configurations by inclusion of a suitable geometric factor.

In his analysis, Griffith assumed that the creation of new surface was the only energy-dissipating process occurring during fracture. However, calculation of surface energy from Eq. I-2, using strength values obtained on various brittle materials with flaws of known size, indicates that  $\gamma_s$  considerably underestimates the value of fracture stress needed to satisfy the Griffith expression (5). Orowan (5) suggested that energy-dissipation processes other than surface formation can be operative during fracture, and, in the case of ductile metals, proposed the addition of a plastic flow term to the surface free energy to account for the additional strain energy absorption. The modified fracture energy term arrived at by Orowan has been termed the effective fracture energy,  $\gamma_{\text{eff}}$ , and is generally used in place of  $\gamma_s$  in the Griffith expression. Other contributions to fracture energy have also been recognized. Hasselman et al. (6) have summarized these various mechanisms as follows:

$$\gamma_{\text{eff}} = K\gamma_s + \gamma_p + \gamma_n + \gamma_{el} \quad (\text{I-3})$$

where  $K$  is the surface roughness coefficient (which equals unity for totally-planar crack propagation),  $\gamma_p$  and  $\gamma_n$  are the energies expended, respectively, by plastic and viscous flow, and  $\gamma_{el}$  represents non-recoverable elastic strain energy, such as evolved in acoustic emission.

Further insight into crack tip-related behavior was provided by Irwin (7) who, for a crack geometry and configuration similar to that employed by Inglis, defined a stress intensity factor,  $K_I$  (the subscript indicates the crack opening or tensile mode of propagation), such that

$$K_I = \sigma_{app} (\pi c)^{\frac{1}{2}} \quad (I-4)$$

Irwin used this parameter to designate the local stress level,  $\sigma_r$ , at a distance  $r$  directly ahead of the crack tip:

$$\sigma_r = K_I / (2r)^{\frac{1}{2}} \quad (I-5)$$

When the applied stress value has attained the level of the fracture stress,  $\sigma_f$ , at the onset of spontaneous or catastrophic crack growth, the stress intensity factor also reaches a critical or upper value,  $K_{Ic}$ , which is called the critical stress intensity factor or the fracture toughness. This term, believed to be a material property, is extremely important from a fracture standpoint since, from Eq. I-5, it defines the level of applied stress needed to initiate spontaneous fracture or critical crack propagation. At applied stress levels below the fracture stress such that  $K_I < K_{Ic}$ , only stable crack

propagation occurs since the elastic strain energy supplied to the crack tip is insufficient to overcome the energy barrier to catastrophic failure. Fracture toughness thus serves as an indicator of a material's resistance to unstable crack extension. At the onset of critical crack propagation where  $K_I = K_{Ic}$  and  $\sigma_{\text{appl}} = \sigma_f$ , comparison of Equations I-2 and I-4 yields:

$$K_{Ic} = (2 \gamma_{\text{eff}} E / (1 - \nu^2))^{\frac{1}{2}} \quad (\text{I-6})$$

$$\sigma_f = K_{Ic} / Y \sqrt{c} \quad (\text{I-7})$$

where  $Y$  is a geometric constant for a given crack configuration and orientation (8). Equation I-7 is referred to as the Griffith-Irwin expression.

With this brief theoretical introduction on the fracture mechanics of brittle materials, it is possible to outline in a general manner how the strength of brittle composites may be affected by the dispersed phase. Equations I-6 and I-7 indicate that the fracture strength of a brittle material is determined both by the material's resistance to critical crack propagation as represented in the  $\gamma_{\text{eff}}$  (or  $K_{Ic}$ ) term, and the flaw size,  $c$ . Both of these factors may be altered by interaction of the crack with the dispersed phase.

One general way in which the dispersed phase can increase strength in a brittle composite is, as seen in Eq. I-3, for inclusions to increase the amount of strain energy needed to create a new unit of crack surface. In ceramics at room temperature, the major strain energy sink is the combined surface roughness/surface energy effect,

$K_{Y_s}$ . Surface roughness is manifested by non-planar or mixed-mode crack propagation, a phenomenon quite likely to be missing in glasses or fine-grained, single phase polycrystalline structures. However, with the introduction of a dispersed phase to these materials, a variety of different surface roughness effects become possible such as bowing, branching and deflection of cracks about the second phase inclusions. The resulting increase in fracture surface energy can, quite likely, result in strength increases.

The dispersed phase can also work towards limiting the size of flaws present in the composite. Flaws may be grouped into two general categories: extrinsic (introduced from surface damage caused by handling, machining, particle impact, or other forms of surface contact), and intrinsic (due to weak grain boundaries, cleavage cracks, or microcracking from local stress concentrations). Of these two types, extrinsic flaws will generally be the most severe. The presence of a dispersed phase with an intrinsically greater fracture toughness than that of the matrix (as is typical of most glass-crystal composites), could conceivably act to limit the size of any flaws introduced during surface damage by acting as an impenetrable barrier to flaws.

The introduction of a dispersed phase to a previously-uniform brittle material typically results in a strength increase, implying that the second phase particles must, in some manner, interfere with the two crack-related parameters in the Griffith-Irwin expression, namely resistance to crack extension and size of flaws. Extensive documentation exists (as will be discussed in the next several

Sections) to demonstrate that these changes in crack introduction and propagation behavior are a direct result of crack-crystallite interaction. These various types of interactions may be grouped into three general categories:

- (i) effects which influence the stress concentration at the crack tip.
- (ii) effects which govern the nature of crack propagation.
- (iii) effects which control the sizes of the initial flaws.

#### C. Crack-Crystallite Interactions: Influence of Stress Concentration

Included in this category are effects such as internal or residual stress and micromechanical stress concentration, which arise respectively, from mismatch in thermal expansion coefficient or elastic modulus between matrix and inclusion. By influencing the level of localized stress in the crack tip region, these mismatch effects control the conditions for catastrophic failure.

Internal or residual stresses are present to some extent in all multiphase materials and originate from differences in thermal expansion coefficient occurring between the various phases as the composite is cooled from its fabrication or use temperature. The stress state after cooling was first described by Weyl (9) and later modified by Selsing (10). For a spherical inclusion of radius  $R$ , the following expressions are obtained for the hydrostatic stress,  $\sigma$ , existing in the particle and the radial,  $\sigma_{rr}$ , and tangential,  $\sigma_{\theta\theta}$ , stress

components developed in the matrix at a distance  $r$  from the center of the particle:

$$\frac{\text{Particle}}{\sigma = P} \quad (\text{I-8})$$

$$\frac{\text{Matrix}}{\sigma_{rr} = -2\sigma_{\theta\theta} = P \left(\frac{R}{r}\right)^3} \quad (\text{I-9})$$

with

$$P = \frac{(\alpha_p - \alpha_m)\Delta T}{\frac{1+\nu_m}{2E_m} + \frac{1-2\nu_p}{2E_p}} \quad (\text{I-10})$$

where  $\alpha$  is the thermal expansion coefficient,  $\Delta T$  is the temperature range during cooling over which stress relaxation cannot occur,  $\nu$  is Poisson's ratio, and  $E$  is Young's modulus. The subscripts  $p$  and  $m$  refer, respectively, to the second phase inclusion and the matrix. The term  $(\alpha_p - \alpha_m)$  will be referred to in subsequent discussion as the expansion mismatch. It can be seen from Eq. I-9 that the residual stress components of the matrix are highly-localized and have a maximum value at the particle-matrix interface that then decays quite rapidly with distance outward from the particle surface.

The various stress conditions in the matrix and the inclusion are listed in Table I for both high expansion and low expansion dispersed phases. Note that regardless of whether the included particle has a thermal expansion coefficient higher or lower than that of the matrix, some component of matrix stress will always be tensile.

TABLE I. INTERNAL STRESSES PRESENT IN A TWO-PHASE  
COMPOSITE AFTER COOLING

Condition	Stress State		
	Particle	Matrix	
		$\sigma_{rr}$	$\sigma_{\theta\theta}$
$\alpha_p > \alpha_m$	Tension	Tension	Compression
$\alpha_p < \alpha_m$	Compression	Compression	Tension

The presence of a tensile internal stress state for the matrix regardless of sign of the mismatch suggests that the presence of residual stresses would be expected to have a detrimental effect on strength. Khaund et al. (11) have shown that localized stress concentrations such as from expansion mismatch will increase the crack tip stress intensity factor and so result in a lowering of the applied stress level needed to initiate catastrophic failure.

This presumed detrimental role for residual stresses is, however, not totally supported by literature data on brittle composites. In a classic study of the effect of thermal expansion mismatch, Binns (12) measured the tensile strength of a series of hot-pressed glass-particulate composites consisting of three different particle size fractions of either alumina or zircon as the dispersed phase. By choosing a particular glass as the matrix phase, a specific value of thermal expansion mismatch between matrix and inclusion could be engineered in the composite. Binns' data for alumina as the dispersed phase are the more extensive of the two composite series. Examination of this work shows that at constant volume fraction of dispersed phase, composites made from either the fine or the intermediate alumina fractions (10  $\mu\text{m}$  and 45  $\mu\text{m}$ , respectively) all had strength values above that of the base glass, regardless of the sign or magnitude of the expansion mismatch. Only with the largest particle size for the alumina (180  $\mu\text{m}$ ), where microcracking about inclusions was observed, were strength values obtained which were lower than that for the matrix glass without inclusions. For this latter series, strength

was a maximum (but still below that of the base glass) when no mismatch occurred, and then decreased with increasing degree of mismatch regardless of sign of mismatch. Results similar to Binns' were reported by Frey and Mackenzie (13) for a nearly identical series of glass-alumina composites. For a single dispersed particle size of 120-150  $\mu\text{m}$ , strength values above that of the base glass were obtained regardless of sign or magnitude of expansion mismatch. Only for the single composite where microcracking was observed did strength values fall below that of the base glass. The role of microcracking will be considered in more detail later in this Section.

Substantial strength increases as a result of thermal expansion mismatch associated with the crystallization of a high-expansion phase from a  $\text{Li}_2\text{O-SiO}_2$  glass have been reported by Borom et al. (14). For this particular system with mismatch  $\alpha_p > \alpha_m$ , residual stresses might well be expected to have a beneficial effect on strength despite the tensile character of the radial component of internal stress around the inclusions. Erdogan (15) has shown that the influence exerted on crack behavior by any localized stress field around inclusions is determined by the flaw size-to-particle size ratio. In the fine-grained glass-ceramic samples of Borom et al., the ratio would be expected to be quite large. As a consequence, only a relatively small segment of crack front would be subjected to internal stress effects, so any strength-degrading role for expansion mismatch stress would be negligible. Given, then, the principle of mechanical equilibrium

(which states that in the absence of an external stress, the volume integral of all stresses in a body must be zero), the hydrostatic stress state in the crystallites created by the expansion mismatch would require that the average stress for the matrix be compressive. This result, which forms the basis of the "pre-stress" model of composite strengthening, could well account for the observed strength increase in the glass-ceramic samples, since any applied stress must overcome the compressive residual stress before fracture can commence.

Additional support for the pre-stress theory was provided by Tummala and Friedberg (16), who obtained strength increases for hot-pressed glass-stabilized zirconia composites only when  $\alpha_p > \alpha_m$ . For composites with  $\alpha_p < \alpha_m$  (so that the average matrix stress state would be tensile), only strength values below that of the base glass were obtained. It should be noted that neither Erdogan's analysis on the importance of flaw size-to-particle size ratio nor the pre-stress theory are applicable to the strengthening observed in the relatively coarse composites investigated by both Binns, and Frey and Mackenzie, especially in instances where the inclusion was of lower thermal expansion coefficient than the matrix. For these materials, strengthening must occur by some other mechanisms such as non-planar crack propagation (observed by Swearingen et al. (17) for similar composites) or, as Borom (18) has proposed, a mechanical reinforcement process associated with the higher elastic modulus of the dispersions. Both of these effects will be discussed shortly.

Although many of the investigations cited in this Section have been contradictory with respect to the effect that thermal expansion mismatch will have on strength, there is complete agreement, however, that strength decreases will occur once microcracking is initiated by mismatch stresses. Binns (12), Frey and Mackenzie (13), and Davidge and Green (19) all observed strength losses in glass-crystal composites only when microcracking was present.

Microcracking around inclusions in a brittle composite is influenced by two properties of the dispersed phase: thermal expansion coefficient relative to that of the matrix, and particle size. Binns (12) was the first to observe that the sign of the thermal expansion mismatch between matrix and inclusions determined the nature of any resulting microcracking. In composites with  $\alpha_p > \alpha_m$ , the tensile nature of the radial internal stress component (see Table I) in the near-matrix region around the particles causes circumferential cracking to occur around each inclusion. For  $\alpha_p < \alpha_m$ , radial cracks, driven by the tensile character of the tangential component of residual stress, form at the particle-matrix interface and extend outward into the matrix.

Binns also noted a particle size dependency for microcracking in that, at a given value of thermal expansion mismatch, microcracks would be more likely to form around coarse, rather than fine, particles. In the case of circumferential microcracking ( $\alpha_p > \alpha_m$ ), Davidge and Green (19) employed a Griffith-type energy balance approach to show that a critical size of inclusion radius existed below which no

microcracking will occur at a given value of thermal expansion mismatch. This critical radius,  $R_c$ , is given by:

$$R_c \geq 8\gamma_{\text{eff}} [(\alpha_p - \alpha_m)\Delta T]^2 \left\{ \frac{(1+\nu_m)}{2E_m} + \frac{(1-2\nu_p)}{2E_p} \right\}^{-1} \quad (\text{I-11})$$

where  $\gamma_{\text{eff}}$  is the fracture energy of the matrix, with the other terms defined in the same manner as was done for Eq. I-10.

Davidge and Green concluded that in brittle composites with  $\alpha_p > \alpha_m$ , the presence of particles larger than the critical size will result in the initiation of circumferential cracks about the inclusions with a flaw size equal to that of the particle diameter. Replacing the flaw size,  $c$ , in the Griffith formula (Eq. I-2) with the particle diameter,  $d$ , and replacing  $\gamma_s$  by  $\gamma_{\text{eff}}$ , gives the following expression for fracture strength:

$$\sigma_f = \left[ \frac{2E\gamma_{\text{eff}}}{(1-\nu^2)\pi d} \right]^{1/2} \quad (\text{I-12})$$

All of Davidge and Green's samples for which microcracking was predicted by Eq. I-12 had strength values below that of the base glass. For these composites, a plot of  $\sigma_f$  as a function of  $d^{-1/2}$  showed excellent agreement between observed strength values and the theoretical curve constructed from Eq. I-12. Composites for which no microcracking was predicted all had strength values above the theoretical curve. A strength dependency on  $d^{-1/2}$  predicted by Eq. I-12 has also been reported for several glass-ceramic systems (20-22).

Stress concentrations around an included particle in a composite may also arise during mechanical loading as a result of differences

in elastic modulus between the dispersion and the surrounding matrix. Goodier (23) has shown that the magnitude of these local stresses is proportional to the difference in shear modulus between the matrix and inclusion. These so-called micromechanical stress concentrations are extremely limited in range and achieve a maximum value at the particle-matrix interface. Regardless of the sign of the elastic modulus mismatch between matrix and inclusion, some component of matrix stress at the interface will always exceed the applied stress level. Hasselman and Fulrath (24) found ratios of local stress-to-applied stress of approximately 1.4 around alumina particles contained within a glass matrix, with the result that composite strength values were appreciably lower than that obtained on the matrix glass by itself. As noted in the discussion on internal stresses arising from thermal expansion mismatch, Khaund et al. (11) have shown that the presence of stress concentrations act to lower the effective fracture toughness of a material. As a result, the level of applied stress needed to cause catastrophic failure may be reduced.

Despite the higher stresses present at the particle-matrix interface from elastic mismatch, strength increases have been observed for brittle composites where differences occurred in elastic modulus between the various phases. This may reflect, as noted by Swearingen and Eagan (25) in the case of several zinc silicate glass-ceramics, an increased fracture toughness (as seen in Eq. I-6) for materials where the elastic modulus is raised by the addition of the dispersed phase. Borom (18) has used the term "mechanical reinforcement" to explain the strength increases reported by Binns (12) and Frey and

Mackenzie (13) for various glass-crystal composites in which elastic moduli mismatch occurred. In this model, strengthening occurs through a load-sharing process in which the external load is apportioned between the matrix and the dispersed phase on the basis of the individual elastic modulus. For the case of an inclusion with a higher elastic modulus than the matrix, the stress acting on the matrix is decreased, and the strength of the composite is increased, both in proportion to the composite modulus.

#### D. Crack-Crystallite Interactions; Effects Which Interfere With Crack Propagation

In brittle materials, the major strain energy-absorbing process, as seen from Eq. I-3, is the generation of surface energy through the formation of fracture surface. Increases in total fracture surface would be expected to result in higher values of both fracture energy and fracture toughness. In completely uniform materials such as homogeneous glasses, no microstructural features are present to increase relative toughness either by impeding crack propagation or by increasing the relative amount of fracture surface formed during such propagation. In glass-ceramics and other composites, the presence of a dispersed phase may act as a toughening mechanism, both by serving as an obstacle to crack propagation, as in crack bowing, or by increasing relative fracture surface area through mixed-mode propagation such as crack deflection around inclusions.

Bowing of cracks between second phase particles in a brittle composite has been proposed as a toughening mechanism by both Lange (26) and Evans (27). In this model, the dispersions are presumed to act as impenetrable barriers to any approaching crack front. As a result, a crack front encountering these obstacles becomes temporarily pinned until the stress acting to drive the crack front reaches a value sufficiently high to finally cause break-away of the crack front. During pinning, the crack front, assumed initially to be linear, bows out between adjacent particles in a manner analogous to dislocations pinned by precipitate particles in a dispersion-strengthened metal. Lange (26) attributed any rise in toughness to the higher levels of fracture energy,  $\gamma$ , needed for continued crack propagation as a result of the increased length of crack front:

$$\gamma = \gamma_0 + T/\lambda \quad (\text{I-13})$$

where  $\gamma_0$  is the fracture energy of the matrix,  $T$  is the line tension of the crack front, and  $\lambda$  is the interparticle separation distance (or mean free path) of the dispersions. Lange (28) subsequently modified his original model to reflect the greater pinning capacity of larger particles by including a particle size dependence for  $T$ . Green et al. (29) have extended this model to account for crack bowing observed with weaker, less impenetrable inclusions.

The crack bowing models proposed by Lange and Evans do not consider the influence of a dispersed particle's stress field on an approaching crack front. Khaund et al. (11) have shown that localized

stress non-homogeneities in a brittle composite caused by thermal or elastic mismatch will force a crack front to undergo a directional change as it approaches a second phase inclusion. Because of the distribution of tensile stress from the local stress fields present in mismatch situations, cracks will tend to propagate towards inclusions having a lower value of either thermal expansion coefficient (17) or elastic modulus (30) than the surrounding matrix, and to deviate away from particles where the nature of this mismatch is reversed. The crack propagation path will also be affected by differences in fracture energy between matrix and inclusion (31). The out-of-plane crack propagation resulting from these interactions is capable of producing appreciable increases in fracture toughness (32).

The manner in which the crack front is deflected by the inclusions (i.e., towards or away from the particles) will play a large role in determining the extent of the toughness increase produced by the change in crack propagation path. Nadeau and co-workers (33,34) were able to obtain significant toughening in a model glass-glass composite only when the expansion mismatch was such ( $\alpha_p < \alpha_m$ ) that crack deflection occurred towards the dispersed phase. No significant toughening was observed in mismatch situations where the crack propagation path deviated away from the particles. This conclusion is consistent with an observation by Green and Nicholson (35), that, in addition to the toughening increase from the surface roughness effect possible with crack deflection towards inclusions, additional

toughening interactions are likely such as crack bowing or direct intersection with the particle (which would utilize any intrinsically greater fracture toughness possessed by the inclusions relative to the matrix). Changes in crack path away from the particle offer only the possibility of toughening from increased surface roughness, an effect which is not likely to be substantial given the low fracture energies of typical matrix phases in brittle composites. Implicit in this discussion of crack propagation interactions is the assumption of a well-bonded interface, since as shown by Stett and Fulrath (36), weak bonding between matrix and inclusions will affect any potential toughening interactions.

Most of the studies cited in this Section have involved hot-pressed glass-crystal composites; however, crack deflection behavior has also been observed in several glass-ceramic materials where the scale of microstructure was considerably finer than the relatively-coarse textures of the hot-pressed composites. Deviation of cracks around crystallites as small as one micron were noted in an electron microscope study of fracture surfaces in several glass-ceramic materials (20,37). Faber and Evans (38) correlated a nearly-three fold increase in fracture energy for a lithium alumino-silicate glass after crystallization with crack deflection effects.

The discussion in this Section of crack-particle interactions occurring during crack propagation is pertinent not only for catastrophic failure conditions ( $K_I = K_{Ic}$ ), but also has relevance to instances of slow crack growth where propagation occurs at stress levels below

those associated with failure. Slow crack growth in brittle materials may occur through a moisture-dependent, stress-enhanced corrosion process (39) that can be detrimental from a mechanical standpoint in that several-fold increases in crack length are possible. Palmer et al. (40) have reported that crystallization of a  $\text{Li}_2\text{O-SiO}_2$  glass to form a glass-ceramic results in a decidedly-lowered susceptibility to slow crack growth effects. It appears reasonable, then, to speculate that the presence of a dispersed phase can restrict slow crack growth, both by the mechanisms discussed in this Section, as well as by a flaw limitation model which will be considered in the following Section.

#### E. Crack-Crystallite Interactions: The Flaw Introduction Process

As discussed previously, the strength of brittle materials is controlled to a large extent by flaws introduced from surface contact. Surface damage in brittle materials may be initiated during contact loading events associated, for example, with particle impact, shaping processes involving material removal, or accidental contact with other hard materials. The system of flaws introduced during surface contact plays a fundamental role in a host of mechanically-related phenomena such as strength degradation (41,42), erosion and wear of surfaces (43,44), and a variety of ceramic finishing operations (45,46) including cutting, grinding, and polishing.

The manner in which the dispersed phase will affect the size of failure-initiating flaws in brittle matrix composites is probably the

least understood topic associated with the mechanical behavior of these materials. Accordingly, this subject has received special emphasis in the research program carried out for this Dissertation.

The principal model for the role of the dispersed phase in a brittle composite undergoing surface damage is the flaw-limitation theory proposed by Hasselman and Fulrath (47). This hypothesis, which asserts that inclusions will act to limit the maximum size of extrinsic flaws, was proposed to explain the superior strength properties of hot-pressed glass-alumina composites compared to values obtained on the matrix glass alone (47). In this model, the fracture toughness of the dispersions is presumed to be sufficiently high so that the particles constitute impenetrable barriers to flaws. As a result, any flaws introduced in the composite will be limited by the included particles to the matrix phase on geometric grounds alone. Denoting  $\lambda$  as the mean free path\* between particles, and  $c_0$  as the flaw size which would be present in the matrix in the absence of dispersions, two specific regimes of strength behavior may be distinguished:

Region I ( $c_0 < \lambda$ )

---

\*The mean free path,  $\lambda$ , has been shown by Fullman (48) to be given by:

$$\lambda = \frac{\bar{L}(1-V_f)}{V_f} \quad (\text{I-14})$$

where  $\bar{L}$  and  $V_f$  are, respectively, the average linear intercept length and the volume fraction of the dispersed phase.

In this regime, the particles are sufficiently far apart so that flaw size will not be restricted by the inclusions, and as a consequence, strength will be independent of mean free path. Since the flaw size for the composite will equal  $c_0$ , measured composite strength values will not be different from that of the pure matrix itself.

Region II ( $c_0 > \lambda$ )

In this regime, the flaw size in the composite will be limited by the impenetrability of the inclusions from exceeding the mean free path distance. Since the composite's flaw size will be reduced below  $c_0$  by the mean free path restriction, strength will increase as  $\lambda$  becomes progressively smaller. Because flaw size equals mean free path in this regime, Eq. I-2 becomes:

$$\sigma_f = \left[ \frac{2E\gamma_{\text{eff}}}{(1-\nu^2)\pi\lambda} \right]^{1/2} \quad (\text{I-15})$$

where, since the flaws are assumed to propagate entirely within the matrix,  $E$  and  $\gamma_{\text{eff}}$  are, respectively, the Young's modulus and fracture energy of the matrix. Because strength values above that of the base matrix can be realized from the flaw-limitation role of the inclusions, the Hasselman-Fulrath hypothesis is frequently referred to as a "dispersion-strengthening" model.

The validity of the Hasselman-Fulrath approach rests in large part on the authors' assumption that it is the matrix phase alone, rather than the composite, which determines the basic aspects of the flaw introduction process. Justification for this view is provided by studies aimed at simulating extrinsic flaw introduction in homogeneous

materials. Analysis of solid particle impact events by Evans (43) and of quasi-static surface contact by Lawn and Marshall (49) indicate that both the size of flaws introduced as well as the level of surface contact needed to initiate flaws are inversely dependent on fracture toughness. Extending these findings to materials such as glass-crystal composites, the low fracture toughness of the glass matrix phase relative to any inclusions would appear to insure that the basic assumptions of the dispersion-strengthening model would be upheld. A qualifying statement should be made, however, that the flaw size-limiting role of inclusions in Region II would not be expected in situations where the flaw size-to-particle size ratio is large enough that the composite acts as a continuum for crack propagation. Instances such as this would occur when the level of surface contact is so severe that the stress intensity factor exceeds the fracture toughness of the inclusions or when the dispersions are extremely small ( $\ll 1 \mu\text{m}$ ) compared to the typical flaw sizes of 10-50  $\mu\text{m}$  commonly found in glasses and other low toughness materials.

Despite the almost intuitively reasonable nature of the model, the Hasselman-Fulrath hypothesis has not been universally received or widely corroborated. Both Lange (28) and Borom (18) have interpreted Hasselman and Fulrath's data on the basis of other models (crack bowing and mechanical reinforcement, respectively), although it is difficult to see how these alternative approaches predict the mean free path-independent strength behavior of Region I. Wahi and Ilschner (50) reported a flaw size that decreased with decreasing TiC mean free path in  $\text{Al}_2\text{O}_3$ -TiC composites, although the calculated

flaw sizes were some 20-30 times the measured mean free path values. Strength values inversely related to the square root of mean free path were obtained on a  $\text{Li}_2\text{O-SiO}_2$  glass-ceramic by both Freiman and Hench (51) and Atkinson and McMillan (52). However, the  $\sigma_f \propto \lambda^{-1/2}$  relationship predicted for Region II of Hasselman and Fulrath's model may also be derived from the crack bowing hypothesis by substituting Lange's expression for fracture energy (Eq. I-13) into the Griffith equation (Eq. I-2). A more extensive examination by Hing and McMillan (53) of essentially the same glass-ceramic composition investigated by Freiman and Hench, and Atkinson and McMillan, provided the most unambiguous confirmation to date of the Hasselman-Fulrath model. Both Region I and Region II behavior were demonstrated. Furthermore, excellent agreement was obtained between the calculated flaw size and the measured mean free path distance in the composite. Miyata and Jinno (54) have extended the Hasselman-Fulrath model to systems where substantial microcracking takes place. With increasing volume fraction of dispersion, strength decreases may well occur for microcracked composites at low volume fractions of dispersed phase until the mean free path distance becomes sufficiently small to limit both intrinsic and extrinsic flaws.

#### F. Indentation Fracture in Brittle Materials

Recently, indentation techniques employing standard microhardness equipment have been developed into a powerful tool to simulate and characterize surface damage. The initial work in this area goes back

to Hertz (55) and his analysis of spherical ("blunt") indenters in contact with planar surfaces. Much of today's effort utilizes so-called sharp indenters (such as cones and pyramids), since their constant contact angle with the indented surface produces an indent shape that is not dependent on penetration depth. This assures that an invariant contact pressure is maintained throughout the entire indentation sequence (56). Additionally, sharp indenters cause cracks to be initiated at much lower loads than blunt indenters and are thus more suitable from a conservative design standpoint. Much of the discussion that follows will involve the Vicker's indenter, a four-sided regular diamond pyramid that gives an impression having a square cross-section when viewed in projection from above.

The indentation stress field associated with sharp indenters is extremely complex (57,58), and is dominated by components of shear and hydrostatic compression which permit irreversible deformation modes such as plastic flow and densification to be realized in brittle materials. It is this irreversible deformation which results in the permanent impression left in the indented material once the indenter is removed. The ability of a material to resist this permanent deformation during indentation is termed the hardness and is defined as the ratio of load on the indenter to true surface area of the resulting impression. For a Vicker's indentation, the hardness,  $H$ , is given by:

$$H = (P/2a^2)\sin \theta/2 \quad (I-16)$$

where  $P$  is the load on the indenter,  $a$  is the half-diagonal of the projected square impression, and  $\theta$  is the interior angle of the indenter ( $136^\circ$ ).

Indentation fracture mechanics have generally been analyzed using an elastic-plastic model (57,59) to define the spatial extent of the tensile stresses developed during indentation. The tensile stresses, although small in comparison to the shear and hydrostatic compression components, are present nevertheless at a level generally sufficient to cause crack systems to develop around the indent. The typical physical model, shown in Figure 1, assumes a spherical symmetry to the deformation field. Surrounding the point of contact is a plastic region where flow has occurred once some characteristic yield stress has been attained. Material outside the plastic zone has not been stressed to the yield value and represents a region of elastic deformation. During indentation, tensile stresses, as seen from Figure 2, are most intense in a near-surface region and also directly below the indenter at the elastic-plastic interface.

The volume of material displaced by the indenter is accommodated during indentation by strains in the elastic region. Since a permanent impression remains after removal of the indenter, these strains are present both during and following unloading where they define a residual stress field. This residual stress field serves to initiate a series of cracks to form during the unloading cycle which are called lateral cracks (see Figure 3). These saucer-shaped cracks form at the elastic-plastic interface, propagate initially on planes roughly

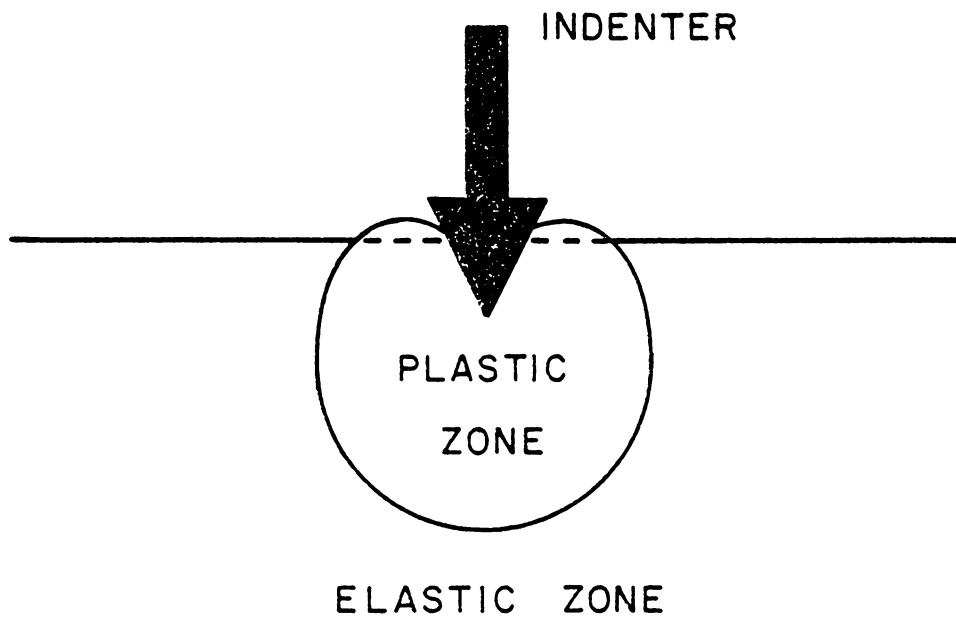


Fig. 1. Schematic illustration of deformation fields during indenter contact in elastic-plastic indentation model (adapted from ref. 57).

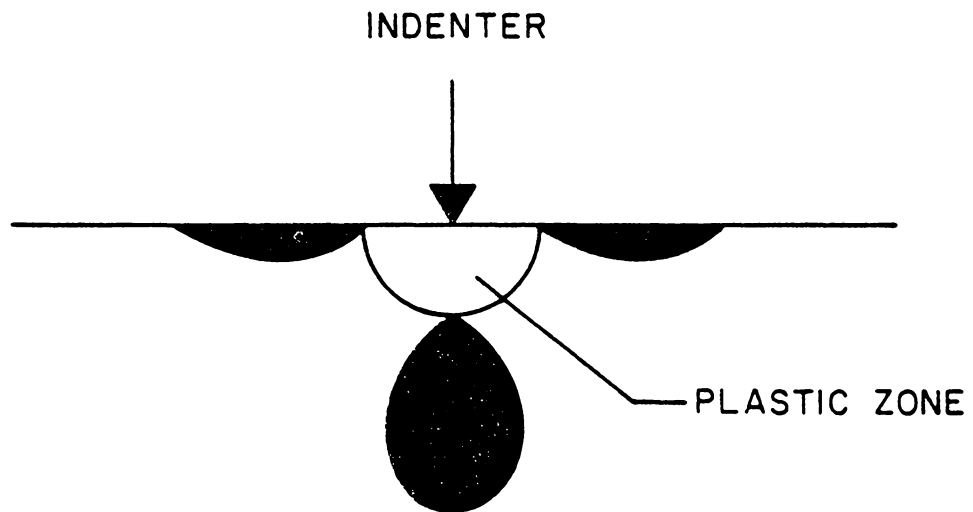


Fig. 2. Location of tensile fields (darkened regions) during indentation loading cycle (adapted from ref. 49).

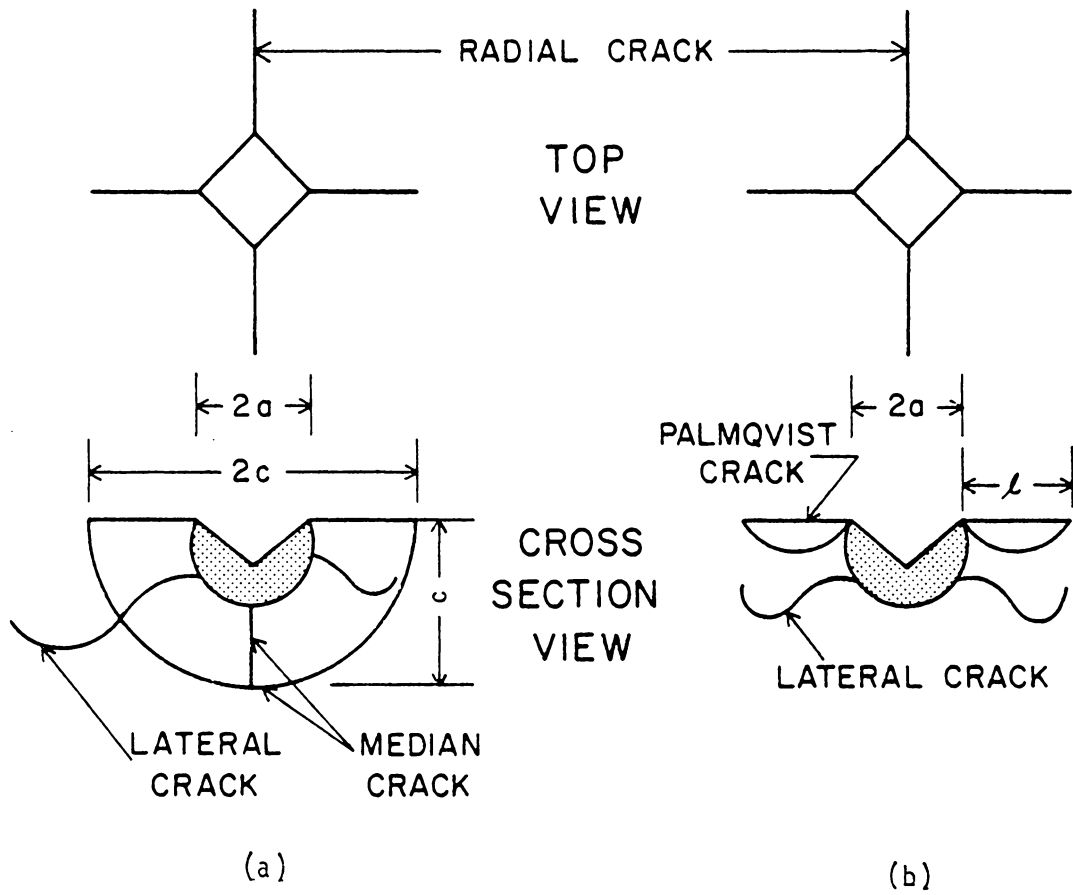


Fig. 3. Top and cross-sectional views around Vicker's indent assuming: a, median cracks; and b, Palmqvist cracks. The plastic zone appears as the stippled region.

parallel to the surface, and then curve upwards towards the surface. These cracks play a major role in wear processes such as abrasion and erosion where linkup of adjacent lateral cracks constitutes a primary mechanism of material removal.

The crack system which is of major interest from a flaw introduction standpoint is, in the case of a Vicker's indent, a series of individual cracks which appear to emanate from each indent corner as seen in Figure 3. These cracks, which are far less blunt and have the potential for extending much deeper into the material than lateral cracks, play a major role in the strength behavior of brittle materials following surface contact. Lawn and co-workers (60,61) have proposed that these cracks, which are termed median cracks, form initially as full-penny or circular cracks at the sub-surface tensile zone on orthogonal planes that are normal to the surface and contain the indenter axis and one of the indent diagonals. As the load on the indenter is increased, the median cracks grow in size until they intersect the surface, at which point they assume a half-penny geometry, (as shown in Figure 3a) with characteristic surface traces called radial cracks. Because of the semi-circular configuration, the depth,  $c$ , of these half-penny cracks may be determined by measuring the length of the associated radial crack along the surface from the center of the indent to the crack tip. For well-developed median cracks (i.e.,  $c \gg a$ ), Lawn and Swain (60) have shown that the following relationship exists between crack length and indenter load:

$$K_{Ic} = \chi_r P_c^{-3/2} \quad (I-17)$$

where  $\chi_r$  is a dimensionless constant related to the residual stress field about the indentation. Solving for crack length and substituting in the general form of the Griffith-Irwin expression (Eq. I-7) gives the following relationship for strength loss accompanying quasi-static indenter contact:

$$\sigma_f = [(\chi_r K_{Ic})^4 Y^{-1/2}] P^{-1/3} \quad (I-18)$$

where  $Y$  is a crack-geometry constant. The  $\sigma_f \propto P^{-1/3}$  relationship predicted by this expression only applies when the contact-induced flaws are dominant (i.e., strength-controlling). For instances where the pre-existing flaws are large enough to control strength behavior, fracture strength will be independent of contact load until a level of indenter load is reached at which the indentation flaws are large enough to control strength.

Although the median crack model is widely-accepted as accurately describing fracture behavior in the high load or far-field indentation regime ( $c \gg a$ ), disagreement exists as to its applicability at lower indenter loads and smaller  $c/a$  ratios. Perrott (57) has maintained that at low loads, it is the near-surface, rather than the sub-surface, tensile region which dominates fracture behavior. Palmqvist (62) observed a radial crack system (Fig. 3b) which does not represent traces of half-penny cracks, but rather is associated with shallow, semi-elliptical cracks which originate at each indent corner. The characteristic surface dimension of these Palmqvist cracks is  $\ell$ , the distance along the surface from the corner of the indent to the crack tip. Comparison of Figs. 3a and 3b indicate that:

$$l = c - a = \frac{c}{a} - 1 \quad (\text{I-19})$$

In contrast to the crack size-load relationship of  $c \propto P^{2/3}$  predicted for median cracks from Eq. I-17, Palmqvist, and Dawihl and Altmeyer (63) observed a linear load dependence for Palmqvist crack size,  $l \propto P$ . The presence of Palmqvist, rather than median, cracks at low loads has been confirmed by Lankford and Davidson (64) for a variety of brittle materials such as silicon carbide and aluminum oxide. Sectioning work by Hagan and co-workers (65-67) in a variety of silicate glasses indicate that radial cracks will form at low loads in the absence of any observed median cracking. Direct optical examination by Evans and Wilshaw (68) in silicon nitride and other brittle materials again confirms that only Palmqvist cracks are present at low  $c/a$  ratios. In this Dissertation, where the indentation technique will be used to introduce flaws on the order of the mean free path dimension in a glass-ceramic, the fine texture of this material will require that indentations be made at low loads ( $c/a < 2.0$ ). Thus, Palmqvist cracks will be the likely source of any observed radial cracking.

Indentation studies of the fracture behavior of brittle materials indicate the existence of a "universal" curve relating hardness, fracture toughness, and the measured indentation parameters of crack size and indent size. Evans and Charles (69) concluded, using a dimensional and fracture mechanics analysis of indentation data from a variety of brittle materials, that a plot of  $(K_{Ic} \phi H a^{1/2}) (H/E\phi)^{2/5}$  as

a function of  $c/a$  ratio defined a curve which described the fracture and deformation behavior of these materials.

In this relation,  $\phi$  is a constraint factor equal to approximately 3. Blendell (70) has used curve-fitting procedures to obtain the following expression for the Evans-Charles curve:

$$(K_{Ic} \phi / H a^{1/2}) (H/E\phi)^{2/5} = 0.055 \log 8.4 (a/c) \quad (I-20)$$

Niihara et al. (71,72) found, however, that indentation fracture data obtained at low  $c/a$  ratios for soda-lime-silica glass and silicon nitride, as well as reported low load data (63) on WC-Co alloys, deviated from the universal curve of Evans and Charles and accordingly were not satisfactorily described by Eq. I-20. Niihara et al. attributed these deviations from the Evans-Charles model to the occurrence of Palmqvist, rather than median, cracks at low loads, and proposed the following modification to the basic Evans-Charles relation:

$$\frac{\text{for } c/a \geq 2.5 \text{ (median crack regime)}}{(K_{Ic} \phi / H a^{1/2}) (H/E\phi)^{2/5} = 0.129 (c/a)^{-3/2}} \quad (I-21a)$$

$$\frac{\text{for } \ell/a \leq 2.5 \text{ (Palmqvist crack regime)}}{(K_{Ic} \phi / H a^{1/2}) (H/E\phi)^{2/5} = 0.035 (\ell/a)^{-1/2}} \quad (I-21b)$$

Note that there is a region of overlap defined by  $1.5 < \ell/a < 2.5$  (or  $2.5 < c/a < 3.5$ ) where either expression is suitable to describe deformation/fracture behavior. In principle, then, fracture toughness may be obtained from an indentation procedure by measuring  $\ell$

(or  $c$ , depending on the relative load) and  $a$ , and by determining  $E$  through a separate measurement.

The key material parameters which emerge from Eqs. I-21,  $a$  and  $b$ , for characterizing the elastic-plastic response of brittle materials during sharp indenter contact, are seen to be the hardness and fracture toughness. The importance of these parameters in modelling other surface contact events may be seen in work by Lawn and Evans (73) concerning the level of critical or threshold load needed to initiate radial cracking from a sharp indenter. This threshold load,  $P_c$ , and the crack size,  $c^*$ , formed at the critical load were all determined to be functions of hardness and fracture toughness:

$$P_c \propto (K_{Ic}/H)^3 K_{Ic} \quad (I-22)$$

$$c^* \propto (K_{Ic}/H)^2 \quad (I-23)$$

Although these relationships were derived on the basis of median crack geometry, Lankford and Davidson (64) have found that they are also valid for Palmqvist cracks, at least from a relative standpoint, to rank materials on the basis of their resistance to surface damage. The importance that  $K_{Ic}$  and  $H$  play in the indentation process is also found in other surface contact phenomena, and serves to illustrate at least indirectly, the high degree to which the indentation method successfully simulates actual surface damage events. Both the volume of material removed by erosive wear during solid particle impact (52), and the relative ease with which brittle materials may be finished in abrasive machining operations (74) are all dependent on some combined

hardness/toughness function. Indentation techniques, then, constitute a powerful method for modelling real contact situations and for characterizing the resulting flaw introduction process.

#### G. The Glass-Ceramic Process

Since a glass-ceramic will constitute the model composite used to study the effect that the dispersed phase in brittle materials has on mechanical performance, a brief description of glass-ceramic technology, insofar as it affects possible strength or toughness-controlling microstructural variables will be presented here. Emphasis will be placed on how process variables control the more important microstructural features, such as particle size and dispersed phase volume fraction.

Controlled crystallization of a glass to produce a glass-ceramic results in a glass-crystal composite where, by close control over the heat-treatment operation, both the desired phase assemblage as well as the optimal combination of microstructural parameters (such as size, shape, and volume fraction of dispersed phase) may be achieved. Generally, only a negligible quantity of pore phase is created during this process, so that the complicating effect of porosity may be avoided in any subsequent analysis of microstructure-property relationships.

Crystallization from a glass is neither a new nor unique phenomenon - witness the appropriately-named compound devitrite ( $\text{Na}_2\text{O} \cdot 3\text{CaO} \cdot 6\text{SiO}_2$ ) which was such a curse to early manufacturers of soda-lime-silica glass (75). However, what distinguishes the glass-ceramic

process from other devitrification phenomena is the control over the crystallization process permitted by glass-ceramic technology. Uncontrolled devitrification is frequently only a surface event characterized by large crystallites growing radially inward into the bulk of the glass article from the surface with most of the interior of the sample remaining unaltered and totally glassy. The coarse surface texture combined with the oriented nature of the crystal growth and the unfavorable stresses introduced by thermal expansion and density gradients between exterior and interior of the sample leads to a very weak and readily-degraded structure. In glass-ceramics, however, these problems can be avoided by careful time-temperature control of a two-step process involving separate nucleation and growth stages for the crystallite phase. The end product is characterized by a dispersion of fine crystallites distributed uniformly throughout the entire sample.

The nucleation step can probably be singled out as the most critical operation in the glass-ceramic process for it determines whether a uniform crystalline dispersion is achieved. Despite the fact that at temperatures below the liquidus, the crystallite phase will have a lower volume free energy than either the liquid or the glass, substantial thermodynamic and kinetic barriers work against spontaneous, large-scale crystallization. For this reason, crystallization is first initiated at discrete centers or nuclei, with subsequent outward growth from these sites proceeding by successive deposition of atoms onto the interface separating the crystallized

and non-crystallized regions. The nucleation process may be classified as either homogeneous or heterogeneous depending on whether, as in the case of homogeneous nucleation, the nuclei have the same composition as the parent glass and do not form on pre-existing boundaries such as free surfaces. Nucleation in glasses is almost always accomplished via a heterogeneous process since either the nuclei will differ in composition from the glass or else they will form preferentially around gas bubbles, undissolved batch constituents, or at the surface.

Models dealing with homogeneous nucleation are simplest to derive. For the homogeneous nucleation of a spherical crystallite at a temperature below the liquidus, the free energy change upon nucleation  $\Delta G_r$ , is given by:

$$\Delta G_r = 4\pi r^2 \gamma + \frac{4}{3} \pi r^3 \Delta G_v \quad (\text{I-24})$$

where  $r$  is the particle radius,  $\gamma$  is the interface energy, and  $\Delta G_v$  is the volume free energy change accompanying the nucleus formation with  $\Delta G_v = G_{\text{crystal}} - G_{\text{glass}}$ . Since for temperatures  $<$  the liquidus,  $G_{\text{crystal}} < G_{\text{glass}}$ , the contribution from  $\Delta G_v$  provides the driving force for nucleation. However, at small values of  $r$ , the surface energy term is dominant in Eq. I-24. As a result, initial increases in nucleus size will cause an overall energy increase to occur in the system. Growth of the nucleus will still be possible to some extent because of energy variations caused by localized fluctuations in temperature and composition.

Only when some critical value of radius,  $r^*$ , is attained will the volume free energy term in Eq. I-24 become sufficiently large that incremental nucleus growth beyond  $r^*$  results in a net free energy decrease. For this reason, only nuclei with  $r > r^*$  will be stable. This critical value of radius is obtained by setting  $\partial\Delta G_r/\partial r = 0$ , with the result

$$r^* = -2\gamma/\Delta G_v \qquad \Delta G^* = \frac{16\pi\gamma^3}{3(\Delta G_v)^2} \qquad (\text{I-25,a,b})$$

where  $\Delta G^*$ , the free energy change accompanying the formation of the nucleus of critical size, represents the maximum free energy barrier for nucleation. In the case of heterogeneous nucleation,  $\Delta G^*$  is replaced by  $\Delta G^* f(\theta)$ , where  $\theta$  is the contact angle between the nucleus and the foreign surface. Generally (76),  $0 \leq f(\theta) \leq 1$ , so that heterogeneous nucleation offers the likelihood of a substantial decrease occurring in the height of the free energy barrier to nucleation.

In addition to the thermodynamic barrier to nucleation represented by  $\Delta G^*$ , an additional obstacle exists from kinetic or mass transport considerations. Nucleus growth is limited by the rate at which atoms or molecules arrive at the interface for incorporation into the nucleus. Becker (77) has derived a general expression for the rate of nucleation,  $I$ , in condensed systems that incorporates both the thermodynamic and the kinetic restriction:

$$I = A \exp \left[ \frac{-(\Delta G^* + Q)}{kT} \right] \qquad (\text{I-26})$$

where A is a pre-exponential term that is dependent, in part, on (viscosity)<sup>-1</sup>, Q is the activation energy for diffusion of atoms across the phase boundary, k is Boltzman's constant, and T is the absolute temperature. A low value of nucleation rate is predicted by Eq. I-26, both near the liquidus as well as at much lower temperature because of, respectively, high values of  $\Delta G^*$  or Q. Only at some intermediate temperature range where the volume free energy driving force is high and transport processes occur relatively rapid will the nucleation rate be substantial.

Once nuclei have attained the critical size needed for stability, growth considerations will then be the controlling process involved with crystallization. As was the case for nucleation rate, both thermodynamic and kinetic factors determine the growth rate. Atoms must first be transported to the crystal-glass interface and then must obtain sufficient energy to overcome any energy barrier associated with adopting the atomic configuration of the crystalline structure. A simplified expression obtained from empirical considerations has been found by Swift (78) to describe the growth rate, U, for several alkali silicate phases from silicate glasses:

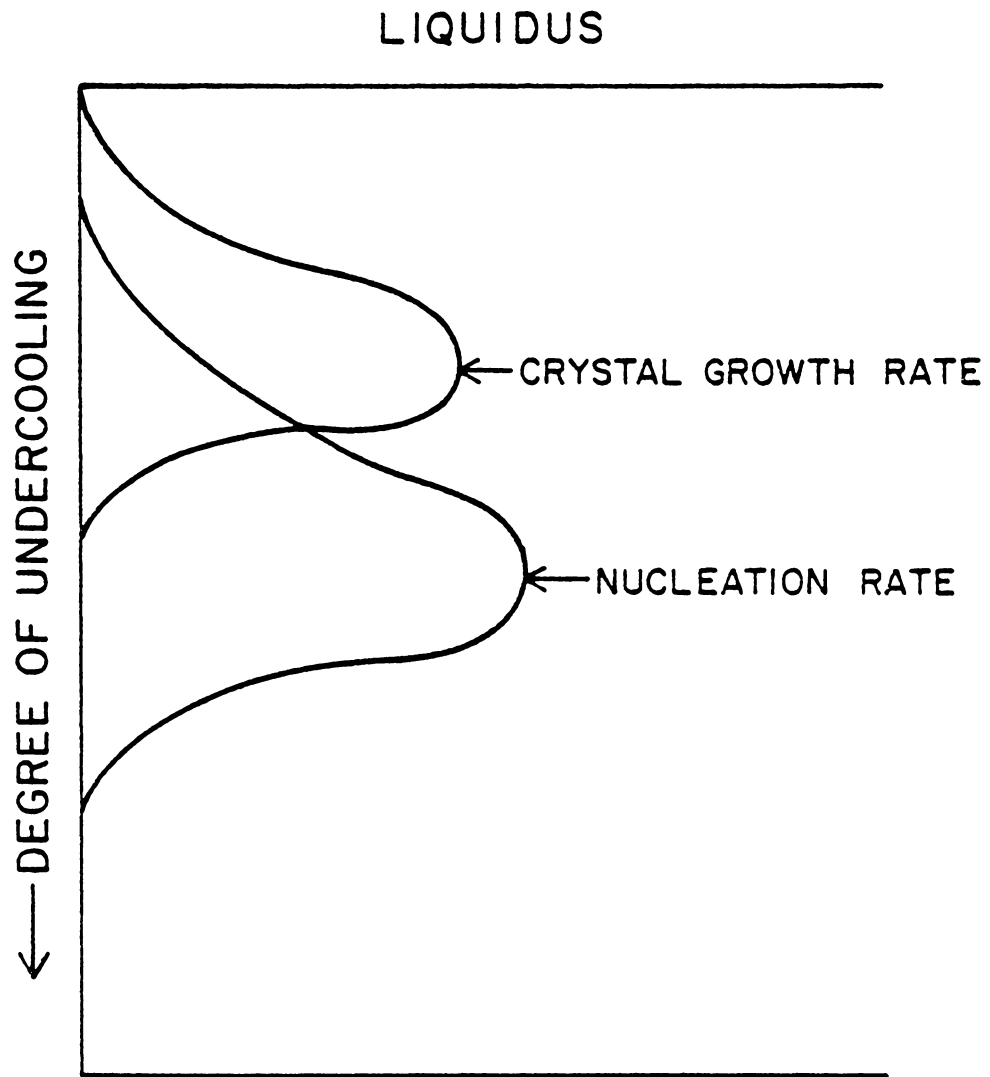
$$U = \frac{K}{\eta} (T_{liq} - T) \quad (I-27)$$

where K is a constant,  $T_{liq}$  is the liquidus temperature, and T is the temperature of interest. Kinetic influences are represented by the inclusion of the viscosity,  $\eta$ , while the degree of undercooling,  $T_{liq} - T$ , is a reasonable approximation of thermodynamic effects.

Like the corresponding expression for nucleation rate, Eq. I-27 predicts a maximum in growth rate at some intermediate temperature range.

Nucleation and growth rate curves are shown as a function of temperature in Figure 4 for a hypothetical glass. Although there is no theoretical reason for these two rate curves not to overlap, it is essential from the standpoint of achieving a glass-ceramic with a dispersion of fine crystallites that any overlap be at a minimum. Should these two processes occur simultaneously, the end product will be a structure composed of a small number of coarse crystallites.

Given nucleation and growth curves with a reasonable degree of non-overlap such as depicted in Figure 4, glass-ceramic technology makes use of a two-stage heat-treatment process to obtain a uniform dispersion of fine-crystallites (79). The first stage of the heat-treatment accomplishes the nucleation process, while subsequent growth of the nuclei to attain the desired crystallite size and volume fraction is achieved by an additional heat-treatment at a suitable growth temperature. "Crystallization catalysts" are also used to assure that nucleation proceeds evenly throughout the entire sample and is not limited to just the surface. These crystallization catalysts are materials which in themselves are not the desired crystallization end product, but which accelerate the crystallization process by providing sites for nucleation of the desired crystal phase. Chief among these catalysts is titania, whose use was first reported by Stookey



### RATES OF NUCLEATION AND CRYSTALLIZATION

Fig. 4. Nucleation and crystallization rates for a glass-ceramic as functions of temperature.

in the original glass-ceramic patent (79). Other common nucleating agents include  $ZrO_2$  and  $P_2O_5$ .

Originally it was thought that these nucleation catalysts first crystallized from the glass through some homogeneous mechanism. This is not now believed to be the case. Considerable evidence (80,81) suggests that these nucleating agents instead promote the separation of the glass into two immiscible glassy phases which in turn act as sites for heterogeneous nucleation of the desired crystal compound. Because of the low interfacial energy existing between two liquids or glasses, thermodynamic barriers to phase separation are quite low. Separation, thus, can take place rather readily by homogeneous nucleation on a fine-scale basis throughout the glass, either during cooling of the glass following the forming process or else during the initial stages of the nucleation heat-treatment.

Essential, then, to the production of high quality glass-ceramics is the nucleation process. Nucleation must occur uniformly throughout the entire bulk of the glass and over a temperature region distinct from that where any appreciable crystal growth occurs. Control over the nucleation and growth processes permits, in turn, control over microstructural parameters, many of which may be important from a mechanical standpoint. Obviously, final crystal size is determined by the selection of the time-temperature combination of the growth heat-treatment. Other important variables such as volume fraction and interparticle separation distance may be altered by adjustments in either the nucleation or growth heat treatments (82). The coarseness and volume fraction of any precursor phase separation step will

also exercise a large measure of control over the end microstructure (83). Stewart (84) has shown that in several glass-ceramic systems the identity of the final crystal phase may even be altered by the choice of growth temperature or nucleating agent. The glass-ceramic process is ideal, then, for obtaining a wide variety of different microstructures to study dispersed phase-crack interactions in brittle composites.

#### H. Objectives of the Research Program

It has been shown in the preceding Sections that the strength of brittle composites is dependent upon a variety of flaw-dispersed phase interactions. The emphasis in this Dissertation will be placed on characterizing these interactions for a model brittle composite, a glass-ceramic. The micro-hardness indentation method will be used to simulate surface damage so that flaw-microstructure effects may be observed directly, by electron microscopy, rather than inferred as typically done in past studies.

The objectives of this Research are as follows:

(i) To determine the role played by the dispersed phase in a brittle composite during the flaw introduction process - more specifically, to investigate how inclusions affect both the size and the level of surface contact required to initiate flaws.

(ii) To determine the manner in which the dispersed phase affects flaw stability, i.e., crack propagation and strength behavior.

(iii) To characterize the various microstructural variables, such as particle size and volume fraction of inclusions, which are found to control the above two processes.

Information gained from this Research would be expected to prove valuable in the design of brittle composite materials having maximum resistance to both surface damage and associated strength loss and wear phenomena.

## II. EXPERIMENTAL PROCEDURE

### A. Sample Preparation and Preliminary Characterization

#### 1. Material

A glass-ceramic<sup>†</sup> having as its major phase the compound cordierite ( $2\text{MgO}\cdot 2\text{Al}_2\text{O}_3\cdot 5\text{SiO}_2$ ) was selected for this study. This particular glass-ceramic has been the subject of a number of investigations involved with the thermal and mechanical behavior of brittle materials (85-87).

The glass-ceramic which was used is derived from a  $\text{MgO-Al}_2\text{O}_3\text{-SiO}_2$  glass to which  $\text{TiO}_2$  has been added as a nucleating agent (79). The addition of titania serves to promote the separation of the glass into two immiscible glassy phases. As noted in the discussion of the glass-ceramic process in Chapter I, phase separation of the precursor glass is beneficial to achieving a high quality glass-ceramic since a multitude of pre-existing surfaces are created to assure that any subsequent crystallization will be accomplished on a very uniform and fine scale throughout the bulk of the glass. Phase separation in  $\text{TiO}_2$  nucleated  $\text{MgO-Al}_2\text{O}_3\text{-SiO}_2$  glasses has been observed during cooling of the glass following melting (88), as well as during subsequent heating of the glass to  $750^\circ\text{-}800^\circ\text{C}$  (89).

Since cordierite glass-ceramics are of commercial importance because of their low coefficient of thermal expansion, a number of detailed studies (90-92) have been reported describing their crystalliza-

---

<sup>†</sup>C-9606, Corning Glass Works, Corning, NY.

tion behavior. Heat-treatment of the glass results in the crystallization at 900<sup>o</sup>-950<sup>o</sup>C of a stuffed high quartz phase,  $MgO \cdot Al_2O_3 \cdot nSiO_2$  ( $2 \leq n \leq 5$ ), designated as  $\mu$ -cordierite (93). Almost complete transformation of the glass into a polycrystalline material is accomplished at this point, with only a negligible amount (2-5 vol.%) of residual glass remaining (86).

Heat-treatment of the stuffed quartz phase beyond 1000<sup>o</sup>C produces a complex series of solid state reactions. The stuffed quartz phase exsolves spinel ( $MgO \cdot Al_2O_3$ ) and, as a result, becomes silica-enriched. At about 1100<sup>o</sup>C, the stuffed quartz phase reacts with the spinel to form high, or  $\alpha$ , cordierite ( $2MgO \cdot 2Al_2O_3 \cdot 5SiO_2$ ). Any unreacted stuffed quartz (by then, appreciably enriched in silica) transforms into a silica polymorph, high-cristobalite. The presence of cristobalite is extremely undesirable in ceramic bodies from a commercial standpoint since the volume change associated with the cristobalite inversion at approximately 275<sup>o</sup>C is large enough to cause cracking when this phase is present in substantial quantity. The amount of cristobalite produced in the glass-ceramic may be minimized by close control over heating rates, since slow heating rates ( $\approx 5^{\circ}C \text{ min.}^{-1}$ ) have been found to favor the stuffed quartz-spinel reaction (92). Continued heat-treatment of the  $\alpha$ -cordierite phase results in the gradual growth of  $\alpha$ -cordierite crystals from a much finer-grained  $\alpha$ -cordierite/high cristobalite matrix (90). With very long heating times, such as several weeks duration (well beyond commercial glass-ceramic heat-treatment times),  $\alpha$ -cordierite will invert to low, or  $\beta$ , cordierite (90).

## 2. Sample geometry and heat-treatment

A single block (15-20 kg) of the glass-ceramic in the form of the original or unheat-treated glass was donated by the manufacturer. A few specimens used in this study were thin discs, approximately 0.2 cm. in thickness and 1.3 cm. in diameter, that had been drilled from this block, heat-treated, and used in a previous investigation (86) concerning the effect of crystallization of a glass-ceramic on thermal diffusivity. However, most samples, especially those for which both strength and indentation data were measured, were in the form of circular cross-section rods, approximately 2.0 cm. in length and 1.3 cm. in diameter, that had been core-drilled from the block of original glass.

All samples that were crystallized received a nucleation heat-treatment of 820°C for 2 hours, after which they were subjected to various time-temperature treatments to obtain a variety of microstructures covering a range in crystallite size and volume fraction of dispersed phase. These crystallization heat-treatments covered the temperature range from 905°C to 1260°C, and involved holding times at maximum temperature of up to 8 hours. The 1260°C heat-treatment represented an upper temperature limit for the crystallization treatment. Samples heated to slightly higher temperatures (1290°C) all showed considerable slumpage as a result of excessive liquid formation.

Heat-treatment for the core-drilled rods was carried out in a high-alumina tube furnace heated by external silicon carbide elements and controlled by a cam-monitored temperature controller.<sup>+</sup> Measurements on this furnace indicated that a zone of relatively constant temperature ( $\pm 10^{\circ}\text{C}$ ) occurred along a section of furnace tube approximately 9 cm. in length. This permitted 8 of the sample rods to be heat-treated simultaneously by arranging them in adjacent rows of 4 rods each. A heat-up rate of  $5^{\circ}\text{C min.}^{-1}$  was used for all heat treatments. In accordance with a suggestion (94) made by the manufacturer of the glass-ceramic, a cooling rate of  $2^{\circ}\text{C min.}^{-1}$  was maintained from the crystallization temperature to about  $500^{\circ}\text{C}$ . Below this temperature, the thermal mass of the furnace caused the actual cooling rate to lag behind that set on the cam. All physical property measurements, such as crack length and strength for a specific heat-treatment, were obtained from the same set of samples to avoid any minor differences in microstructure between samples from separate, but nominally-identical, heat-treatments.

### 3. Sample polishing

Following crystallization, slices were cut from the sample rods with a diamond cut-off saw. A thickness of 1 mm. was used for all strength samples, while a slightly larger thickness (typically 3-5 mm.) was used for samples on which only crack length measurements were obtained. These latter samples were subjected to a grinding and

---

<sup>+</sup>Trend-Trak Recorder, Speedomax Series, Leeds and Northrup, Philadelphia, PA.

polishing operation which consisted of the following sequence of steps: 400- and 600- grit silicon carbide paper, 9  $\mu\text{m}$  diamond impregnated bronze wheel, and 1  $\mu\text{m}$  and 0.3  $\mu\text{m}$  alpha-alumina polishing cloth. For strength specimens where a surface as nearly flaw-free as possible is desired, a final polishing operation of 0.25  $\mu\text{m}$  diamond polishing cloth was performed. After polishing, samples were annealed at 650°C for 3-4 hours to relieve any stresses introduced during sample preparation.

#### 4. Quantitative microscopy

Volume fraction and mean free path (i.e., mean distance between crystallites) parameters were determined for crystallized samples from photographs taken with a scanning electron microscope<sup>+</sup> (SEM). The polished samples were first etched 30 seconds in 5% HF to reveal the microstructure. Samples were then coated with 150-200Å of gold to prevent charge build-up during SEM observation.

SEM magnifications in the range 6,500-15,000X were used for the quantitative microscopy. These actual magnifications were obtained from the dial-setting magnifications on the SEM using a calibrated grid<sup>++</sup> especially designed for SEM use. Correction factors obtained in this manner agreed well with calibration values reported by Lytton (95) for the same instrument. The SEM correction factors were checked by comparing size data for the same features (a series of indents) measured by both scanning electron and optical microscopy. The

---

<sup>+</sup>JSM-2, Japan Electron Optics Laboratory Co., Ltd. Tokyo, Japan.

<sup>++</sup>Calibration Standard No. 1749, E.F. Fullam, Inc., Schenectady, NY.

calibration factors for the SEM were found to be correct. As a final precaution against any errors in magnification, a single working distance was employed for all SEM work to assure that measurements would be correct, at least on a relative basis, for all samples.

Volume fraction measurement were made using standard point count procedures (96). A square grid was randomly placed over a photomicrograph and the particular phase noted which fell under each grid intersection point. The magnification used in each photomicrograph was always selected to assure that the size of the microstructural features (i.e., the dispersed phase) was at least as large as the 7 mm. grid spacing employed. Approximately 725 grid counts were made for each sample from a total of 4 photomicrographs taken at random locations within the sample.

The mean free path distance for a dispersed phase contained within a matrix is calculated typically from the Fullman expression (Eq. I-14) using values of volume fraction and mean intercept length determined for the dispersions by, respectively, point count and linear intercept techniques. A series of parallel test lines is employed in this latter procedure, with the mean intercept length,  $\bar{L}$ , defined as the fractional length of test line subtended by the microstructural feature divided by half the total number of intercepts (per unit length of test line) that occur between the particular feature and

the test lines (97). Mean intercept length is a convenient and efficient means to characterize particle size, and for simple particle geometries such as a sphere or a plate,  $\bar{L}$  can be directly related to particle radius or thickness. However, the highly-irregular shape of the dispersed phase in the glass-ceramic caused the linear intercept technique to prove unreliable in obtaining meaningful crystallite size data since the same dispersed particle would frequently be intercepted more than twice by a given test line. As a result, both particle size and mean free path were found to be underestimated by the use of the linear intercept technique.

The difficulties in obtaining representative microstructural data were overcome using a procedure which involved direct measurement of mean free path as depicted in Figure 5. This approach is based on the recognition that the mean free path distance represents the average of the length of all vectors which can be drawn outward from a point on the surface of a given particle to all neighboring particles. With the direct measurement procedure, a radial grid, with an angular spacing of  $10^\circ$ , was maneuvered in a random manner over a SEM micrograph until the origin of the grid fell on the surface of a particle. The free path distances were then measured and this process was repeated until data from a total of 8 random sites had been obtained from the photomicrograph. The mean free path value for each photomicrograph was determined by averaging these free path measurements and correcting for magnification. Since the free path measurements for a given heat-treatment were taken from the same series of 4

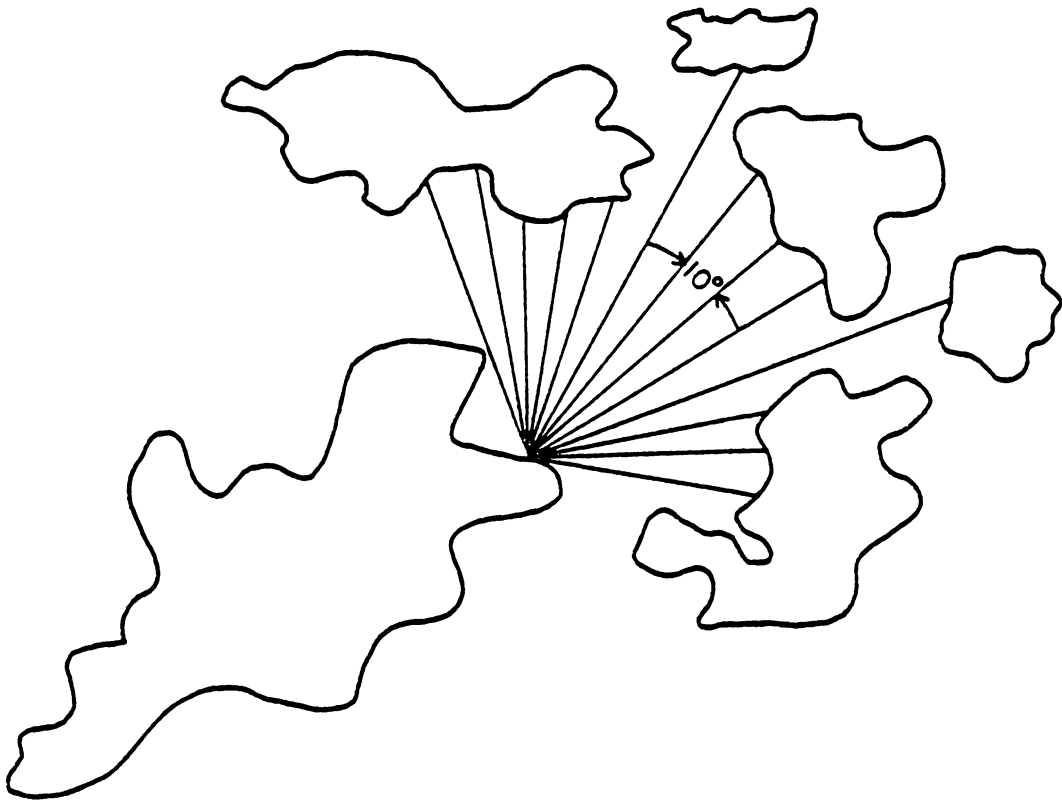


Fig. 5. Measurement of free path distances for mean free path determination using radial grid technique.

photomicrographs that were used to determine the volume fraction of dispersed phase, Eq. I-14 was used to calculate the mean intercept length for each photograph. The values of volume fraction, linear intercept length, and mean free path reported for a given heat-treatment represent overall averages based on the 4 photomicrographs.

#### 5. Phase identification

X-ray diffraction employing standard powdered sample techniques and monochromatized Cu-K $\alpha$  radiation was used for qualitative phase identification. More extensive X-ray results have already been reported (86) on some of the samples in the thermal diffusivity study mentioned previously.

#### 6. Bulk density

Bulk density values were determined by the Archimedes method, with suspended weights obtained with a wire basket immersed in water. The room temperature value of bulk density,  $\rho$ , for each sample was calculated from:

$$\rho = \frac{D}{D-S} \rho_{H_2O} \quad (II-1)$$

where D and S are the dry and suspended weights, respectively, of the sample and  $\rho_{H_2O}$  is the room temperature density of water.

## 7. Young's modulus

Young's modulus values were determined by the sonic pulse method through the courtesy of an outside laboratory.<sup>+</sup> From this technique, Young's modulus, E, was calculated using:

$$E = \rho V^2 \frac{(1+\nu)(1-2\nu)}{1-\nu} \quad (\text{II-2})$$

where, for a given sample,  $\rho$ , V, and  $\nu$  refer, respectively, to the bulk density, the sonic velocity, and Poisson's ratio. A value of 0.25 was assumed for this latter property.

### B. Surface Damage

#### 1. Introduction and measurement of surface damage

Surface flaws were introduced in the polished specimens using a commercial microhardness tester<sup>++</sup> equipped with a Vicker's indenter. Prior to each series of indents, the unit was calibrated with a sample of known hardness provided by the manufacturer of the hardness tester. Total contact time of the indenter with the sample was approximately 25 seconds.

All indentations were made in ambient air. Although indenting in mineral oil would be expected to minimize any moisture-assisted slow crack growth, no significant changes in crack size with time were observed for specimens indented in air. A drop of mineral oil was, however, put on strength specimens following indentation to provide some measurement of protection against damage from surface contact prior to

---

<sup>+</sup> PPG Industries, Inc., Industrial Chemical Dept., Barberton, OH.

<sup>++</sup> Tukon Tester, ACCO Industries, Bridgeport, CT.

breaking, as well as to minimize slow crack growth during strength testing.

Indentations were made over the load range 50 to 1000 grams, with measurements of indent size and crack length being taken on 10-15 indents at each load investigated. For heat-treatments in which indentation data, but not strength values, were obtained, as for the single discs used in the thermal diffusivity study (86), all indentation measurements were made on the single specimen available. In these instances, the repeatability of the data was determined by re-indenting at certain loads and comparing these indentation data with that obtained previously. Repeatability of the means for these samples was found to be within  $\pm 4\%$ . For samples where both strength and indentation data were obtained, as in the case of the heat-treated rods, indentations over the entire load range were made and measured on a single specimen. However, indentations at selected loads were also made on other specimens from the same heat-treatment set to test the replicability of the means. In all instances, good agreement (within  $\pm 7\%$ ) was obtained between the various samples for values of crack length and indent size measured for the same level of indentation load. In cases where a correlation was made between indentation and microstructural parameters, all data were obtained from the same specimen.

Following indentation, the half-diagonal dimension,  $a$ , of the impression was measured using the optical system of the microhardness unit and an eyepiece having a calibrated grid and movable cross-hair.

Crack lengths were measured directly from the viewing screen of the SEM, and converted into true dimensions using the magnification calibration procedure described in the section of this Chapter dealing with quantitative microscopy. Occasionally only 2 or 3 cracks were observed around indents. In these instances, only those cracks actually observed were included in the measurements. Cracks were generally not measured for indents where chipping (removal of material around an indent as a result of intersection of the lateral cracks with the surface) was noted. All crack length data were obtained on samples that had been etched 30 seconds in 5% HF, and then given a gold-coating of 150-200Å to minimize charge-buildup during SEM observation. Cracks made at low loads (<500g) in unetched samples were too narrow and indistinct, especially in the region of the crack tip, to measure with any certainty. Comparison of crack length data for etched and unetched samples indicated etching had a negligible effect on crack length.

The fine texture of the glass-ceramic required that relatively low values of indenter load (typically in the range 50-1000 grams) be employed to obtain crack sizes on the order of the mean free path dimension. Initially, it was thought that the indent cracks introduced in the samples were median cracks, and so the crack dimension,  $c$ , was measured (see Fig. 3a). However, fracture toughness values calculated assuming median crack geometry and using Eq. I-17 or I-20 were either too high or else varied too extensively with load to be meaningful. It became apparent that, for the low ratios of crack-to-indent

size measured at the low loads employed, Palmqvist, rather than median cracks were present in the samples. The Palmqvist crack size,  $l$  (see Fig. 3b), was obtained from measurement of  $c$  and  $a$ , as indicated by Eq. I-19. No significant difference was found in Palmqvist crack size obtained in this manner and that determined by direct measurement.

## 2. Strength behavior

Strength data on indented samples as a function of indentation load were obtained on thin discs, approximately 1 mm. in thickness, that had been sawed from the core-drilled rods. For crystallized samples, the sawing step was performed after heat-treatment. Prior to strength testing, the specimens were polished, annealed 3-4 hours at 650°C to relieve any polishing strains, etched in 5% HF for 30 seconds to minimize the effect on strength of any handling flaws, and then indented.

Strength testing was carried out with a constant cross-head speed mechanical testing machine.<sup>+</sup> A cross-head speed of 0.51 mm.min.<sup>-1</sup> was used for all strength measurements. The resulting loading rate was approximately 20 MPa.s<sup>-1</sup>. Samples were broken in mineral oil to retard slow crack growth. As noted in the preceding Section, the mineral oil was applied immediately after indentation.

The strength apparatus that was used in this study is shown in Figure 6. It is based on the biaxial flexure technique and utilizes the piston-on-3-ball method. Biaxial flexure methods have an advantage

---

<sup>+</sup>Model TTDL, Instron Corp., Canton, MA.

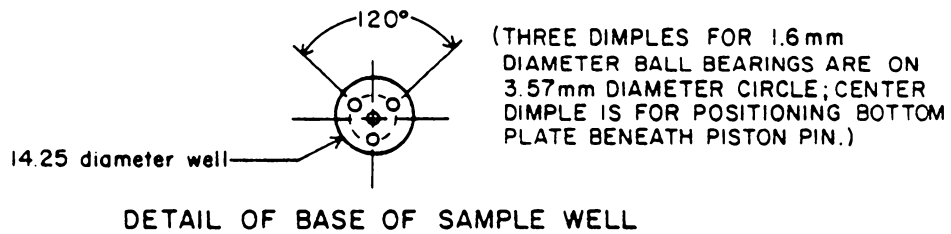
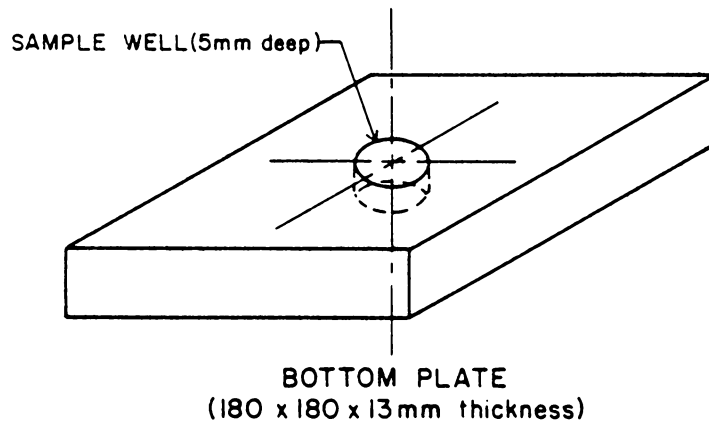
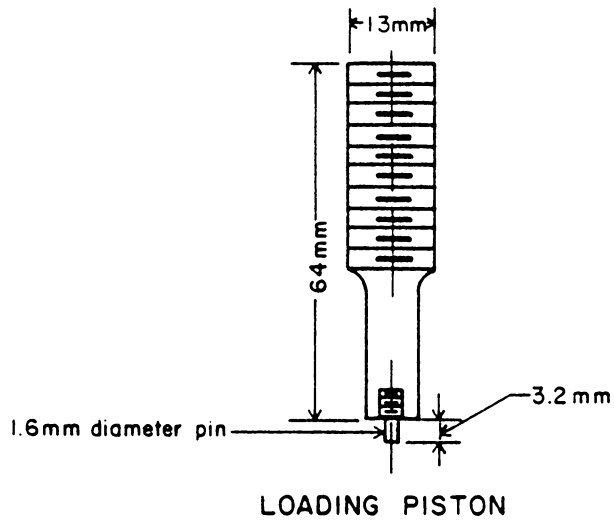


Fig. 6. Biaxial flexure apparatus used to determine strength.

over the uniaxial bend techniques commonly employed to determine strength in that edge effects may be avoided since the region of maximum tensile stress occurs within the centrally-loaded portion of the sample. Ritter et al. (98) have shown that, given sufficient specimen overhang beyond the sample supports, edge stresses during biaxial loading are less than 10% of the maximum central stress. As a result, the spurious failures caused by edge effects encountered with uniaxial loading techniques are eliminated in biaxial flexure methods.

The piston-on-3-ball method for determining strength values was first described by Wachtman et al. (99) and has recently been adopted as a standard ASTM test procedure (100). The apparatus, as shown in Figure 6, consists of 2 main units: a bottom plate which contains 3 ball bearings arranged in shallow dimples equally-spaced about the circumference of a circle (referred to as the specimen support circle), and a piston that has been threaded on one end so as to fit into the upper plate of the mechanical testing machine. The test specimens were supported on the ball bearings, with load being applied to the samples through a small pin located at the tip of the piston. The diameter of this pin defines the size of the region of maximum tensile stress, which occurs at the center of the lower specimen surface. Both the pin and the ball bearings were composed of hardened tool steel. A small dimple, drilled in the center of the sample well in the bottom plate, was used to align the sample well underneath the piston pin.

For the piston-on-3-ball method, the values of the radial and tangential components of stress are equal at the lower surface of the

specimen directly beneath the indenter, with each attaining a maximum tensile value,  $\sigma_{\max}$ , that is given by (101):

$$\sigma_{\max} = \frac{3P}{4\pi t^2} (1+\nu) \left[ 1 + 2 \ln \frac{a}{b} + \frac{1-\nu}{1+\nu} \left\{ 1 - \frac{b^2}{2a^2} \right\} \frac{a^2}{R^2} \right] \quad (\text{II-3})$$

where P is the load on the sample, b is the radius of the piston pin, a is the radius of the support circle, and  $\nu$ , t, and R refer, respectively, to the Poisson's ratio, thickness, and radius of the sample. For the particular jig that was used with a = 3.57 mm. and b = 0.8 mm., and assuming  $\nu = 0.25$ , Eq. II-3 simplifies to:

$$\sigma_{\max} = \frac{P}{t^2} \left[ 1.19 + \frac{2.22}{R^2} \right] \quad (\text{II-4})$$

Strength values were determined from Eq. II-4 for specimens placed in the test apparatus such that the polished (indented) side of the specimen was the lower or tensile surface during testing. Equating  $\sigma_{\max}$  to breaking strength assumes that the indentation flaws (presumed to be the failure-initiating flaws) were located within the central circular region (equal in diameter to the 1.6 mm. diameter of the piston pin) within which the maximum tensile stress occurs. To accomplish this, care was taken to assure that indentations were made in the center of the test specimens, and that these test specimens were, in turn, centered in the strength apparatus beneath the piston pin.

Centering of the indent on the sample was accomplished using a sample holder consisting of an aluminum plate containing a shallow cylindrical well with a diameter slightly larger than the 13.0 mm.

diameter of the specimens. The well was first centered beneath the Vicker's indenter (by focusing on a small dimple drilled at the center of the well), so that when a specimen was placed within the well, any indentation would be made in the center of the test specimen. Positioning of the indented test specimens in the strength apparatus such that indents would lie directly below the piston pin was achieved with an aluminum ring of 0.25 mm. thickness placed concentrically within the strength jig's sample well (see Figure 6). Reducing the 14.25 mm. well diameter by 0.50 mm. in this manner is sufficient to assure that indents made in the center of the test specimens will lie within 0.8 mm. from the center of the piston pin, and thus be subjected to the maximum tensile stress.

### III. EXPERIMENTAL RESULTS

#### A. Preliminary Characterization

##### 1. Phase identification and microstructural analysis

As noted, several of the same glass-ceramic specimens used in this investigation had also been utilized in a previous thermal diffusivity study (86). X-ray diffraction results (86) reported for these specimens show the following quantitative relationship (vol.% basis):

820°C/2h + 1000°C/8h

stuffed quartz	(85-90)
spinel	(5-10)
enstatite, MgO·SiO <sub>2</sub>	(5)
glass	(2-5)

820°C/2h + 1260°C/8h

α-cordierite	(70-80)
MgO·2TiO <sub>2</sub>	(10-15)
low cristobalite	(10-15)

X-ray diffraction analyses performed for this Dissertation are in agreement, essentially, with the above data, as well as with literature results cited in the preceding Chapter. Stuffed quartz was the first crystalline phase to appear, and was present, along with a glassy phase in samples crystallized at 905°C/8h. Stuffed quartz was present in substantial quantity, along with minor amounts of spinel, following a 1000°C/8h crystallization. No glassy phase (as indicated by the absence of base-line roll) was detected. For heat-treatments at 1100°C/2h, 1150°C/8h, and 1260°C/8h, the major

phase present was  $\alpha$ -cordierite, with minor quantities detected of low cristobalite and pseudo-brookite, a solid solution involving  $\text{MgO} \cdot 2\text{TiO}_2$  and  $\text{Al}_2\text{O}_3 \cdot \text{TiO}_2$ . With increasing crystallization temperature for these latter heat treatments, the percentage of  $\alpha$ -cordierite decreased slightly, while that of the pseudo-brookite phase increased, using X-ray peak intensities as an approximate quantitative indicator. No crystalline reflections were observed in the diffraction pattern of either the original glass or a specimen which received only the  $820^\circ\text{C}/2\text{h}$  nucleation treatment. However, a slight opalescence was detected in both samples. This was caused, presumably, by a glass-in-glass phase separation. As noted in the preceding Chapter, phase separation in this system has been observed following cooling from the melt during the glass-forming process, as well as with subsequent heating to about  $800^\circ\text{C}$ . No phase separation could be resolved, however, in SEM micrographs taken of either the original glass or  $820^\circ\text{C}/2\text{h}$  specimens.

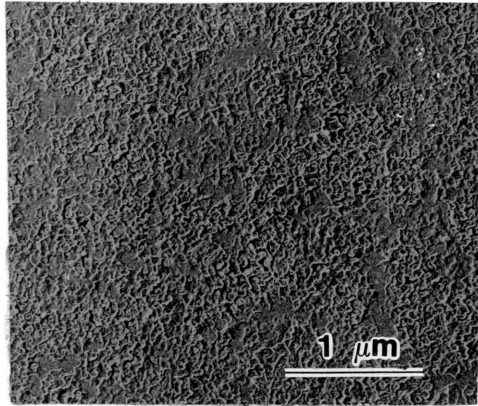
As indicated by the X-ray results, the stuffed quartz  $\rightarrow$   $\alpha$ -cordierite transformation occurs over a relatively narrow time/temperature interval with approximate heat-treatment end-points of  $1000^\circ\text{C}/8\text{h}$  and  $1100^\circ\text{C}/2\text{h}$ . A crystallization treatment made at  $1100^\circ\text{C}/1\text{h}$ , selected since it was intermediate to these end-points, showed stuffed quartz as the major phase, with minor amounts detected of spinel and a trace quantity of  $\alpha$ -cordierite. At  $1100^\circ\text{C}$ , then, the transformation begins after approximately 1 hour and is completed within an additional hour.

Electron micrographs taken of several of the samples are shown in Figure 7. A replica transmission electron micrograph<sup>\*</sup>, taken during the thermal diffusivity study (86), is shown in Figure 7a for a sample which received a crystallization heat-treatment of 8 hours at 905°C. This microstructure, characteristic of all samples heat-treated below the stuffed quartz  $\rightarrow$   $\alpha$ -cordierite transformation, consists of a uniform dispersion of very fine-grained crystallites (predominantly stuffed quartz) that are well below 0.1  $\mu\text{m}$  in size. Samples heat treated above the transformation have a microstructure typified by that shown in Figure 7b for a specimen which received a 1200°C/8h crystallization treatment. This microstructure consists of a dispersed crystalline phase, several microns in size, embedded in a much finer-grained crystalline matrix. On the basis of the photomicrograph and the X-ray diffraction results, the dispersed phase is predominantly  $\alpha$ -cordierite, while the fine-grained matrix is composed of an admixture of  $\alpha$ -cordierite, low-cristobalite and the pseudo-brookite phase. In subsequent discussion, the different microstructures shown in Figures 7, a and b, will be referred to, respectively, as the "fine-precipitate" and the "large-crystallite" or coarse microstructure.

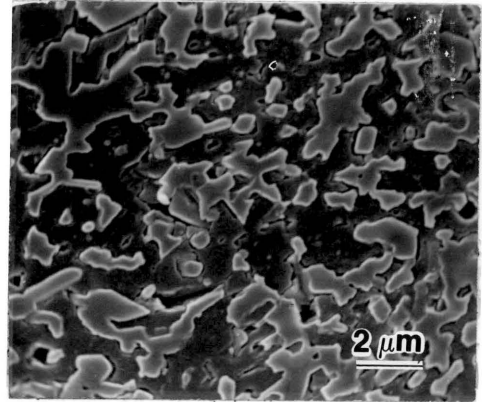
Photomicrographs taken during and immediately following the stuffed quartz  $\rightarrow$   $\alpha$ -cordierite transformation are shown in Figures 7c and 7d for specimens crystallized, at 1100°C/1h and 1100°C/2h, respectively. The microstructure of the 1100°C/1h specimen (in which trace amounts

---

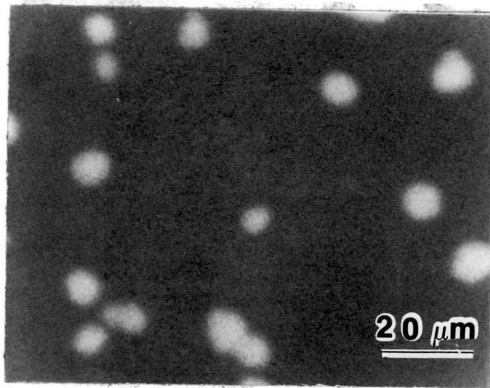
\*The other electron micrographs in Fig. 7 were taken with the SEM.



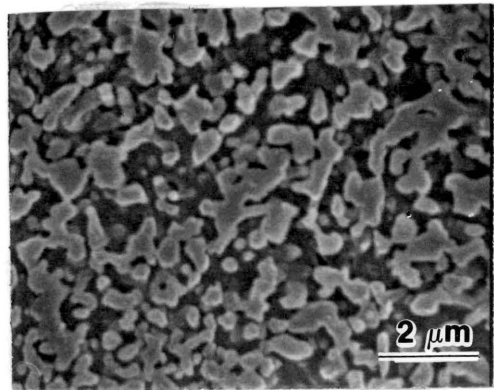
(a)



(b)



(c)



(d)

Fig. 7. Electron micrographs of cordierite glass ceramic initially heat-treated at 820°C for 2h followed by further treatment at a, 905°C for 8h; b, 1200°C for 8h; c, 1100°C for 1h; and d, 1100°C for 2h.

of  $\alpha$ -cordierite were detected in the X-ray diffraction analysis) shows what presumably are regions, or nuclei, within the fine-grained stuffed quartz phase where the transformation has been initiated. The microstructure for the 1100°C/2h sample (in which no remaining stuffed quartz phase was detected by X-ray diffraction) shows the large crystallite microstructure characteristic of samples heated above the transformation.

## 2. Young's modulus and bulk density

Young's modulus values, obtained for various heat treatments, are shown in Table II. Also appearing in this Table are the bulk density values used in the calculation of the Young's modulus from the sonic pulse measurements. Both Young's modulus and bulk density were determined on the same samples.

The value of  $103\text{GNm}^{-2}$  obtained for the original glass and the value of about  $130\text{GNm}^{-2}$  measured for the fully-crystallized samples agree well with data measured elsewhere (102). Young's modulus is seen to be relatively unchanged by either the nucleation process ( $103\text{GNm}^{-2}$ ) or the start of the stuffed quartz crystallization ( $106\text{GNm}^{-2}$ ). Complete crystallization of the glass to form stuffed quartz produces a substantial increase in Young's modulus ( $129\text{GNm}^{-2}$ ). Both the subsequent crystalline transformation and further heat-treatment of the resulting  $\alpha$ -cordierite phase have no significant effect on Young's modulus, with relatively constant values in the range  $131\text{-}134\text{GNm}^{-2}$  obtained.

TABLE II. YOUNG'S MODULUS AND BULK DENSITY FOR VARIOUS  
HEAT-TREATMENTS OF CORDIERITE GLASS-CERAMIC

<u>Heat-Treatment (Temp. and Time)</u>	<u>Bulk Density (g·cm<sup>-3</sup>)</u>	<u>Sonic Velocity (10<sup>5</sup>cm·s<sup>-1</sup>)</u>	<u>Young's Modulus (GNm<sup>-2</sup>)</u>
Original Glass	2.65	6.83	103
820°C/2h	2.64	6.85	103
820°C/2h + 905°C/8h	2.66	6.92	106
820°C/2h + 1000°C/8h	2.98	7.19	129
820°C/2h + 1100°C/1h	3.00	7.32	134
820°C/2h + 1100°C/8h	2.69	7.71	133
820°C/2h + 1260°C/8h	2.65	7.69	131

Bulk density is seen to undergo a pronounced maximum with heat treatment. This property increases dramatically (from 2.65 to 2.98  $\text{g}\cdot\text{cm}^{-3}$ ) with complete crystallization of the glass into stuffed quartz, and then decreases precipitously (from 3.00 to 2.65  $\text{g}\cdot\text{cm}^{-3}$ ) following transformation of the stuffed quartz phase to  $\alpha$ -cordierite. These drastic changes agree well with apparent density data reported by Kumar and Nag (103) and reflect the differences in atomic packing between the tightly packed stuffed quartz structure and the far more open silicate glass and  $\alpha$ -cordierite configurations.

### 3. Quantitative microscopy

Volume fraction and free path values, measured for the large crystallite heat treatments, are shown in Table III, along with the value of mean linear intercept length calculated from the Fullman expression, Eq. I-14. The microstructural detail in the fine-precipitate heat-treatments was too small ( $< 0.1 \mu\text{m}$ ) to permit any reliable quantitative characterization.

Data appear in Table III for 2 separate series of samples: the individual discs obtained from the thermal diffusivity study (86), and specimens cut from the core-drilled rods that had been heat treated for subsequent indentation and strength work. Specimens from this latter group will be distinguished by the designation "strength series" following the heat treatment description.

The data in Table III indicate that the dispersed phase decreases in volume fraction, yet increases in crystallite size, with increasing degree of heat-treatment. This effect may be seen by comparing the

TABLE III. MICROSTRUCTURAL PARAMETERS OF DISPERSED PHASE FOR  
VARIOUS CRYSTALLIZATION HEAT TREATMENTS OF CORDIERITE GLASS-CERAMIC

<u>Heat-Treatment</u> <u>(temp. and time)*</u>	<u>Volume</u> <u>Fraction</u>	<u>Mean Free Path</u> <u>(<math>\mu\text{m}</math>)</u>	<u>Mean Linear</u> <u>Intercept Length (<math>\mu\text{m}</math>)</u>
1100°C/2h	0.622 $\pm$ 0.114	0.38 $\pm$ 0.23	0.62
1100°C/8h	0.585 $\pm$ 0.107	0.61 $\pm$ 0.34	0.87
1150°C/8h	0.492 $\pm$ 0.130	1.07 $\pm$ 0.67	1.04
1150°C/8h (Strength Series)	0.535 $\pm$ 0.109	1.11 $\pm$ 0.67	1.31
1200°C/8h (Strength Series)	0.455 $\pm$ 0.151	1.26 $\pm$ 0.71	1.05
1260°C/8h	0.483 $\pm$ 0.120	1.70 $\pm$ 1.02	1.58
1260°C/8h (Strength Series)	0.480 $\pm$ 0.129	1.68 $\pm$ 0.90	1.56

\* Following 820°C/2h nucleation treatment.  
Values shown are mean  $\pm$  standard deviation.

photomicrographs of specimens crystallized at 1100°C/2h and 1200°C/8h, shown in Figures 7d and 7b, respectively. Gregory and Veasey (91) report that continued heat treatment of cordierite glass-ceramics results in the growth of progressively larger  $\alpha$ -cordierite crystals from a very fine-grained crystalline matrix. However, no comment was made by them concerning concurrent changes in volume fraction. The X-ray diffraction results reported earlier in this Chapter do imply that a decrease in volume fraction of the major phase,  $\alpha$ -cordierite, occurs with increasing degree of heat treatment. These seemingly opposing trends of decreasing volume fraction and increasing crystallite size are difficult to rationalize from the discussion on crystallization kinetics in glass ceramics presented in Chapter I, and are related, presumably, to differences in number of nuclei occurring with heat-treatment. It should be noted that the microstructural changes evident in Table III (i.e., increasing crystallite size and decreasing volume fraction) occur after complete crystallization of the glass, and involve solid state processes distinct from any glass crystallization phenomena.

## B. Surface Damage

### 1. Effect of experimental method on measured crack size

As noted in the Chapter on Experimental Procedure, the indented glass-ceramic samples were etched 30 seconds in hydrofluoric acid prior to measuring cracks. The effect of etching time in HF on crack size is shown in Table IV for a series of 100 gram indents made in the same

TABLE IV. EFFECT OF ETCHING TIME IN 5% HF ON SIZE OF  
INDENT CRACKS IN ORIGINAL GLASS OF CORDIERITE GLASS-CERAMIC

	Etching Time (seconds) in 5% HF					
	<u>0</u>	<u>10</u>	<u>20</u>	<u>30</u>	<u>40</u>	<u>50</u>
Crack Size, c(μm)	(too indis- tinct to measure)	13.14± 1.33	13.43± 1.23	13.56± 0.95	13.61± 0.86	13.69± 0.69

Note: all data obtained from same specimen using indent load of 100g, with 48 data points measured for each etching time; indicated uncertainty is ±1 standard deviation.

#### ANALYSIS OF VARIANCE

<u>Source of Variation</u>	<u>Degrees of Freedom</u>	<u>Sum of Squares</u>	<u>Mean Square</u>
Between Groups	4	205.94	76.49
Within Groups	235	9834.46	41.85

$$F_{\text{calc}} = \frac{\text{Mean Square (Between Groups)}}{\text{Mean Square (Within Groups)}} = 1.83$$

At 95% Confidence Level,  $F_{.95}(4,235) = 2.41$ . Since  $F_{\text{calc}} < F_{.95}$ , we conclude that there is insufficient evidence to demonstrate that changes in etching time produce a significant variation in crack size.

specimen of the original glass. Each series of indents was measured immediately after etching, with approximately 2 hours elapsing between the indentation and measurement operations. Etching times ranging from 0 to 50 seconds were employed. The cracks in the unetched set of indents, although present, were too indistinct to measure in the SEM. Were etching to lead to enhanced crack growth, a noticeable increase in crack size would be expected to occur with increasing etching time. Although a slight increase was observed in mean crack size with increased etching time, this increase, on the basis of an Analysis of Variance test (104), was found to not be significant at the 95% Confidence level. It is concluded, accordingly, that etching in HF does not cause a significant increase to occur in crack size, at least for etching times  $\leq 50$  seconds. Instead, it appears that etching reduces experimental scatter in crack size measurements, presumably by widening the cracks and thus making them more clearly defined.

The effect of any slow crack growth on crack size following indenting in ambient air is seen in Table V. Crack size data are reported for a series of 500 gram indents made in the same specimen of the original glass. Cracks were measured almost immediately after having been introduced (i.e., within 0.5h), and as long as 24 and 48 hours following indentation. The lowest time after indenting listed, 0.5h, corresponds to the minimum time needed to make a series of indents, etch and gold-coat them, and observe them in the SEM. Measurements were also made on a series of unetched cracks at 0.5h after indentation. At the relatively high level of indenter load used in this experiment, unetched cracks were reasonably easy to discern.

TABLE V. EFFECT OF POST-INDENTATION TIME ON SIZE OF INDENT CRACKS  
IN ORIGINAL GLASS OF CORDIERITE GLASS-CERAMIC

	<u>Post-Indentation Time (hours)</u>			
	<u>0.5</u>	<u>0.5</u>	<u>24</u>	<u>72</u>
Condition	unetched	etched	etched	etched
Crack Size,	46.7	48.3	47.7	49.4
c (µm)	±7.56	±4.98	±4.58	±4.87

Note: all data obtained from same specimen using indent load of 500g., with 40 data points measured for each post-indentation time; indicated uncertainty is ±1 standard deviation.

#### ANALYSIS OF VARIANCE

(1) for all 4 sets

<u>Source of Variation</u>	<u>Degrees of Freedom</u>	<u>Sum of Squares</u>	<u>Mean Square</u>
Between Groups	3	56.93	18.98
Within Groups	156	1833.84	11.76

$$F_{\text{calc}} = \frac{\text{Mean Square (Between Groups)}}{\text{Mean Square (Within Groups)}} = 1.61$$

At 95% Confidence Level,  $F_{.95}(3,156) = 2.66$ . Since  $F_{\text{calc}} < F_{.95}$ , we conclude that there is insufficient evidence to demonstrate that a significant difference in crack size exists between the four sets.

(continued on next page)

TABLE V. EFFECT OF POST-INDENTATION TIME ON SIZE OF INDENT CRACKS  
IN ORIGINAL GLASS OF CORDIERITE GLASS-CERAMIC (Cont'd)

ANALYSIS OF VARIANCE

(2) for the etched sets

<u>Source of Variation</u>	<u>Degrees of Freedom</u>	<u>Sum of Squares</u>	<u>Mean Square</u>
Between Groups	2	21.72	10.86
Within Groups	117	999.87	8.55

$$F_{\text{calc}} = \frac{\text{Mean Square (Between Groups)}}{\text{Mean Square (Within Groups)}} = 1.27$$

At 95% Confidence Level,  $F_{.95}(2,117) = 3.07$ . Since  $F_{\text{calc}} < F_{.95}$ , we conclude that there is insufficient evidence to demonstrate that changes in post-indentation time produce a significant variation in crack size.

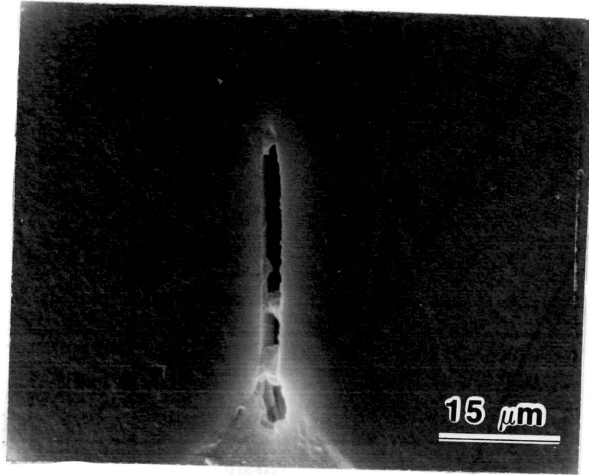
Were slow crack growth effects to play a role in influencing crack size for indents made in air, a noticeable increase would be expected to occur in measured crack size with increasing post-indentation time. Using an Analysis of Variance test, post-indentation time is seen to have no significant effect (at the 95% Confidence Level) on measured crack size. It is concluded that slow crack growth behavior associated with indenting in ambient air does not exert a major influence on crack size, at least for post-indentation times  $\leq 48$  hours.

The above conclusion disagrees with findings reported by Gupta and Jubb (105) for radial cracks in soda-lime-silica glass. These investigators reported slow growth of radial cracks after indentation. However, only average values of crack size were reported in their study, with no statistical analysis performed on the significance of the observed trends in crack size with time. Post-indentation growth of radial cracks in glass has also been reported by Smith et al. (106), who observed slow crack growth even for indents made in mineral oil. In both of these studies, no etching operation was performed since the cracks were readily visible at the high levels (1.5-3 kg) of indenter load employed. It may well be that etching, by increasing the crack-tip radius of curvature and, in effect, causing crack blunting to occur, may, as a consequence, reduce susceptibility to slow crack growth.

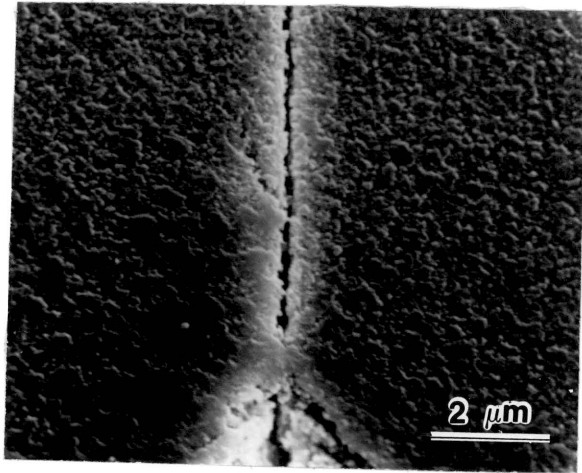
## 2. Indentation parameters for the original glass and samples with the fine-precipitate microstructure

Electron micrographs of a typical indentation crack in the original glass and in a sample crystallized at  $1000^{\circ}\text{C}$  for 8 hours are shown in Figure 8. In each photograph, the cracks appear continuous along the specimen surface and, as indicated by the absence of deflection or pinning phenomena, do not interact at all with any microstructural features. The samples essentially behave as a continuum for crack-related processes.

Data on median crack size,  $c$ , and indent half-diagonal,  $a$ , at various indenter loads are listed in Table VI for the original glass and the fine precipitate samples. As noted in the Chapter dealing with Experimental Procedure, crack sizes were measured for median cracks, i.e., the surface extension of the crack was measured from the center of the indent to the crack-tip (see Figure 3a). However, Palmqvist cracks, as discussed in Chapter I, are presumed to describe more accurately than median cracks the actual crack configuration present in these glass-ceramic samples at the low levels of indenter load employed. The Palmqvist crack size, which is the distance,  $\ell$ , measured along the crack from the corner of the indent to the crack tip (see Figure 3b), may be calculated, according to Eq. I-19, by taking the difference of  $c$  and  $a$ . The Palmqvist crack size is plotted on a  $\ln$ - $\ln$  scale as a function of indenter load in Figure 9 for the original glass and the fine-precipitate samples. From Table VI, the variation in half-diagonal length is generally substantially less than



(a)



(b)

Fig. 8. SEM micrographs showing indentation cracks for cordierite glass-ceramic for: a, original glass; and b, specimen heat-treated at 820°C/2h plus 1000°C/8h.

TABLE VI. EXPERIMENTAL INDENTATION DATA FOR CORDIERITE GLASS-CERAMIC  
FOR THE ORIGINAL GLASS AND THE FINE-PRECIPITATE SAMPLES

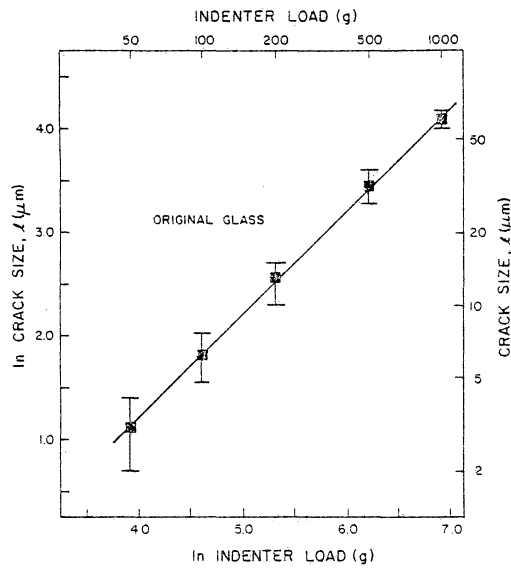
Heat-Treatment (Temp. and Time)	Indentation Load (g.)						
	<u>50</u>	<u>100</u>	<u>200</u>	<u>350</u>	<u>500</u>	<u>750</u>	<u>1000</u>
Original Glass							
half-diagonal, a(μm)	5.00±0.30 (22)	7.31±0.30 (26)	10.5±0.51 (24)		17.1±0.61 (24)		25.4±0.63 (22)
crack size, c(μm)	8.00±1.00 (38)	13.4 ±1.42 (43)	23.1±2.11 (45)		48.5±4.69 (43)		85.1±5.32 (38)
820°C/2h							
half-diagonal, a(μm)	5.21±0.11 (24)	7.61±0.35 (24)	11.0±0.31 (24)		17.6±0.38 (24)		25.2±0.41 (24)
crack size, c(μm)	8.71±0.54 (48)	14.7 ±2.34 (46)	22.3±1.08 (42)		49.8±4.58 (40)		83.9±6.56 (40)
820°C/2h+905°C/8h							
half-diagonal, a(μm)	4.92±0.20 (24)	6.79±0.25 (24)	10.1±0.33 (24)		16.5±0.42 (24)		23.7±0.48 (24)
crack size, c(μm)	7.77±1.07 (37)	12.1 ±0.92 (42)	21.0±2.09 (45)		40.0±3.38 (45)		68.1±5.06 (46)
820°C/2h+1000°C/8h							
half-diagonal, a(μm)	4.21±0.21 (24)	6.20±0.42 (24)	9.12±0.40 (24)		14.8±0.42 (24)		21.5±0.51 (24)
crack size, c(μm)	7.22±0.80 (38)	11.6±1.21 (46)	19.9±2.01 (46)		44.4±3.59 (48)		73.8±7.82 (48)

(continued next page)

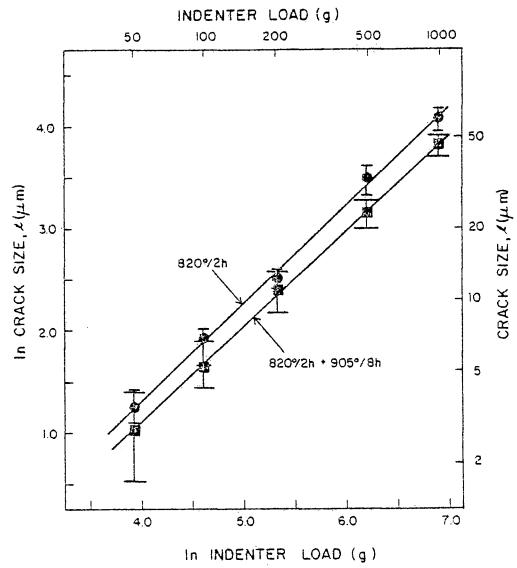
TABLE VI. (Continued)

Heat-Treatment Temp. and Time	Indentation Load (g.)						
	<u>50</u>	<u>100</u>	<u>200</u>	<u>350</u>	<u>500</u>	<u>750</u>	<u>1000</u>
820°C/2h+1000°C/8h (strength series)							
half-diagonal, a(μm)	4.51±0.40 (20)	6.59±0.38 (20)	9.48±0.50 (20)	12.8±0.38 (20)	15.9±0.38 (20)	19.6±0.48 (20)	23.1±0.42 (20)
crack size, c(μm)	7.69±0.82 (36)	12.1±1.81 (37)	20.7±3.13 (38)	36.9±5.42 (40)	48.6±7.83 (34)	62.8±5.04 (38)	76.3±10.9 (40)
820°C/2h+1100°C/1h							
half-diagonal, a(μm)	4.13±0.20 (24)	5.91±0.23 (24)	8.78±0.40 (24)		14.3±0.32 (24)		20.7±0.51 (24)
crack size, c(μm)	6.42±1.11 (44)	10.7±1.92 (47)	18.1±2.31 (41)		37.0±7.61 (48)		65.6±10.6 (48)

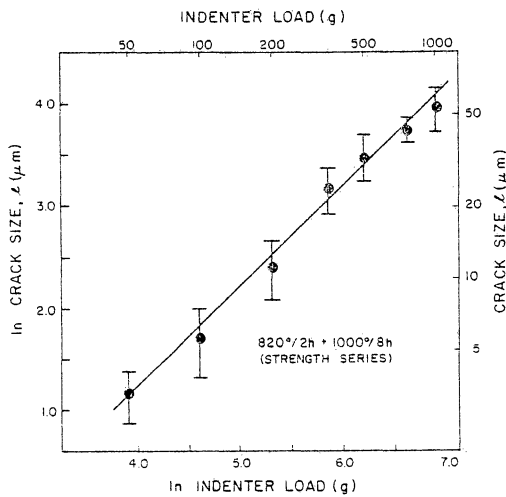
Values shown are mean ± 1 standard deviation; figure in parenthesis is number of data points obtained at each load.



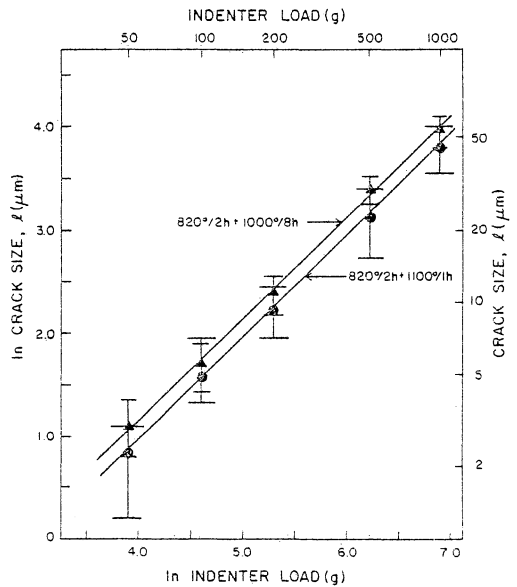
(a)



(b)



(c)



(d)

Fig. 9. Crack size as a function of indenter load for cordierite glass-ceramic for: a, original glass; and specimens heat-treated at B, 820°C/2h and 820°C/2h plus 905°C/8h; c, 820°C/2h plus 1000°C/8h (strength series); and d, 820°C/2h plus 1000°C/8h and 820°C/2h plus 1100°C/1h. (Indicated error bars represent  $\pm 1$  estimated standard deviation from the mean.)

the variation in median crack size. As a result, the mean values of Palmqvist crack size that are plotted in Figure 9 were obtained from the difference in the individual means of  $c$  and  $a$ . Similarly, the standard error in the measured median crack sizes was used to approximate the standard deviation of  $\ell$ . The range of uncertainty shown in Figure 9 for the Palmqvist crack size is  $\pm$  one standard deviation.

The plots of crack size shown in Figure 9 are linear and continuous across the whole range of loads investigated. Little or no difference appears to exist for all the samples shown with respect to the value of crack size at any given load. The results of linear regression analyses of these data are listed in Table VII. The expected value of slope for a  $\ln$ - $\ln$  plot of Palmqvist crack size versus indenter load, as reported by several investigators (62,63), is unity. The actual slopes, listed in Table VII for these heat-treatments of the glass-ceramic, agree quite well with the literature value, and range from 0.917 to 1.00

### 3. Indentation parameters for samples with the large crystallite microstructure

The experimental data for median crack size,  $c$ , and half-diagonal length,  $a$ , are listed as a function of load in Table VIII. Electron micrographs of typical indentation cracks made at low and high loads in the large crystallite samples are shown in Figure 10 for the glass-ceramic crystallized at  $1150^{\circ}\text{C}$  for 8 hours. At low levels of indentation load (Figures 10, a and b), the crack is contained entirely within

TABLE VII. LINEAR REGRESSION ANALYSIS OF PALMQVIST CRACK SIZE AS A FUNCTION OF LOAD FOR CORDIERITE GLASS-CERAMIC FOR THE ORIGINAL GLASS AND THE FINE-PRECIPIRATE SAMPLES

Heat-Treatment (Temp. and Time)	$\ln \ell = m \ln P + b$		
	Slope, <u>m</u>	Intercept, <u>b</u>	Correlation Coefficient
Original Glass	1.00	-2.80	1.00
820°C/2h	0.944	-2.45	0.998
820°C/2h + 905°C/8h	0.917	-2.53	1.00
820°C/2h + 1000°C/8h	0.981	-2.77	0.999
820°C/2h + 1000°C/8h (strength series)	0.985	-2.73	0.996
820°C/2h + 1100°C/1h	0.990	-3.00	0.999

Above analyses for Palmqvist crack size,  $\ell$ , in microns, and indenter load, P, in grams; data for load range, 50g.  $\leq P \leq 1000$ g.

TABLE VIII. EXPERIMENTAL INDENTATION DATA FOR CORDIERITE GLASS-CERAMIC FOR THE LARGE CRYSTALLITE SAMPLES

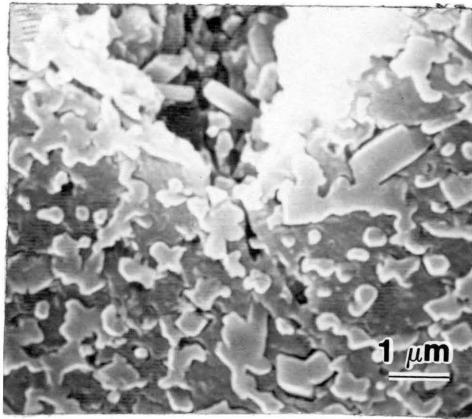
Heat-Treatment (Temp. and Time)	I N D E N T A T I O N L O A D (GRAMS)												
	<u>50</u>	<u>60</u>	<u>75</u>	<u>100</u>	<u>125</u>	<u>150</u>	<u>175</u>	<u>200</u>	<u>250</u>	<u>325</u>	<u>500</u>	<u>1000</u>	
820°C/2h+1100°C/2h													
half-diagonal, a(μm)	4.60±0.38 (24)	5.21±0.35 (24)	5.93±0.24 (24)	6.91±0.24 (24)				10.0±0.41 (24)			16.0±0.32 (24)	23.0±0.35 (24)	
crack size, c(μm)	7.71±1.45 (48)	8.72±1.31 (44)	10.5±1.18 (44)	11.3±1.67 (48)				18.0±1.87 (47)			34.8±3.97 (48)	57.6±7.49 (46)	
820°C/2h+1100°C/8h													
half-diagonal, a(μm)	4.92±0.35 (24)			7.08±0.42 (24)	8.20±0.34 (24)	9.00±0.40 (24)	9.82±0.40 (24)	10.5±0.40 (24)			17.0±0.51 (24)	24.2±0.31 (24)	
crack size, c(μm)	7.12±0.96 (39)			11.6±2.02 (39)	13.6±2.15 (47)	13.2±1.83 (44)	14.8±2.34 (47)	16.8±2.44 (40)			33.6±4.94 (47)	56.7±7.03 (45)	
820°C/2h+1150°C/8h													
half-diagonal, a(μm)	4.91±0.20 (24)			7.01±0.38 (24)	8.32±0.40 (24)	9.20±0.35 (24)		10.5±0.40 (24)	12.0±0.29 (24)	13.8±0.43 (24)	16.8±0.39 (22)	24.0±0.41 (24)	
crack size, c(μm)	7.11±1.10 (38)			11.6±2.00 (41)	14.3±2.33 (44)	13.8±1.90 (40)		15.1±2.60 (42)	17.6±2.75 (44)	21.8±2.92 (44)	28.4±4.80 (46)	51.5±7.36 (48)	

(continued on next page)

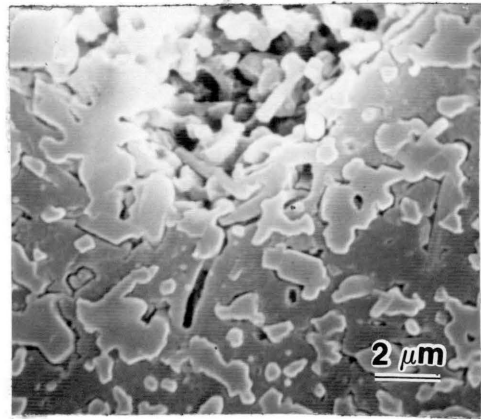
TABLE VIII. (Cont'd) EXPERIMENTAL INDENTATION DATA FOR CORDIERITE GLASS-CERAMIC FOR THE LARGE CRYSTALLITE SAMPLES

Heat-Treatment (Temp. and Time)	I N D E N T A T I O N L O A D (GRAMS)																
	50	75	100	125	150	200	225	250	275	300	325	350	425	500	650	750	1000
820°C/2h+1150°C/8h (strength series)																	
half-diagonal, a(μm)	5.31±0.42 (24)	6.58±0.40 (24)	7.59±0.30 (24)	8.59±0.30 (24)		10.9±0.20 (24)								17.3±0.40 (24)			24.5±0.39 (24)
crack size, c(μm)	7.72±1.32 (44)	10.1±1.60 (42)	12.6±1.98 (42)	12.4±1.98 (47)		16.4±2.48 (42)								30.0±3.84 (46)			46.8±3.79 (44)
820°C/2h+1200°C/2h (strength series)																	
half-diagonal, a(μm)	5.46±0.43 (20)		7.65±0.39 (20)			11.2±0.48 (20)		12.3±0.44 (20)	13.4±0.61 (20)	13.8±0.35 (20)	14.1±0.58 (20)	15.0±0.69 (20)		17.7±0.50 (20)	20.2±0.49 (20)	21.8±0.51 (20)	25.4±0.63 (20)
crack size, c(μm)	7.65±1.61 (39)		11.9±2.25 (38)			18.7±2.59 (40)		23.2±3.46 (39)	23.3±3.04 (39)	22.8±3.07 (38)	23.4±2.69 (39)	25.7±2.83 (40)		31.7±3.09 (40)	37.5±3.36 (36)	40.9±3.75 (40)	49.2±4.22 (40)
820°C/2h+1260°C/8h (strength series)																	
half-diagonal, a(μm)	5.44±0.44 (20)	6.55±0.41 (20)	7.82±0.52 (20)		9.69±0.44 (20)	11.0±0.56 (20)	11.9±0.41 (20)	12.5±0.56 (20)	13.0±0.40 (20)	13.6±0.43 (20)	14.1±0.42 (20)	14.8±0.36 (18)	16.7±0.42 (20)	18.2±0.44 (20)		22.4±0.47 (20)	26.0±0.60 (20)
crack size, c(μm)	7.51±1.33 (37)	9.59±1.50 (37)	11.6±1.55 (39)		15.2±2.10 (36)	18.9±2.49 (39)	20.8±2.52 (39)	20.6±2.22 (39)	20.5±2.10 (39)	22.0±2.31 (39)	21.6±2.51 (39)	21.8±2.79 (34)	26.0±3.49 (40)	29.9±2.8 (38)		38.6±4.71 (40)	47.7±5.20 (39)

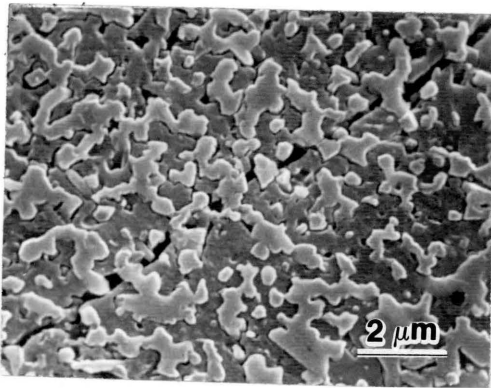
Note: Values shown are mean ± 1 standard deviation; figure in parenthesis indicates number of data points measured at each load.



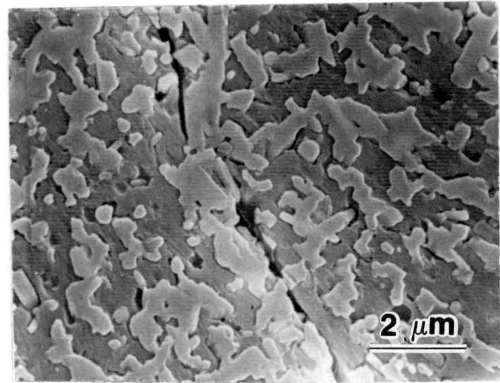
(a)



(b)



(c)



(d)

Fig. 10. SEM micrographs of cordierite glass-ceramic heat-treated at 820°C/2h plus 1150°C/8h showing indentation crack at indenter load of: a, 75g; b, 100g; c, 500g; and d, 1000g.

the fine-grained matrix and does not interact, to any appreciable extent, with the dispersed phase. This behavior can be rationalized entirely from geometric considerations, since at sufficiently low loads, the Palmqvist crack size is less than the mean free path distance between the dispersed crystallites. At much higher levels of indentation load (Figures 10, c and d), the indent cracks are large enough that they are several multiples of the mean free path dimension in length. As a consequence, the cracks will encounter at least several dispersed crystallites along their paths. The predominant type of crack-inclusion interaction which results from these encounters is crack deflection by the dispersed phase. In these latter two photomicrographs, the crystallites are seen to act as obstacles to crack propagation, with the crack forced to go below or around the inclusion. Unlike the low-load regime where crack introduction and propagation were found to be matrix-determined, these same processes in the high-load regime are controlled by the composite response of the material.

The differences seen in Figure 10 between the two sets of micrographs with respect to the nature of the crack-microstructure interaction occurring at low and high loads are also expressed in Figure 11, where plots of crack size as a function of load are shown for the various large crystallite heat treatments. For each sample, the crack size data fall into two distinct groupings, a low load set and a high load set, separated by a discontinuity or transition region across which crack size actually decreases with increasing load. These

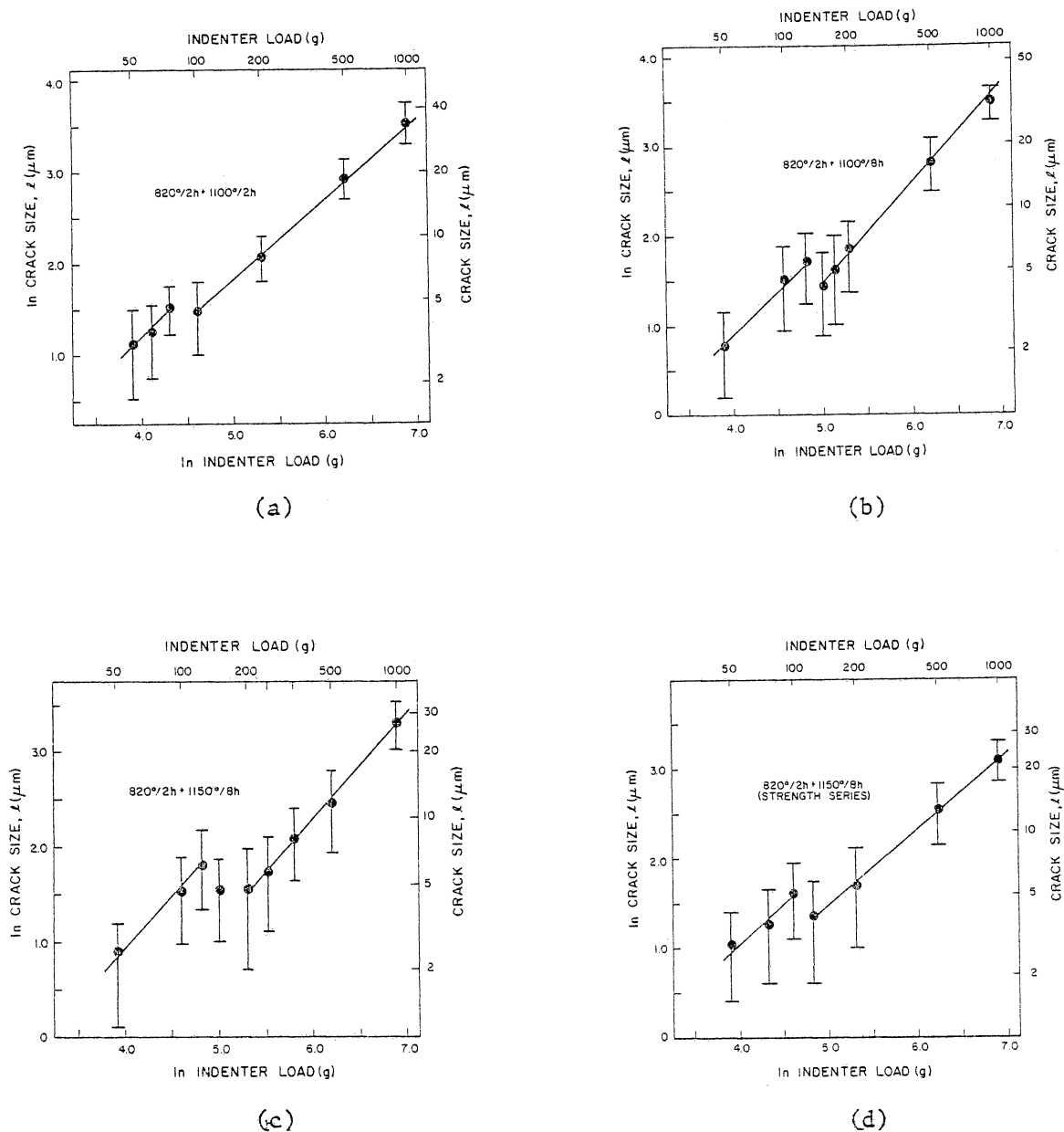
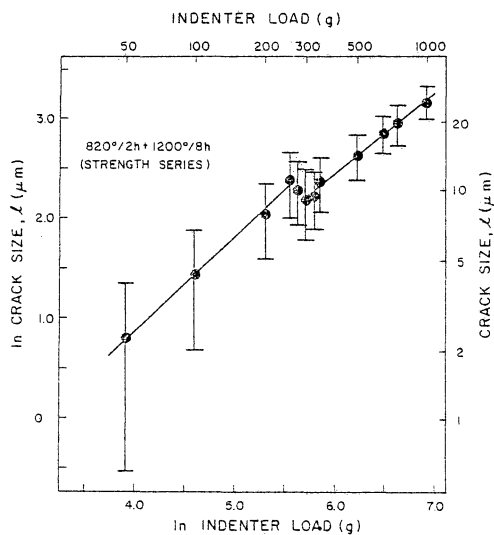
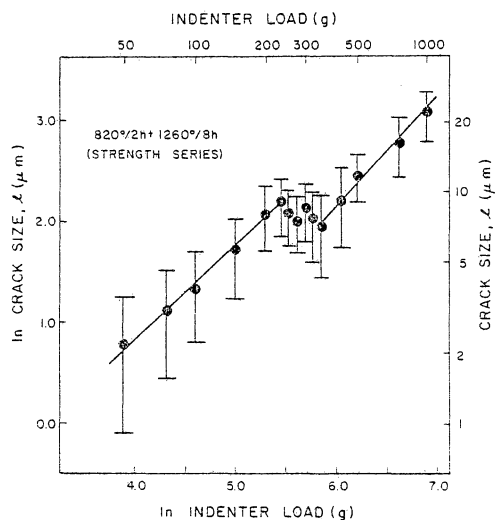


Fig. 11. Crack size as a function of indenter load for cordierite glass-ceramic given an initial heat-treatment of  $820^\circ\text{C}/2\text{h}$  followed by further treatment at: a,  $1100^\circ\text{C}/2\text{h}$ ; b,  $1100^\circ\text{C}/8\text{h}$ ; c,  $1150^\circ\text{C}/8\text{h}$ ; d,  $1150^\circ\text{C}/8\text{h}$  (strength series) - continued on next page. (Indicated error bars represent  $\pm 1$  estimated standard deviation from the mean.)



(e)



(f)

Fig. 11 (continued). Crack size as a function of indenter load for cordierite glass-ceramic given an initial heat-treatment for 820°C/2h followed by further treatment at: e, 1200°C/8h (strength series); and f, 1260°C/8h (strength series). (Indicated error bars represent  $\pm 1$  estimated standard deviation from the mean.)

graphs are in marked contrast to the completely continuous crack size-load curves which appear in Figure 9 for the original glass and the fine-precipitate glass-ceramic samples.

Examination of the crack size-load curve for a given heat treatment in Figure 11 indicates that the crack sizes at the higher loads lie below the extrapolation of the low load set of data into the high-load regime. This suggests that crack propagation is much more difficult at loads above, rather than below, the transition region as a result of the crack-crystallite interactions which occur in the high-load regime. Also note that the experimental scatter in crack size decreases with increasing load. As a consequence, crack sizes, when compared at the same load for the various heat treatments, are more likely to be significantly different above, rather than below, the transition region. This would be expected since, below the transition region, cracks are contained within the fine-grained matrix, and do not interact appreciably with any microstructural feature. Both the microscopy and X-ray diffraction analyses reported previously indicate that the fine-grained matrix remains essentially unaltered by heat-treatment. Above the transition region, crack propagation involves interaction with the dispersed phase. Since the quantitative microscopy results indicate that both volume fraction and mean free path of the dispersed phase vary with heat-treatment, it seems likely, then, that crack sizes above the transition region may be significantly altered by changes in the crystallization time/temperature schedule.

The results of linear regression analyses are listed in Table IX for the crack size-load curves which appear in Figure 11. The values of slope for the various curves (both below and above the transition region) agree reasonably well with the literature value of unity. The sole exception to this trend was a specimen from the thermal diffusivity study (86), which had been heat-treated at 1260°C for 8 hours. The slope value for this specimen in the high-load regime was approximately 0.6. However, this specimen had an extremely degraded and micro-cracked surface as a result of repeated polishings, with the result that crack sizes were very difficult to measure. A repeat heat-treatment (the specimen listed as "1260°C/8h, strength series") had a slope in the high-load regime of 1.04, which agrees quite well with the expected literature value. Since the data on the original 1260°C/8h sample could not be replicated, results from this specimen will not be reported.

A histogram of crack sizes, at three given loads is shown in Figure 12 for one of the heat-treatments (1150°C/8h). At any given load, the shape of the distribution of crack sizes depends, as seen in Figure 12, on whether the load selected lies within or outside the transition region. Of the three crack size histograms shown, a bimodal distribution of crack sizes is suggested for the transition region load (125g). A more uni-modal shape of the crack size distribution is obtained for loads below (50g) or above (1000g) the transition region.

TABLE IX. LINEAR REGRESSION ANALYSIS OF PALMQVIST CRACK SIZE AS A  
FUNCTION OF LOAD FOR CORDIERITE GLASS-CERAMIC FOR THE LARGE-CRYSTALLITE SAMPLES

$$\ln \ell = m \ln P + b$$

Heat-Treatment (Temp. and Time) *	Below Transition Region			Above Transition Region		
	Slope, m	Intercept, b	Correlation Coefficient	Slope, m	Intercept, b	Correlation Coefficient
1100°C/2h	0.981	-2.73	0.987	0.902	-2.68	1.00
1100°C/8h	0.992	-3.09	0.999	1.08	-3.92	0.999
1150°C/8h	1.13	-3.63	0.998	1.11	-4.37	0.990
1150°C/8h (Strength Series)	1.05	-3.25	0.974	0.864	-2.83	1.00
1200°C/8h (Strength Series)	0.957	-2.97	0.996	0.815	-2.44	0.998
1260°C/8h (Strength Series)	0.941	-2.96	0.997	1.04	-4.06	0.993

\* Following initial 820°C/2h nucleation treatment.

Above analyses for Palmqvist crack size,  $\ell$ , in microns, and indenter load, P, in grams;  
data for load range,  $50g \leq P \leq 1000g$ .

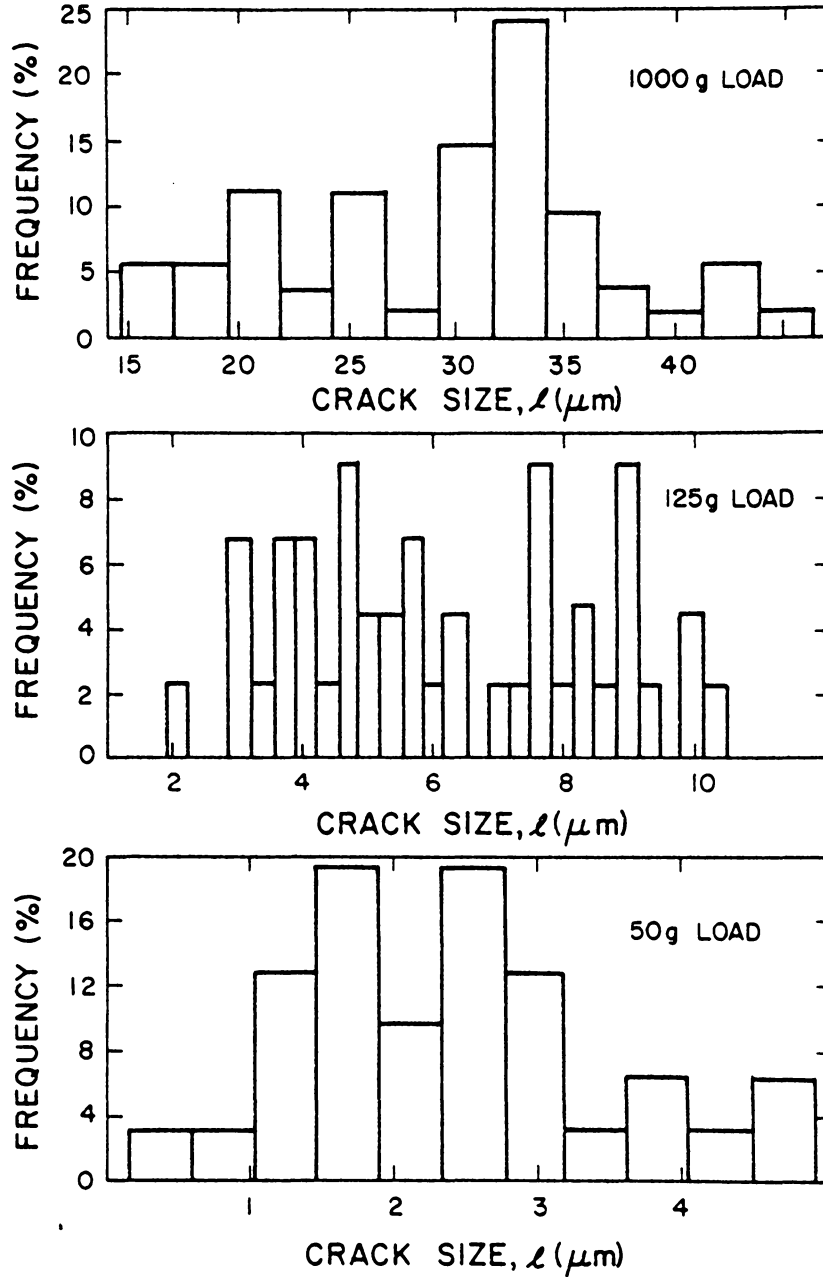
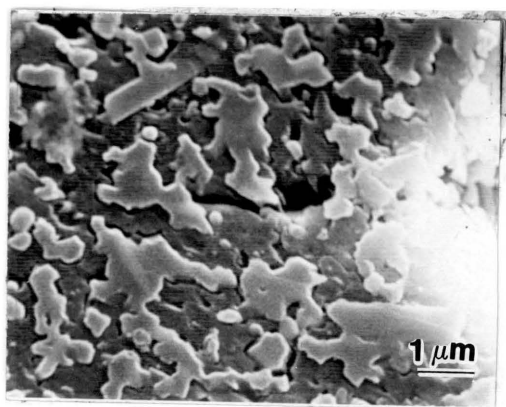


Fig. 12. Frequency histogram for crack size for cordierite glass-ceramic heat-treated at  $820^{\circ}\text{C}/2\text{h}$  plus  $1150^{\circ}\text{C}/8\text{h}$  for indenter loads of 50, 125, and 1000g. The 125g load for this sample corresponds to the start of the transition region.

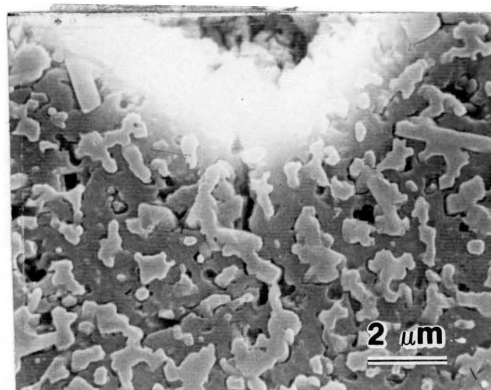
#### 4. Crack-crystallite interaction in the transition region

The transition region separates the low-load, or matrix, regime where crack processes are not appreciably affected by microstructure, from the high-load, or composite, regime where considerable microstructural involvement is evident with crack propagation. Photomicrographs of cracks introduced at loads corresponding to the transition region are shown in Figure 13 for specimens crystallized for 8 hours at 1100°C and 1200°C. In each instance, the crack has been stopped, or pinned, at a dispersed phase particle.

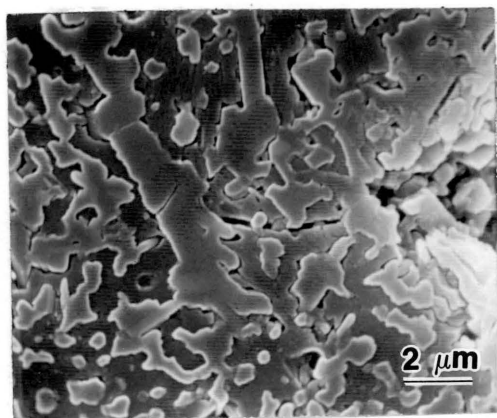
Evidence for this pinning interaction may be seen in Figure 14a where indent half-diagonal,  $a$ , and median crack size,  $c$ , are plotted on a ln-ln basis as a function of indenter load for a specimen crystallized at 1150°C for 8 hours. The half-diagonal dimension is completely continuous across the entire load range shown. A discontinuity is observed, however, for the median crack data, in which median crack size is relatively unchanged despite increasing indentation load. This discontinuity corresponds exactly to the load range over which the transition region is observed in the Palmqvist crack size curve in Figure 11c. The median crack dimension is the measure of the distance of the crack tip from the center of the indent. The horizontal region observed in median crack size in Figure 14a corresponds, then, to a load interval over which the position of the crack tip is relatively unchanged with respect to the center of the indent - i.e., a region where crack tip pinning by the dispersed crystallites occurs. It is this pinned position of the crack tip, combined with



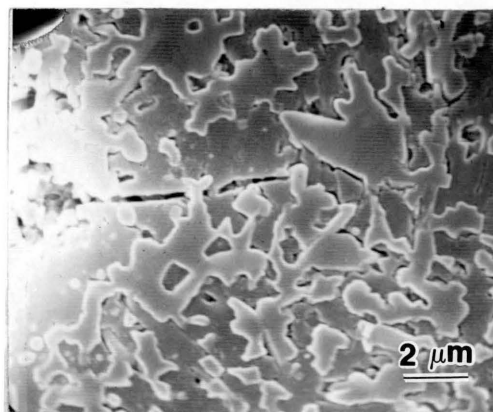
(a)



(b)

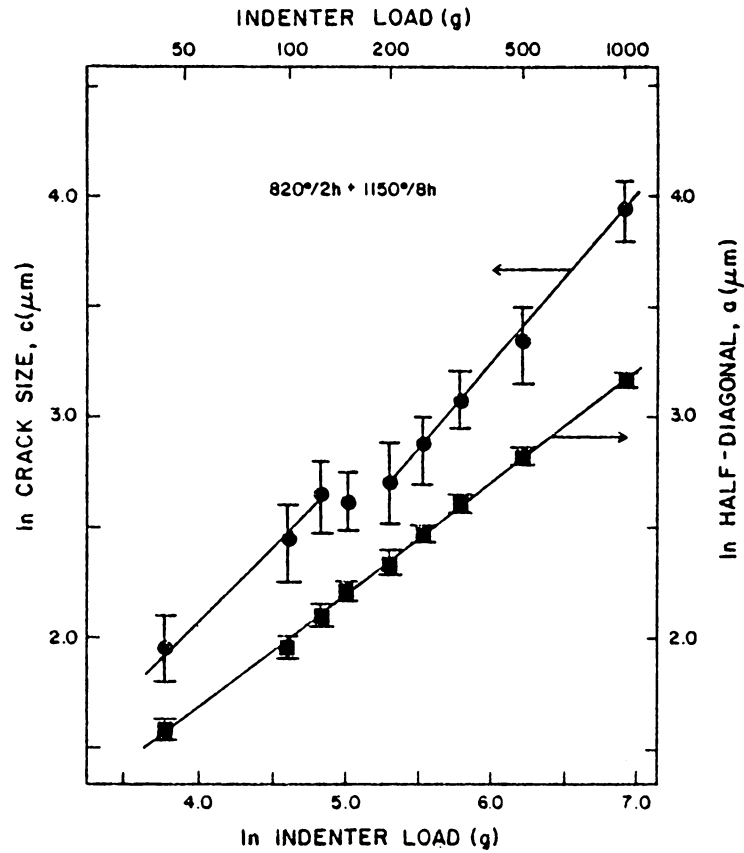


(c)

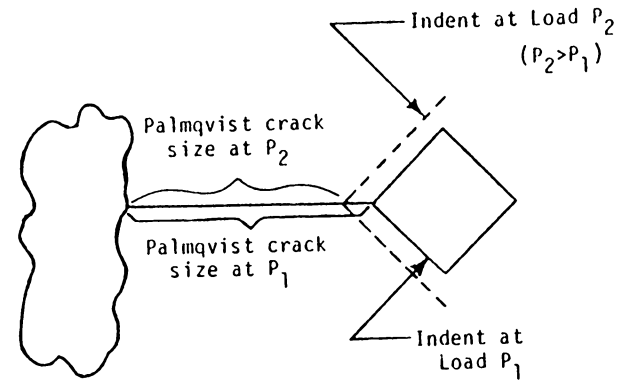


(d)

Fig. 13. SEM micrographs of crack-crystallite pinning in the transition region of cordierite glass-ceramic heat-treated at 820°C/2h followed by subsequent heat treatment at: a and b, 1100°C/8h; and c and d, 1200°C/8h.



(a)



(b)

Fig. 14. Explanation of decreasing Palmqvist crack size occurring with increasing indentation load in the transition region for the large-crystallite cordierite glass-ceramics: a, median crack size and half-diagonal length as functions of load for 820°C/2h plus 1150°C/8h sample (the error bars represent  $\pm 1$  standard deviation); and b, schematic showing effect of pinning on Palmqvist crack size,  $l$ .

the monotonic increase in indent size, that gives rise to the decrease in Palmqvist crack size (Fig. 14b) that occurs with increasing load across the transition region. This same phenomenon is seen for all the large-crystallite samples in Table X, where indentation parameters across the transition region are listed for the various heat-treatments.

The effect of microstructure on this pinning interaction is shown in Figure 15 where the average number of crystallites encountered prior to the start of crack pinning (calculated by dividing the Palmqvist crack size at the start of the transition region by the sum of the mean linear intercept length and the mean free path) is plotted as a function of average crystallite size (i.e., mean linear intercept length). As seen in this Figure, pinning of the surface crack tip occurs at a lower number of crystallite interactions as the particle size of the dispersed phase increases.

##### 5. Fracture toughness - standard test samples

To determine the suitability of the Palmqvist crack model for calculating fracture toughness ( $K_{Ic}$ ) by the indentation technique, as well as to test further the validity of the experimental procedures used in obtaining crack size data, indentation measurements were made on two materials that served as standards for  $K_{Ic}$  testing: soda-lime-silica glass, and the cordierite glass-ceramic that had been heat-treated by the manufacturer. The same sequence of polishing, annealing, etching, and indenting (in ambient air) operations described in the preceding Chapter was followed for these materials.

TABLE X. INDENTATION PARAMETERS ACROSS THE TRANSITION REGION  
FOR THE LARGE-CRYSTALLITE SAMPLES OF CORDIERITE GLASS-CERAMIC

Heat-Treatment (Temp. and Time)*	Lower Load Limit			Upper Load Limit		
	c ( $\mu\text{m}$ )	a ( $\mu\text{m}$ )	$\lambda$ ( $\mu\text{m}$ )	c ( $\mu\text{m}$ )	a ( $\mu\text{m}$ )	$\lambda$ ( $\mu\text{m}$ )
1100°C/2h	10.5	5.9	4.6	11.3	6.9	4.4
1100°C/8h	13.6	8.2	5.4	13.2	9.0	4.2
1150°C/8h	14.3	8.3	6.0	15.1	10.5	4.6
1150°C/8h (Strength Series)	12.6	7.6	5.0	12.4	8.6	3.8
1200°C/8h (Strength Series)	23.2	12.3	10.9	22.8	13.8	9.0
1260°C/8h (Strength Series)	20.8	11.9	8.9	21.8	14.8	7.0

\* Following 820°C/2h nucleation treatment

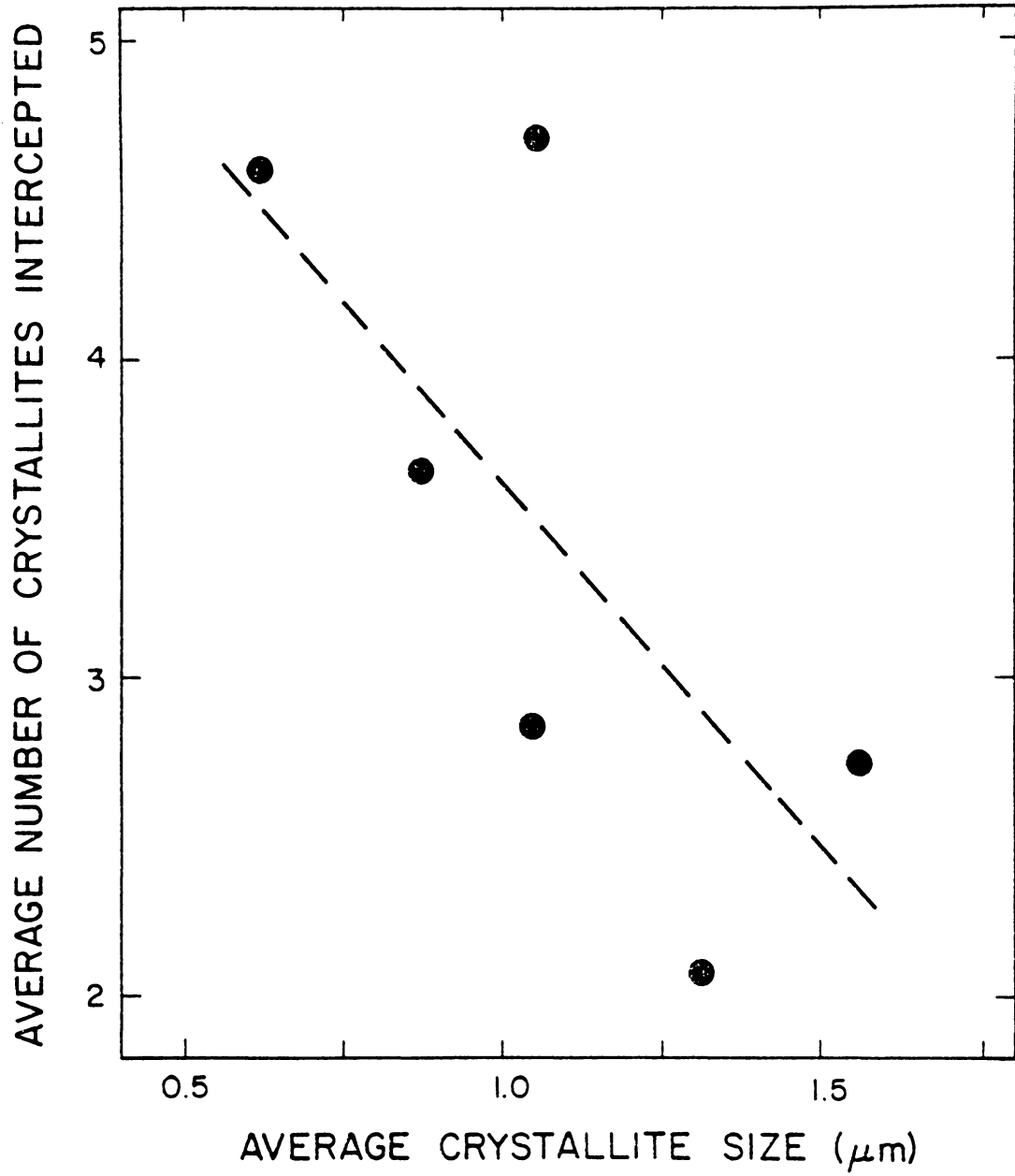


Fig. 15. Average number of crystallites intercepted before pinning commences as a function of crystallite size for cordierite glass-ceramic samples displaying a transition region.

Indentation data, as a function of load, are listed in Table XI for the soda-lime-silica glass. Two sets of toughness data are shown, depending on whether median crack (Eq. I-21a) or Palmqvist crack (Eq. I-21b) geometry was assumed. A Young's modulus value of  $73.4 \text{ GNm}^{-2}$  was used for the fracture toughness calculations (35). The accepted literature value (39) for the fracture toughness of soda-lime-silica glass is  $0.758 \pm 0.012 \text{ MNm}^{-3/2}$ , obtained by the double-cantilever beam (DCB) technique.

As seen in Table XI, fracture toughness values calculated assuming Palmqvist crack geometry give very good agreement with the DCB value for low  $c/a$  ratios, i.e., less than approximately 3.00. At higher  $c/a$  ratio, the median crack model gives the best agreement with the literature value. This complementary nature of these crack models has been discussed by Niihara et al. (71), who also found a region of  $c/a$  ratio in the approximate range 2.50-3.50 over which the two crack models yielded equivalent fracture toughness results. This effect may also be seen with the  $K_{Ic}$  values in Table XI.

Indentation measurements on the commercially heat-treated cordierite glass-ceramic were made at indenter loads of 700 and 900 grams, with 10 indents being measured at each load. The resulting  $c/a$  ratios were 1.74 and 1.83, respectively. A Young's modulus of  $132 \text{ GNm}^{-2}$  (see Table II) was assumed. Fracture toughness, calculated assuming Palmqvist crack geometry, was determined as  $2.23 \pm 0.38 \text{ MNm}^{-3/2}$  at 700 grams, and  $2.25 \pm 0.26 \text{ MNm}^{-3/2}$  at 900 grams. These results were pooled to give an overall value of  $2.24 \pm 0.33 \text{ MNm}^{-3/2}$ .

TABLE XI. INDENTATION PARAMETERS AND FRACTURE TOUGHNESS VALUES  
FOR SODA-LIME-SILICA GLASS

	Indentation Load (g.)					
	<u>25</u>	<u>50</u>	<u>100</u>	<u>200</u>	<u>500</u>	<u>1000</u>
Median crack size, c(μm)	7.11±0.41 (38)	12.1±0.62 (39)	19.6±1.29 (38)	35.3±2.22 (35)	70.3±4.61 (32)	11.2±5.72 (36)
Indent half-diagonal, a(μm)	4.31±0.19 (20)	6.41±0.12 (20)	9.10±0.18 (20)	12.9±0.31 (20)	20.6±0.39 (20)	29.8±0.50 (20)
c/a ratio	1.65	1.89	2.15	2.74	3.41	3.76
Fracture toughness, $K_{IC}$ (MNm <sup>-3/2</sup> )						
Palmqvist crack model (Eq. I-21b)	0.77±0.06	0.76±0.04	0.79±0.05	0.76±0.04	0.81±0.04	0.88±0.03
median crack model (Eq. I-21a)	1.09±0.09	1.02±0.08	0.99±0.10	0.82±0.08	0.75±0.08	0.76±0.06

Note:

- (1) Number of data points for measured values are indicated in parentheses.
- (2) Uncertainty shown indicates ± 1 standard deviation.
- (3) Mean  $K_{IC}$  value calculated from mean c and a values.
- (4) Standard deviation for  $K_{IC}$  estimated from standard error in measured crack sizes.

The samples of the commercially heat-treated glass-ceramic on which the above data were determined were part of a round-robin study (107) conducted by ASTM Subcommittee E24-07 aimed at comparing  $K_{Ic}$  values obtained by a variety of experimental methods. Both indentation and non-indentation test methods were included in the study. The round-robin results from the participating laboratories are listed in Table XII.

Note the close agreement between the fracture toughness values calculated by the Palmqvist indentation method and those obtained by non-indentation methods, namely, the double-torsion and short rod tests. Further support for the value of 2.24 determined by the Palmqvist method may be had with data reported by Lewis (108) for a different lot of the commercially heat-treated cordierite glass-ceramic. Lewis lists a value of  $2.14 \text{ MNm}^{-3/2}$  based on 14 data points using the double-cantilever beam technique.

The data from both the soda-lime-silica glass and the commercially heat treated cordierite glass-ceramic indicate that the Palmqvist crack model in conjunction with the experimental procedure described in the preceding Chapter may be used with confidence to obtain reliable fracture toughness values. The versatility of the indentation technique may be extended by using a median crack model at high  $c/a$  ratios.

#### 6. Fracture toughness of the cordierite glass-ceramic

Fracture toughness data, based on the Palmqvist crack sizes listed in Tables VI and VIII, and calculated using Eq. I-21b, are presented

TABLE XII. COMPARISON OF FRACTURE TOUGHNESS ROUND-ROBIN RESULTS  
ON COMMERCIALY HEAT-TREATED CORDIERITE GLASS-CERAMIC

<u>Technique</u>	<u>Fracture Toughness, MNm<sup>-3/2</sup></u>
Controlled Indentation Microflaw (2 Laboratories)	1.62 ± 0.05 1.68 ± 0.08
Indentation (median crack model)	2.76 ± 0.34
Indentation (Palmqvist crack model)	2.24 ± 0.33
Double Torsion (2 Laboratories)	2.15 2.15
Short-Rod	2.13 ± 0.06

in Table XIII for the original glass and the heat-treated glass-ceramic samples. Given the range shown in average  $c/a$  ratios, the Palmqvist crack model would appear the more appropriate of the 2 crack geometries for  $K_{Ic}$  calculations. The values of Young's modulus used in these calculations were those given in Table II. The overall fracture toughness value listed in Table XIII for each sample or load regime represents the grand average of the individual mean  $K_{Ic}$  values determined at each of the loads investigated. The standard deviation listed for each overall toughness value represents the pooled value calculated from the variances in toughness estimated at each load from the scatter in the measured crack size data. As indicated by the range in the individual mean toughness values, the between group variation in overall fracture toughness for each sample or load regime is relatively small. The relatively large value in the calculated uncertainty shown for each overall toughness value reflects the large within group variation caused by both experimental error inherent in measuring small values of crack size, as well as by statistical variation occurring in the microstructure.

The toughness value of  $1.22 \text{ MNm}^{-3/2}$  obtained for the original glass is rather high compared to other silicate glasses which have typical toughness values in the range  $0.70\text{--}0.90 \text{ MNm}^{-3/2}$  (39). However as noted in the initial Section of this Chapter which dealt with microstructure, a slight opalescence was noted in the original glass. This opalescence, on the basis of reported literature studies (88,89), may be attributed to glass-in-glass phase separation. Toughness values of  $1.10\text{--}1.20 \text{ MNm}^{-3/2}$  have been reported by Brinker and Mecholsky (109) for several

TABLE XIII. FRACTURE TOUGHNESS VALUES FOR CORDIERITE GLASS-CERAMIC

A. Original Glass and Fine-Precipitate Samples

Heat-Treatment (Temp. and Time)	Load Range (g.)	No. of Loads	Fracture Toughness, $K_{Ic}$ ( $MNm^{-3/2}$ )		Overall $K_{Ic}$ (all loads)
			Range in Average $c/a$ Ratio	Range in Average $K_{Ic}$ for Individual Loads	
Original Glass	50-1000	5	1.60-3.35	1.20-1.25	$1.22 \pm 0.14$
820°C/2h	50-1000	5	1.67-3.33	1.15-1.26	$1.19 \pm 0.12$
820°C/2h+905°C/8h	50-1000	5	1.58-2.87	1.30-1.45	$1.37 \pm 0.16$
820°C/2h+1000°C/8h	50-1000	5	1.71-3.43	1.39-1.48	$1.44 \pm 0.15$
820°C/2h+1000°C/8h (strength series)	50-1000	7	1.71-3.31	1.28-1.43	$1.38 \pm 0.17$
820°C/2h+1100°C/1h	50-1000	5	1.56-3.17	1.61-1.64	$1.63 \pm 0.32$

(continued on next page)

TABLE XIII. (Cont'd) FRACTURE TOUGHNESS VALUES FOR CORDIERITE GLASS-CERAMICS

## B. Large Crystallite Samples

Heat-Treatment* (Temp. and Time)	FRACTURE TOUGHNESS, $K_{Ic}$ (MNm <sup>-3/2</sup> )									
	Low-Load Regime					High Load Regime				
	Load Range(g)	No. of Loads	Range in Average c/a Ratio	Range in Average $K_{Ic}$ of Individual Loads	Overall $K_{Ic}$ (all loads)	Load Range(g)	No. of Loads	Range in Average c/a Ratio	Range in Average $K_{Ic}$ of Individual Loads	Overall $K_{Ic}$ (all loads)
1100°C/2h	50-75	3	1.67-1.78	1.38-1.41	1.39±0.30	100-1000	4	1.64-2.50	1.61-1.79	1.71±0.25
1100°C/8h	50-125	3	1.45-1.66	1.58-1.60	1.59±0.40	150-1000	5	1.47-2.34	1.83-2.00	1.90±0.40
1150°C/8h	50-125	3	1.45-1.72	1.53-1.62	1.57±0.47	200-1000	5	1.44-2.15	2.01-2.22	2.18±0.54
1150°C/8h (strength series)	50-100	3	1.45-1.66	1.49-1.52	1.52±0.42	125-1000	4	1.44-1.91	1.93-2.22	2.06±0.45
1200°C/2h (strength series)	50-250	4	1.40-1.88	1.59-1.70	1.62±0.58	300-1000	7	1.65-1.98	1.89-2.13	1.99±0.25
1260°C/8h (strength series)	50-225	6	1.39-1.75	1.63-1.72	1.67±0.44	350-1000	5	1.47-1.83	2.14-2.33	2.22±0.37

\* Following initial 820°C/2h nucleation treatment.

Uncertainty range for overall  $K_{Ic}$  is ± 1 standard deviation (see text).

phase-separated alkali/alkaline earth silicate glasses. Lending support for the presence of phase separation in accounting for the high toughness value of the original glass is the  $K_{IC}$  value for the 820°C/2h heat-treatment. This latter sample, which received only the nucleation heat-treatment, has a fracture toughness value essentially identical to that of the original glass.

With the onset of crystallization (i.e., the 905°C/8h heat-treatment), toughness increases slightly, from the value of approximately  $1.20 \text{ MNm}^{-3/2}$  obtained on the glass, to  $1.37 \text{ MNm}^{-3/2}$ . The overall toughness value for the fine-precipitate samples do not vary appreciably with heat-treatment temperature, and are all within the range 1.37 to  $1.63 \text{ MNm}^{-3/2}$ . These values are quite similar to the toughness values obtained in the low-load regime for the large-crystallite samples, where overall toughness ranged from 1.39 to  $1.67 \text{ MNm}^{-3/2}$ , depending on heat treatment. On the basis of this correspondence in toughness, both the large-crystallite samples in the low-load regime and the fine-precipitate samples behave in a similar manner with respect to crack propagation, namely, propagation of cracks occurs within a fine-grained phase without any appreciable interaction occurring with the microstructure.

Toughness values in the high-load regime for the large-crystallite samples range from 1.71 to  $2.22 \text{ MNm}^{-3/2}$ , depending on heat treatment. This variation is appreciably greater than the variation in  $K_{IC}$  which occurs with heat-treatment in the low load regime, and illustrates the effect that microstructural variables have on crack-crystallite interaction in the high-load regime. Microstructural and toughness data

are summarized in Table XIV for all the large crystallite heat-treatments. Also listed for each heat-treatment is the value of effective fracture surface energy,  $\gamma_{\text{eff}}$ , for the composite regime calculated from Eq. I-6 by using the Young's modulus values reported in Table II.

The data in Table XIV indicate that fracture toughness and effective fracture surface energy in the composite regime are affected by changes in volume fraction,  $V_f$ , mean free path,  $\lambda$ , and average crystallite size,  $\bar{L}$ , of the dispersed phase, as well as by variation in the ratio  $\bar{L}/\lambda$ . Fracture toughness and  $\gamma_{\text{eff}}$  increase with increases in either  $\lambda$  or  $\bar{L}$ , and with decreases in either  $V_f$  or  $\bar{L}/\lambda$ . Fracture toughness as a function of mean free path and average crystallite size is shown in Figures 16, a and b, respectively. In each instance, the data can be fitted to a linear relationship with the following best-fit expressions obtained from linear regression analysis:

$$K_{\text{Ic}} = 0.49 \bar{L} + 1.48 \quad (\text{correl. coef.} = 0.86) \quad (\text{III-1})$$

$$K_{\text{Ic}} = 0.36 \lambda + 1.65 \quad (\text{correl. coef.} = 0.88) \quad (\text{III-2})$$

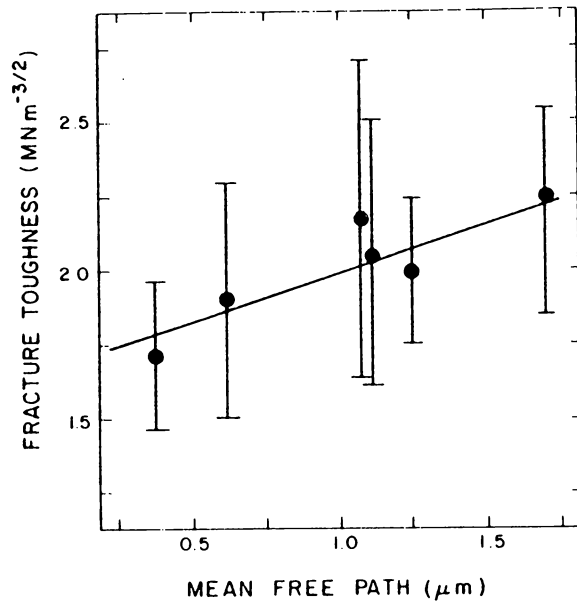
The microstructural dependence of the high-load regime  $K_{\text{Ic}}$ , seen in Eqs. III, 1 and 2, explains the increases occurring in fracture toughness with increasing crystallization temperature for the large-crystallite samples. As shown in Table XIV, both  $\bar{L}$  and  $\lambda$  increase with higher heat-treatments. This microstructural dependence also accounts for the fracture toughness value of the 1200°C sample, which was lower than either of the two 1150°C heat-treatments. As seen from Table XIV, the average crystallite size of the 1200°C/8h sample was less than that of either 1150°C heat-treatment.

TABLE XIV. TOUGHNESS AND MICROSTRUCTURE DATA FOR THE LARGE-CRYSTALLITE SAMPLES OF THE CORDIERITE GLASS-CERAMIC

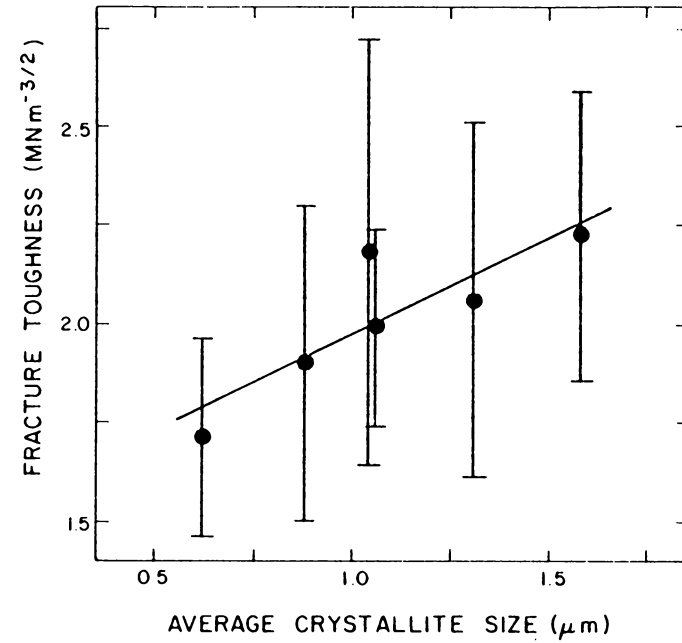
Heat-Treatment (Temp. and Time) *	Microstructural Parameter				Av. Fracture Toughness, $K_{Ic} (MNm^{-3/2})$		Fracture Surface Energy For Composite Regime, $\gamma_{eff} (Jm^{-2})$
	Volume Fraction of Dispersed Phase, $V_f$	Mean Intercept Length, $\bar{L} (\mu m)$	Mean Free Path, $\lambda (\mu m)$	$\bar{L}/\lambda$	Matrix	Composite	
1100°C/2h	0.622	0.620	0.380	1.63	1.39	1.71	11.72
1100°C/8h	0.585	0.871	0.610	1.43	1.59	1.90	14.47
1150°C/8h	0.492	1.04	1.07	0.972	1.57	2.18	19.20
1150°C/8h **	0.535	1.31	1.11	1.18	1.52	2.06	16.26
1200°C/8h **	0.455	1.05	1.26	0.833	1.62	1.99	16.12
1260°C/8h **	0.480	1.56	1.68	0.929	1.67	2.22	20.06

\*Following nucleation treatment of 820°C for 2h.

\*\*Strength series.



(a)



(b)

Fig. 16. Fracture toughness in the high-load regime for the large-crystallite samples of the cordierite glass-ceramic as a function of: a, mean free path; and b, average crystallite size for the dispersed phase. (Indicated error bars represent  $\pm 1$  standard deviation from the mean.)

Overall fracture toughness values, plotted as a function of load range, are shown in Figure 17 for the original glass and for those heat-treatments which involved crystallization heat-treatment times of 8 hours. Unlike the  $K_{Ic}$  values for the original glass and the fine-precipitate samples, the fracture toughness values of the large-crystallite samples are seen to increase with increasing load from below to above the transition region. The increase in toughness that occurs for these samples indicates, essentially, the existence of a crack size-dependent fracture toughness. This toughness increase across the transition region takes place in a smooth, continuous manner as seen in Figure 18, where average fracture toughness is plotted as a function of load for a specimen crystallized at 1260°C for 8 hours.

## 7. Strength behavior

Strength values following indentation are shown in Table XV as a function of indentation load for the original glass and for samples crystallized for 8 hours at 1000°C, 1150°C, 1200°C, and 1260°C. Microscopy and crack length measurements reported earlier in this Chapter for specimens obtained from these same sets of strength samples indicate that the 1150°C, 1200°C, and 1260°C heat-treatments all possess the large-crystallite microstructure and exhibit a transition region with attendant crack-pinning. No

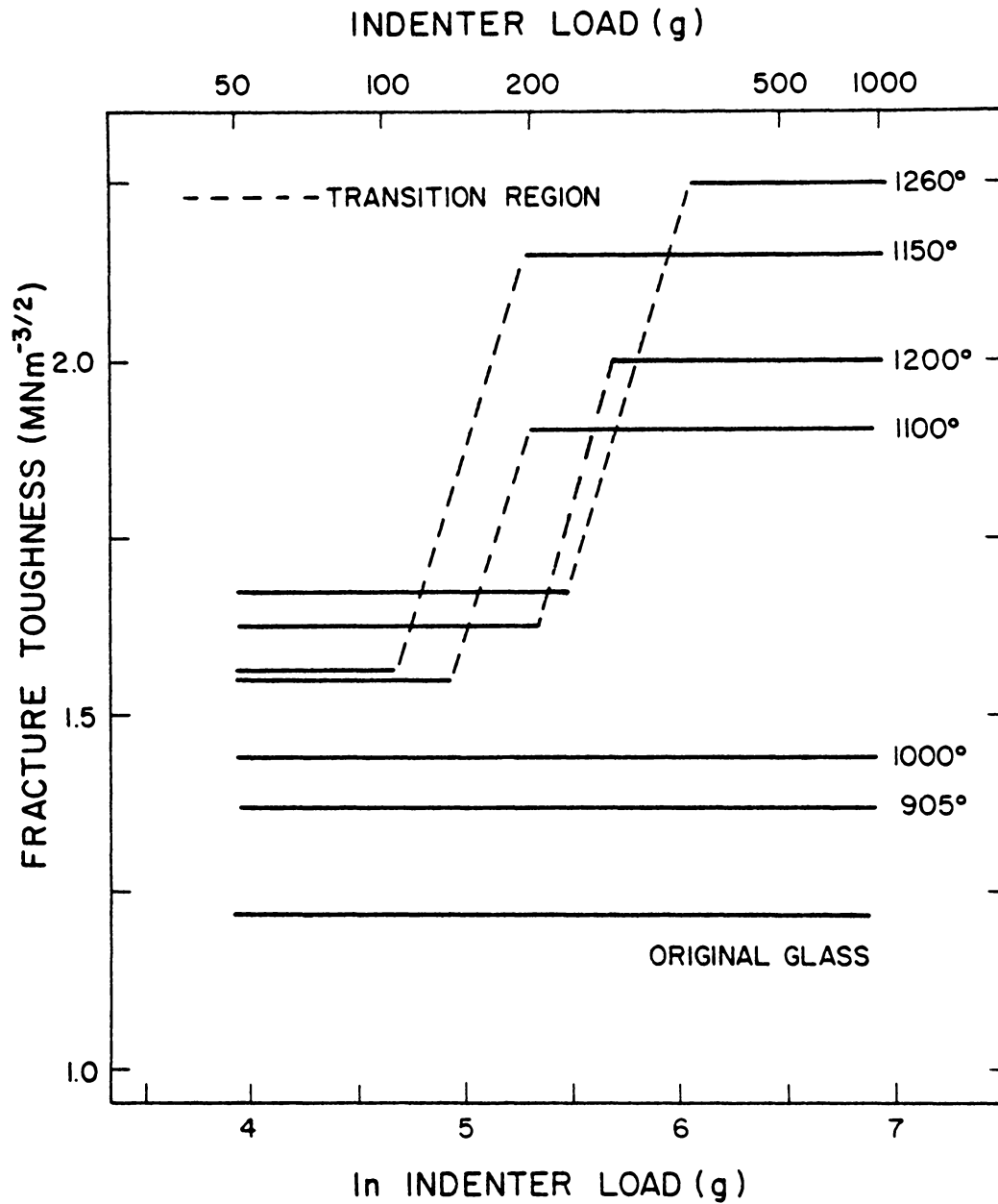


Fig. 17. Fracture toughness of cordierite glass-ceramic for original glass and samples heat-treated for 3h at indicated temperatures following initial heat-treatment at 820°C/2h.

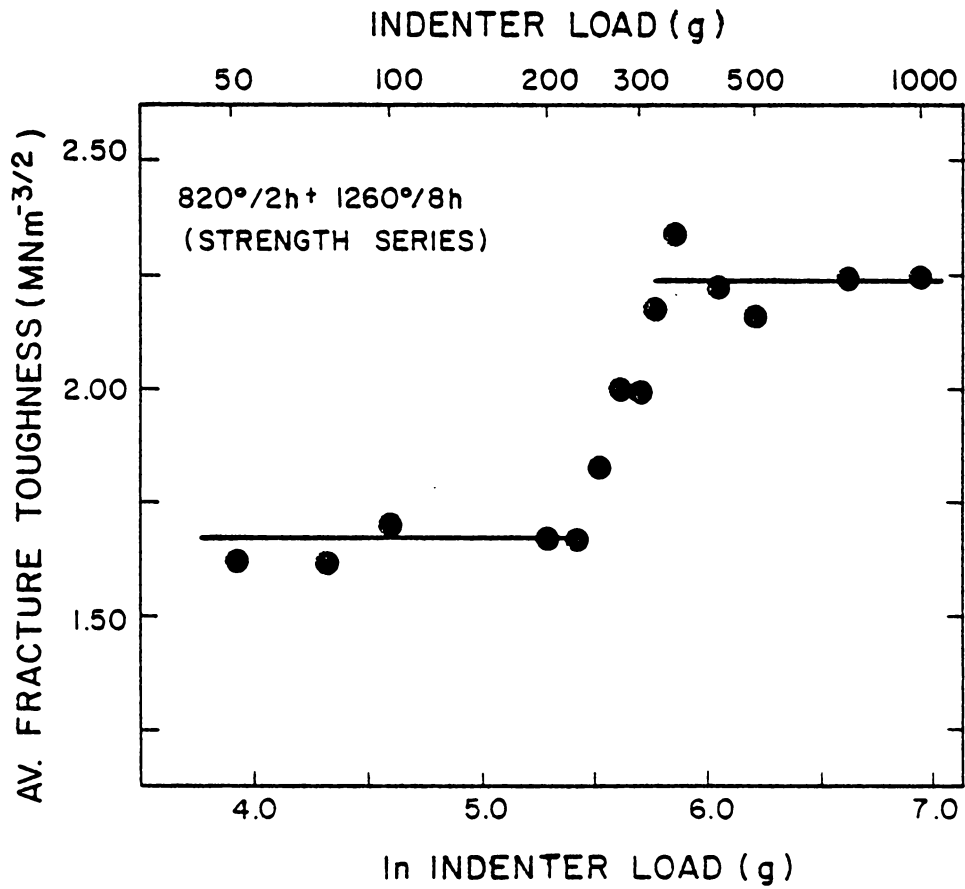


Fig. 18. Average fracture toughness as a function of indenter load for cordierite glass-ceramic heat-treated at 820°C/2h plus 1260°C/8h.

TABLE XV. STRENGTH VALUES AS FUNCTION OF INDENTATION LOAD FOR ORIGINAL CLASS AND CRYSTALLIZED SAMPLES OF CORDIERITE GLASS-CERAMIC

Heat-Treatment (Temp. and Time)	Trans. Region(g)	FRACTURE STRENGTH (MPa) FOLLOWING INDICATED INDENTATION LOAD (g.)																
		Un- Indented	50	75	100	125	150	200	225	250	275	300	325	350	500	650	750	1000
Original Class	-	210.9± 44.7	188.6± 40.8		161.9± 27.8			150.0± 25.0							125.0± 11.4			97.0± 18.0
820°C/2h+1000°C/8h	-	349.5± 80.5	272.2± 35.2		239.3± 40.6			206.2± 26.8						162.0± 18.3	138.9± 18.3		117.7± 15.6	108.2± 10.1
820°C/2h+1150°C/8h	100-125	311.9± 33.2	268.5± 32.9	258.5± 35.3	246.5± 35.2	266.0± 34.1	267.9± 30.7	230.1± 35.4							197.5± 26.5			168.9± 23.8
820°C/2h+1200°C/8h	250-300	249.6± 26.3	228.0± 17.7				221.9± 20.4			223.6± 20.1	226.0± 19.7	251.3± 31.4				202.7± 32.1	198.4± 34.8	180.5± 29.7
820°C/2h+1260°C/8h	225-350	288.5± 19.9	264.2± 23.3				260.2± 15.1		253.9± 11.8	254.9± 19.3		252.7± 20.4	254.9± 29.1	249.2± 29.1	241.5± 20.1		217.4± 24.0	201.2± 27.1

Numbers shown are mean ± 1 standard deviation; each mean represents average of 8-10 individual values.

transition region was found for the 1000°C strength set with specimens from this heat-treatment all having the uniform and very fine-scale crystallite dispersion characteristic of the **fine-precipitate** microstructure.

The strength data reported in Table XV are plotted as a function of load in Figures 19, a-d. The line through each set of data was obtained by a linear regression analysis. The linear regression parameters are listed in Table XVI.

At low loads the strength values for the large-crystallite samples are seen to be relatively-unaffected by changes in indentation load. Only at higher loads does strength for these samples decrease with increasing indentation load. In contrast to this, the strength values for the original glass and the 1000°C/8h sample show a decrease with increasing indentation load over the whole range of loads investigated. It may be seen that the strength data in the decreasing strength region for the large-crystallite samples can be fitted to a single linear regression curve. However, for the original glass and the 1000°C/8h heat-treatment, a better fit to the strength data is obtained with two regression lines.

Also shown in each graph in Figure 19 for the large-crystallite samples is the location of the transition region, based on the crack size measurements reported earlier. In each case, the upper value of load at which the constant strength region ends essentially coincides with the high load end of the transition region. It is also noteworthy that this constant strength region occurs over a load range where crack size (and thus the extent of surface damage) was found

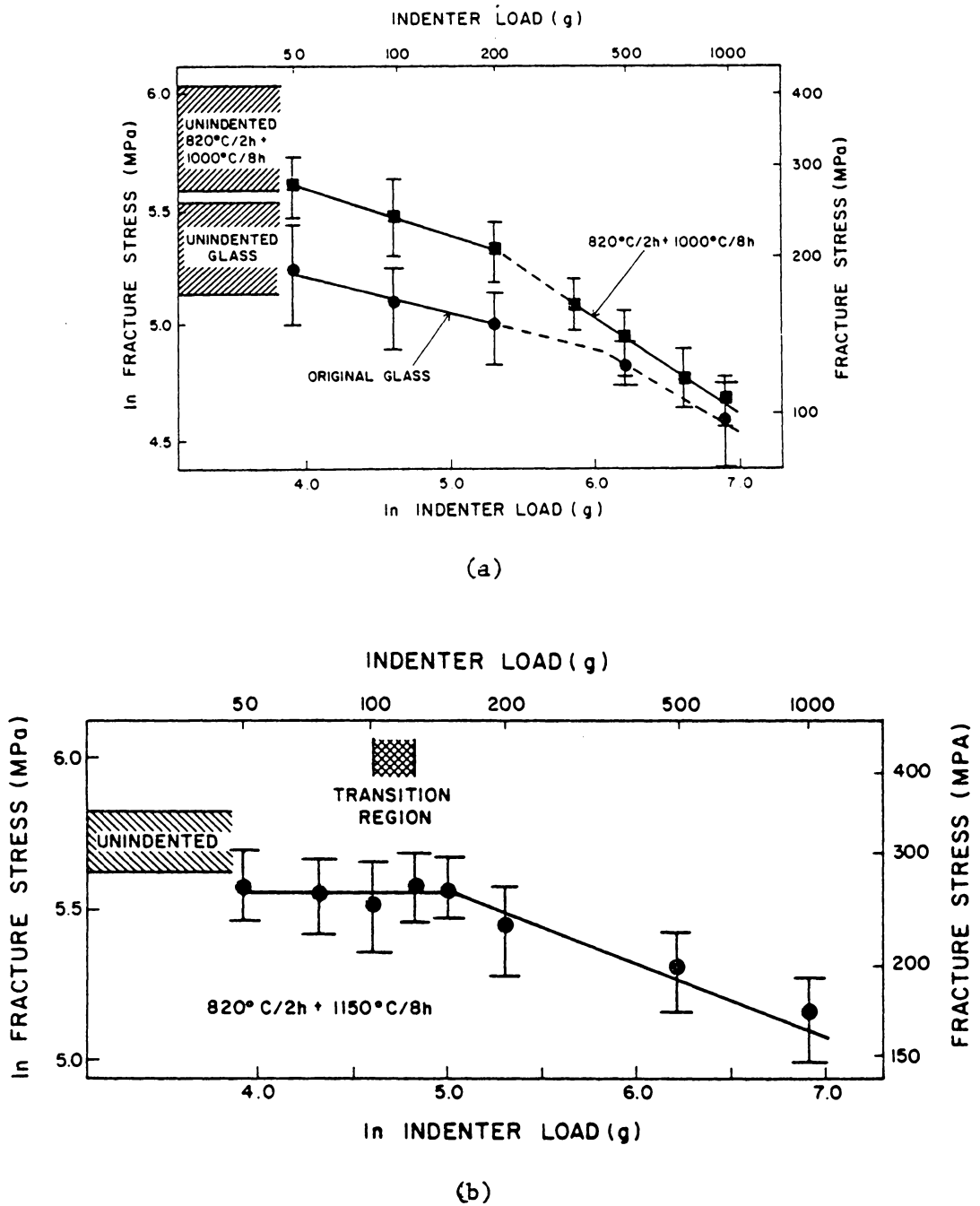
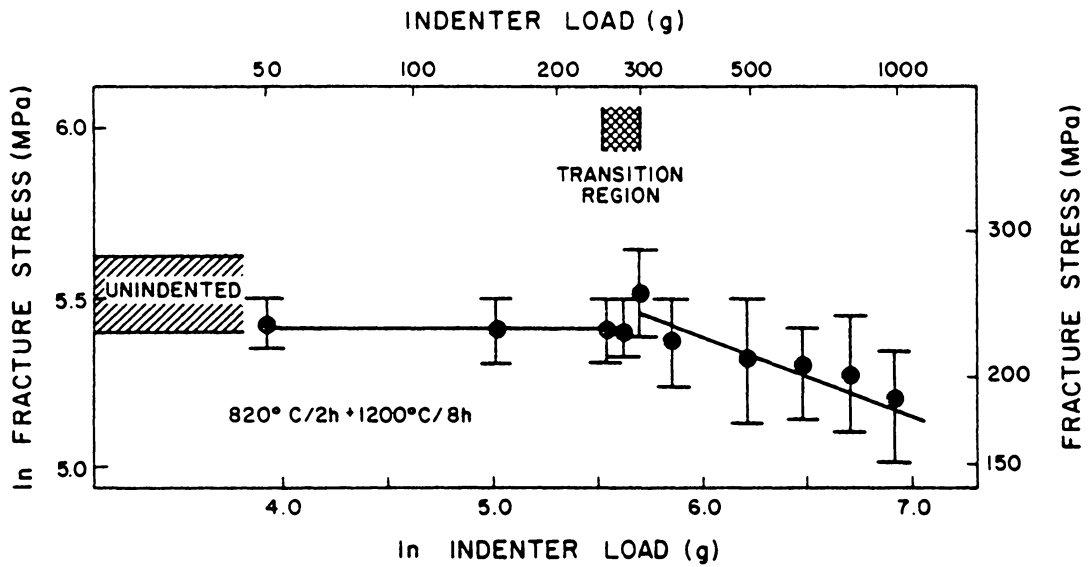
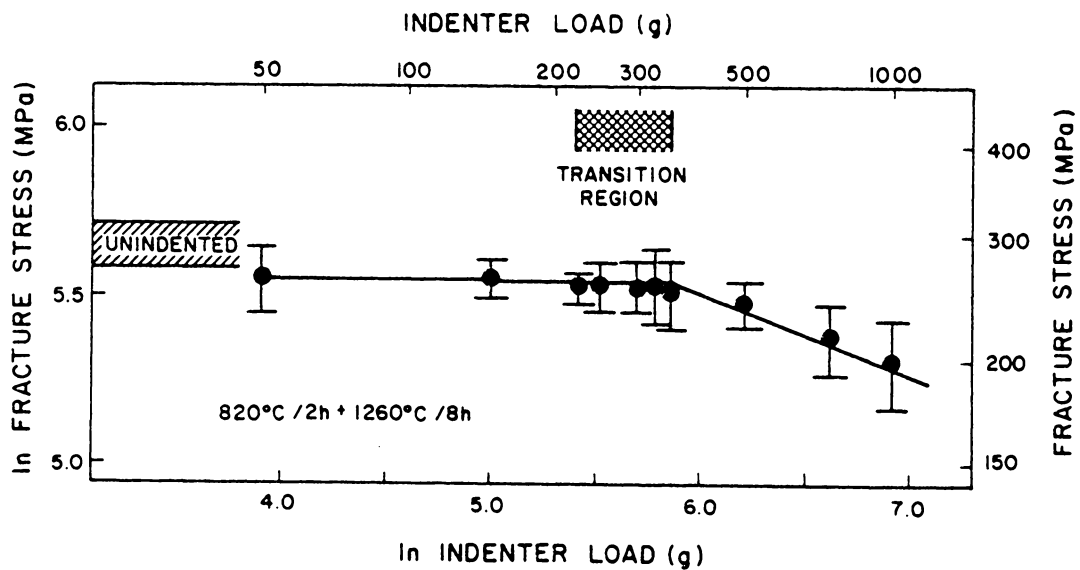


Fig. 19. Fracture stress as a function of indenter load for the cordierite glass-ceramic for: a, original glass; and samples heat-treated at 820°C/2h followed by 8 hour growth treatment at: a, 1000°C; b, 1150°C/8h (continued on next page). (Indicated error bars represent  $\pm 1$  standard deviation from the mean.)



(c)



(d)

Fig. 19 (continued). Fracture stress as a function of indenter load for the cordierite glass-ceramic for samples heat-treated at 820°C/2h followed by 8 hour growth treatment at: c, 1200°C; and d, 1260°C. (Indicated error bars represent  $\pm 1$  standard deviation from the mean.)

TABLE XVI. LINEAR REGRESSION ANALYSIS OF STRENGTH-LOAD BEHAVIOR FOR ORIGINAL GLASS AND CRYSTALLIZED SAMPLES OF CORDIERITE GLASS-CERAMIC

Heat-Treatment (Temp. and Time)	Load Range(g)	No. of Loads	c/a Range	$\ln \sigma_f = m \ln P + b$		
				Slope, m	Intercept, b	Correlation Coefficient
Original Glass	50-200	3	1.6-2.2	-0.165	5.87	-0.982
	500-1000	2	2.8-3.4	-0.366	7.10	-1.00
820°C/2h + 1000°C/8h	50-200	3	1.7-2.2	-0.200	6.39	-0.995
	350-1000	4	2.9-3.3	-0.389	7.36	-0.997
820°C/2h + 1150°C/8h	150-1000*	4	1.6-1.9	-0.225	6.68	-0.983
820°C/2h + 1200°C/8h	300-1000*	4	1.7-1.9	-0.222	6.73	-0.924
820°C/2h + 1260°C/8h	350-1000*	4	1.5-1.8	-0.209	6.78	-0.980

Above analyses for fracture strength,  $\sigma_f$ , in MPa, and indenter load, P, in g.

\*The load range shown corresponds to the decreasing strength region for these samples.

to increase with increasing load. For one of the strength sets (the 1200°C heat-treatment shown in Fig. 19c), an actual increase in strength (from 226 to 251 MPa) was observed at the end of the transition region. This increase is significant at the 95% Confidence Level.

To determine the effect that any residual stress from the indentation may have on strength values, a comparison was made using 2 sets of 10 strength specimens each, selected at random from a lot of 820°C/2h + 1260°C/10h samples. Prior to subdividing the specimens into the 2 sets, each specimen was given the standard strength preparation treatment consisting of polishing, annealing, and etching. This was followed by indenting each specimen with a 300 gram load. Following the indentation, the specimens were subdivided randomly into the two treatment groups. One of the groups received a post-indentation anneal (700°C for 3h) designed to relieve any residual stresses which may be present from the indentation. The second group, as was done for all the strength tests reported in Table XV, did not receive any post-indentation anneal. The strength results (mean  $\pm$  1 standard deviation) were as follows:

No post-indentation anneal	249,4 $\pm$ 34,3 MPa
Post-indentation anneal	244,8 $\pm$ 30,1 MPa

These results were deemed to not be significantly different at the 90% Confidence Level.

#### 8. Vicker's hardness: Effect of heat-treatment

Vicker's hardness values at an indentation load of 1000 grams are listed in Table XVII for all samples. Heat-treatment of the original

TABLE XVII. VICKER'S HARDNESS VALUE AT 1000 GRAMS  
FOR CORDIERITE GLASS-CERAMIC

<u>Heat-Treatment (Temp. and Time)</u>	<u>Vicker's Hardness Value at 1000g (GNm<sup>-2</sup>)</u>
Original Glass	7.07 ± 0.25 (22)
820°C/2h	7.17 ± 0.23 (24)
820°C/2h + 905°C/8h	8.10 ± 0.32 (24)
820°C/2h + 1000°C/8h	9.84 ± 0.45 (24)
820°C/2h + 1000°C/8h (strength series)	8.54 ± 0.31 (20)
820°C/2h + 1100°C/1h	10.62 ± 0.50 (24)
820°C/2h + 1100°C/2h	8.60 ± 0.22 (24)
820°C/2h + 1100°C/8h	7.77 ± 0.20 (24)
820°C/2h + 1150°C/8h	7.90 ± 0.28 (24)
820°C/2h + 1150°C/8h (strength series)	7.58 ± 0.26 (24)
820°C/2h + 1200°C/8h (strength series)	7.07 ± 0.34 (20)
820°C/2h + 1260°C/8h (strength series)	6.73 ± 0.30 (20)

Values shown are mean ± 1 standard deviation (standard deviation estimated from range in measured indent size).

Number of data points indicated in parenthesis.

glass produces a rapid increase in hardness with increasing heat-treatment temperature for the fine-precipitate samples. Hardness reaches a maximum value at the start of the stuffed quartz  $\rightarrow$   $\alpha$ -cordierite transformation (1100°C/1h), and then decreases with increasing heat-treatment temperature for the large-crystallite samples. The hardness of the 1260°C/8h sample is actually lower than that of the original glass. A hardness - heat-treatment relationship identical to this was observed at all indentation loads investigated.

#### IV. DISCUSSION

##### A. Cracking Pinning

The measurements of crack size as a function of indentation load confirm the basic concept of the dispersion-strengthening model of Hasselman and Fulrath (47) that the dispersed phase (assuming its fracture toughness exceeds that of the matrix) in a brittle composite acts as a geometric constraint to the introduction of flaws. This model for the role played by the dispersed phase in the cordierite glass-ceramic is most appropriate in describing crack-crystallite interaction at the low-load end of the transition region. SEM observations made of the flaw-introduction process for the large-crystallite samples show that with increasing indentation load in the low-load or matrix-controlled regime, the size of flaws introduced in the matrix will increase until a second phase particle is encountered by the crack. At this point, the crack is pinned by the particle. Despite increasing indentation load, continued propagation of the crack ceases until the value of the stress intensity factor generated from the contact event becomes sufficiently large to overcome the resistance to crack extension created by the presence of the particle. Once the crack finally does break free, so that the high load, or composite-controlled, regime begins, the dominant form of crack-crystallite interaction is no longer pinning, but rather crack deflection.

The crack pinning interaction that marks the start of the transition region is complicated by the shallow, semi-elliptical configuration of the Palmqvist cracks (Fig. 3b). Because of this crack geometry, a

greater degree of crack-crystallite interaction will be evident along the crack surface than along the sub-surface crack front perimeter. This is illustrated in the SEM micrographs which appeared in Fig. 13, where crack pinning is observed to occur only after the crack has encountered several crystallites, rather than a single crystallite as would be anticipated from the Hasselman-Fulrath model. However, this is entirely reconcilable with the dispersion-strengthening hypothesis, since what is depicted in Fig. 13 is behavior relating to the surface crack tip and not to the crack front as a whole. Until the entire sub-surface portion of crack front has become pinned it will be capable of dragging the surface crack tip past any potential pinning interactions. Although pinning of the crack front may well occur at the first encounter with a crystallite, the low aspect ratio of the Palmqvist crack will assure that the surface crack tip will not become pinned until several interactions take place between it and the dispersed particles. This behavior accounts for the decrease, which occurs with increasing crystallite size, in the number of crack-crystallite encounters required before pinning commences (see Fig. 15), since large particle sizes make it more difficult for the subsurface crack front to drag the surface crack tip past crystallites.

The crack size data which were shown in Fig. 11 for those samples having the wider transition regions (i.e., the 1150°C, 1200°C, and 1260°C heat-treatments) suggest that the decrease in crack size found to occur in the transition region proceeds in a smooth, monotonic

fashion rather than as an abrupt, discontinuous process. It would be expected, however, that within the transition region, crack size influenced as it is by crack-crystallite interactions, would be expected to be affected by statistical variation occurring in the microstructure over a range of a few microns. Cracks formed near crystallites will be pinned at a shorter length than cracks formed, at the same load, away from any dispersed particles. It is likely, then, that within the transition region, crack sizes associated with both the low- and high-load regimes will be present. This would explain the crack size histogram presented previously (Fig. 12) for the 1150°C heat-treatment where a bi-modal distribution of crack sizes is suggested for loads corresponding to the transition region, while only a uni-modal distribution is obtained for loads either lower or higher than the transition region.

#### B. Toughening in the Composite Regime

Microstructure is undoubtedly the key factor operative in the toughness increases obtained in the composite regime for the large-crystallite samples with increasing heat-treatment. A number of different toughness models have been proposed to account for toughness increases which result from crack-microstructure interaction. These models include crack bowing, crack deflection, surface roughness, ligament toughening, and microcrack toughening. Some of these models have already been discussed. A brief analysis of each model along with a consideration of its possible applicability to the cordierite glass-ceramic is presented in Table XVIII.

TABLE XVIII. EXAMINATION OF VARIOUS TOUGHNESS MODELS APPROPRIATE TO BRITTLE COMPOSITES

Model	Reference(s)	Physical Description	Toughening Expression	Comments
Crack bowing	Lange (26), Evans (27)	Particles act as impenetrable obstacles that force crack front to bow between particles	$\gamma_{comp.} = \gamma_m + T/\lambda$ where: T = line tension of crack front	Not applicable - predicts increase in $K_{comp}$ with decreasing $\lambda$ .
Crack deflection (mixed-mode)	Faber and Evans (38) Faber et al. (110)	Crack deflection by particles causes creation of Mode II (shearing) crack propagation	$K_{comp} = K_m (1+0.87V_f)$	Not applicable - predicts increase in $K_{comp}$ with increasing $V_f$ of dispersed phase; does not predict a particle size effect.
Surface roughness	Faber et al. (110)	Crack deflection by particles causes increase in crack surface area	$K_{comp} = 1/2 K_m$ $\left[ 1 + \frac{\left\{ \frac{\lambda + \bar{L}}{2} + \left( \frac{\bar{L}}{2} \right)^2 \right\}^{1/2}}{\frac{1}{2}(\lambda + \bar{L})} \right]$	Not applicable - predicts decrease in $K_{comp}$ with increasing $(\lambda + \bar{L})$

(continued on next page)

TABLE XVIII. (Continued)

Model	Reference(s)	Physical Description	Toughening Expression	Comments
Ligament toughening	Krstic et al. (111) Evans et al. (112)	Bridging of cracks by unfractured particles (ligaments) constrains crack propagation	$K_{\text{comp}} = K_m + \left(\frac{\pi D}{2}\right)^{1/2} \left[ \frac{\sigma_Y \phi}{\left\{1 + \frac{2}{3} \left(\frac{1}{V_f} - 1\right)\right\}^2} \right]$ <p>where: <math>\sigma_Y</math> = strength of particles  <math>D</math> = length of ligamented crack  <math>\phi</math> = constant</p>	Not applicable - predicts decrease in $K_{\text{comp}}$ with decreasing $V_f$
Microcrack toughening	Evans et al. (112) Evans and Faber (113)	Circumferential microcracking about particles decreases strain energy available to main crack front	$K_{\text{comp}} = K_m \left(\frac{1}{1-\eta}\right)$ <p>with <math display="block">\eta = \frac{4V_f}{\pi(\bar{L}_c/\bar{L})-1}</math></p> <p>where: <math>\bar{L}_c</math> = critical particle size needed to cause microcracking.</p>	Not applicable - microcracks were not observed in the cordierite glass-ceramic samples and $\alpha_m \neq \alpha_p$ (a pre-condition for circumferential microcracking); does however predict increase in $K_{\text{comp}}$ with increasing $\bar{L}$ .

( $K_{\text{comp}} = K_{Ic}$  in composite regime;  $K_m = K_{Ic}$  in matrix regime)

As seen from Table XVIII, all of the various toughening theories, with the exception of the microcrack model, predict a relationship between  $K_{Ic}$  and some microstructural variable that is completely opposite to that observed for the present glass-ceramic. The microcrack model does predict, based on the toughness and measured microstructural values for the glass-ceramic, that  $K_{Ic}$  in the composite regime should increase with an increase in crystallite size, despite the slight decrease that occurs in volume fraction of the dispersed phase. However, no microcracking was observed in any of the large-crystallite samples. In addition, no clear trend was observed between fracture stress and crystallite size, contrary to the  $\sigma_f \propto d^{-1/2}$  relationship anticipated from microcracking (Eq. I-12). Additionally, the model only pertains to circumferential microcracking, which, as discussed in Chapter I, occurs from mismatches in thermal expansion coefficient such that  $\alpha_m < \alpha_p$ . This requirement is not satisfied for the cordierite glass-ceramic, which, as shown by the X-ray diffraction and microstructure data reported in the preceding Chapter, consists of low-expansion  $\alpha$ -cordierite crystals dispersed in a much finer-grained matrix composed of  $\alpha$ -cordierite, and the high-expansion phases, low-cristobalite and pseudo-brookite solid solution.

Based on the SEM micrographs shown in Fig. 10, c and d, of crack-crystallite interaction in the composite regime, it would be anticipated that the toughness increases which occur with increased heat-treatment for the large-crystallite samples could be adequately

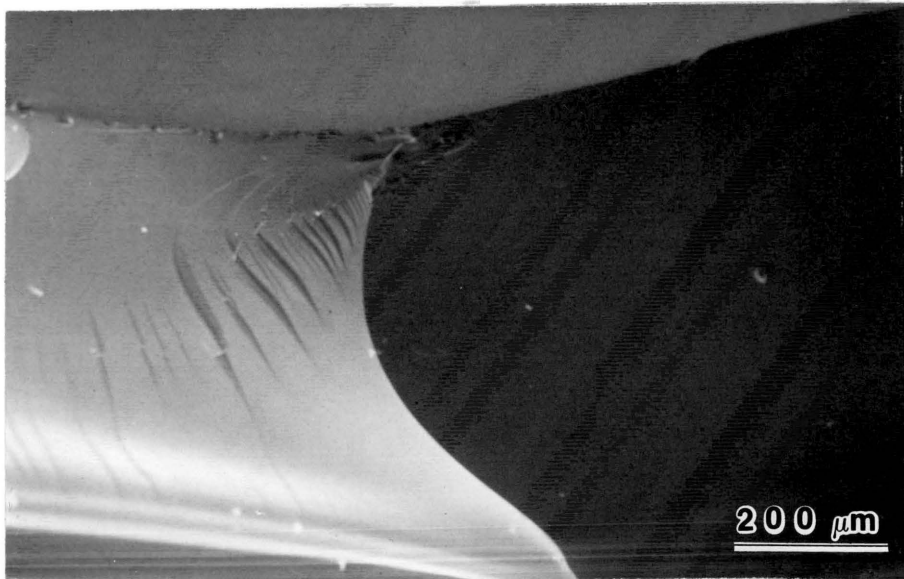
described by surface roughness effects. However, the analysis of Faber et al. (110) for surface roughness predicts that any toughness increases should be inversely proportional to  $(\lambda + \bar{L})$ . As seen in Table XIV,  $K_{Ic}$  for the large-crystallite samples increases with increasing  $(\lambda + \bar{L})$ , in direct contrast to this model. The maximum increase in relative toughness which Faber et al. predict from their model is 1.10. This agrees reasonably well with the relative toughness increase of 1.30 found for the cordierite glass-ceramic samples in the composite regime. In any case, surface roughness constitutes a major aspect of the fracture process for the large-crystallite samples, as can be seen in the electron micrographs of fracture surfaces shown in Fig. 20.

### C. Strength Behavior

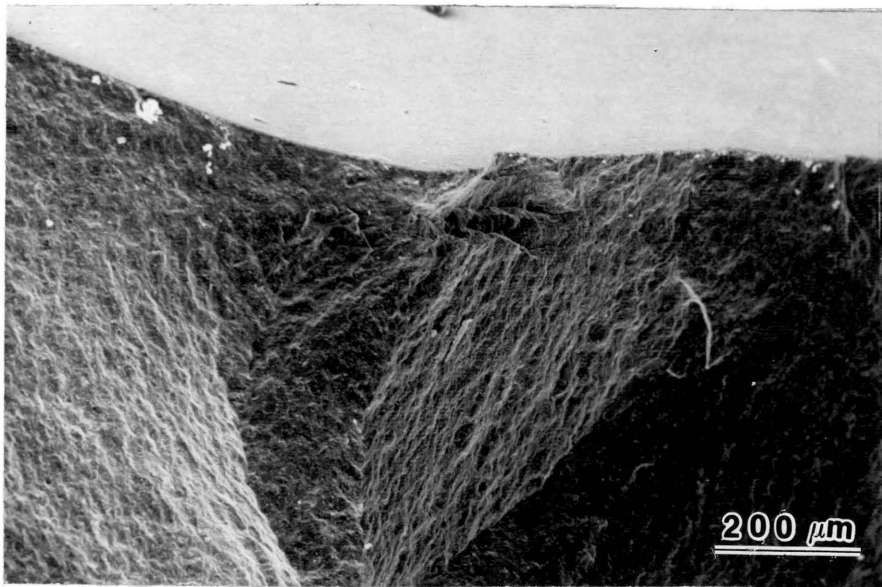
#### 1. Effect of crystallization

Comparison of the strength values (Table XV) obtained at the same level of indentation load for the original glass and heat-treated samples shows that transformation of the glass into the glass-ceramic was accompanied by a major increase in fracture strength. Contrary to the expectations of the microcrack theory, the presence of the dispersed phase in the cordierite glass-ceramic (at least for the range of crystallite sizes obtained in the present study) enhanced, rather than weakened, mechanical performance. The basis for this strengthening may be seen quite readily from the general form of the Griffith-Irwin expression:

$$\sigma_f = \frac{K_{Ic}}{Y\sqrt{c}} \quad (IV-1)$$



(a)



(b)

Fig. 20. SEM micrographs of fracture surfaces of the cordierite glass-ceramic for: a, the original glass; and b, a sample heat-treated at 820°C/2h plus 1260°C/8h.

where  $Y$  is a geometric factor and  $c$  is the flaw depth. As shown by the data in the preceding Chapter, crystallized samples possess a smaller crack size and a higher fracture toughness (at a given value of crack size) than does the original glass. Strengthening in the cordierite glass-ceramic, then, combines the two fundamental approaches used to achieve strength increases in brittle materials: limitations in the flaw size through dispersion-strengthening, and increases in the resistance to crack extension.

## 2. The constant strength region for the large crystallite samples

Examination of the strength-load curves (Figs. 19, a-d) shows that crystallization of the glass to form the large-crystallite glass-ceramic microstructure not only improves strength at a given value of indentation load, but perhaps of equal importance, reduces the strength losses sustained by the material as the indentation load becomes progressively higher. This effect may be most clearly illustrated by comparing strength behavior at low levels of indentation load (i.e.,  $\leq 300$ g.). With increasing indentation load for this load range, the strength of the original glass and the fine-precipitate samples decreases while that of the large-crystallite samples remains relatively-unchanged.

It is suggested that this constant strength region for the large-crystallite samples results from the presence of the transition region. It may be argued, perhaps, that this behavior is due to pre-existing flaws from the specimen preparation process which dominate the strength

behavior. However, examination of the strength data for all 3 of the large-crystallite samples show that mean strength following the 50g indentation load (the lowest load value employed) is lower than the unindented mean strength, indicating that the indentation flaws are indeed strength-controlling. Furthermore, this region of initially constant strength is not present for the original glass and the 1000°C strength series. Samples from these lots were handled and prepared in the same manner as the large-crystallite samples. If anything, flaws from the sample preparation process would be expected to dominate strength behavior at low loads for the original glass and 1000°C/8h samples, since these materials have a lower fracture toughness (and thus would be more susceptible to surface damage) than the large-crystallite heat-treatments.

Yet another explanation for this constant strength region is the possibility that it arises from interaction involving the residual stress field which surrounds the indentation. In fact, Lawn and co-workers (61, 114-5) have developed a model for median cracks which asserts that the residual stress field will interfere with the subsequent growth of these flaws. In this model, median flaws, of initial dimension,  $c_0$ , must, upon application of an external load, grow stably to some final dimension,  $c_m$ , before catastrophic failure can occur. This final length is given by

$$c_m = (4\chi_r P / K_{Ic})^{2/3} \quad (\text{IV-2})$$

where  $\chi_r$  is a proportionality constant given by

$$\chi_r = \frac{R}{V} (E/H)^{0.5} \quad (\text{IV-3})$$

with the material-independent constant,  $\frac{R}{V}$ , determined empirically by Anstis et al. (115) as  $0.016 \pm 0.004$ . Values of  $c_m$ , calculated at various loads from Eqs. IV-2 and IV-3, are listed in Table XIX for 2 strength series: the original glass, and a large-crystallite heat-treatment, the  $1150^\circ\text{C}/8\text{h}$  set. As seen in this Table,  $c_o < c_m$ , so that residual stress effects, characterized by stable growth of flaws from  $c_o$  to  $c_m$ , are predicted to occur for each of the samples and at all of the loads investigated. The fact that, for these 2 strength sets, the constant strength region was obtained only at low loads and only for the  $1150^\circ\text{C}/8\text{h}$  heat-treatment would rule out residual stress interactions as the causative agent for this phenomenon. Further support for this conclusion is provided by the lack of any observed effect on strength from the post-indentation annealing treatment reported in the preceding Chapter.

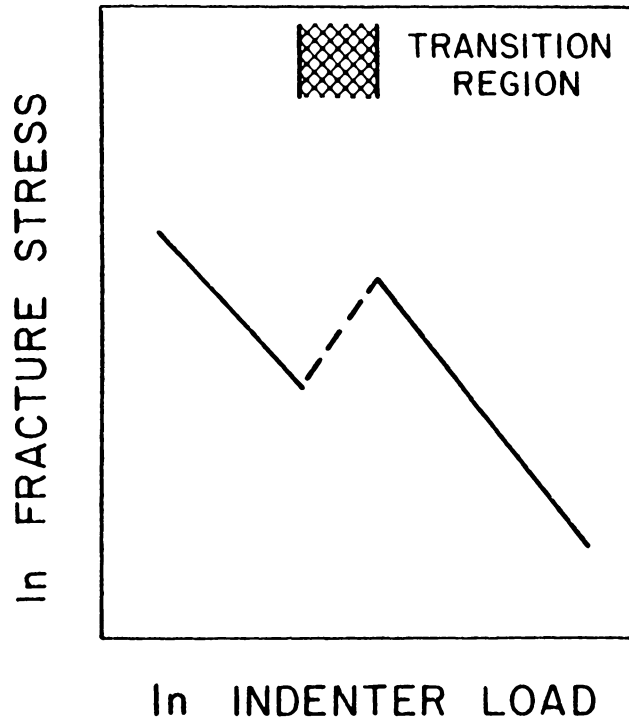
It seems reasonable, then, to conclude that the region of constant strength observed for the large-crystallite samples is due to the transition region. There are 2 models which are appropriate for describing the effect that the transition region will have on the strength behavior of indented samples. The first approach, which may be termed the "initial flaw size" model, assumes that the particular value of indentation flaw size which, from the Griffith-Irwin expression (Eq. IV-1), controls fracture strength, corresponds to that of the initial flaw. In other words, this model assumes that flaw size remains unchanged during the strength test, from the initial application of stress to the onset of catastrophic failure.

TABLE XIX. CALCULATED RESIDUAL STRESS EFFECTS ON CRACK  
 SIZE FOR TWO SAMPLES OF THE CORDIERITE GLASS-CERAMIC

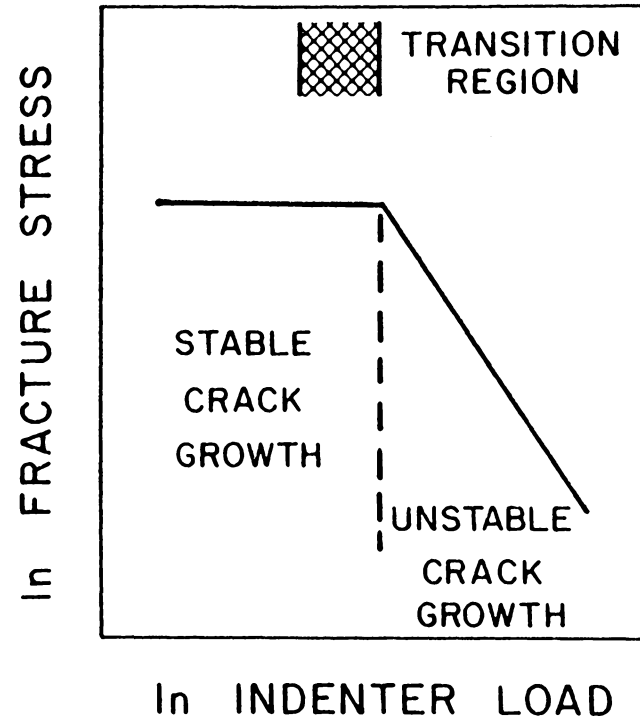
<u>Strength Series</u>	<u>Indentation Load(g)</u>	<u>Median Crack Size (<math>\mu\text{m}</math>)</u>	
		<u>Initial (measured), <math>C_0</math></u>	<u>Final (calculated), <math>C_m</math></u>
Original Glass	50	8.00	19.5
	100	13.4	31.5
	200	23.1	50.9
	500	48.5	95.0
	1000	85.1	156
820°C/2h+ 1150°C/8h	50	7.72	19.3
	75	10.1	25.0
	100	12.6	30.8
	125	12.4	30.1
	200	16.4	40.2
	500	30.0	75.2
	1000	46.8	114

Since flaw size increases with increasing indentation load for the large-crystallite samples in the low-and-high load regimes, fracture strength should show a continual decrease with increasing indentation load for both of these regimes. This is depicted schematically in Figure 21a. As load is increased across the transition region, this model predicts that the combined effect of decreasing crack size and increasing  $K_{Ic}$  should, from Eq. IV-1, cause a substantial increase to occur in fracture strength.

The second approach for describing the effect of the transition region on strength makes use of an analysis by Singh et al. (116) and Evans (117) which views a crack size dependent fracture toughness as constituting a barrier to unstable crack propagation. Because of the increase in fracture toughness that occurs as load is increased from below to above the transition region, flaws propagating in the matrix or low-toughness regime, must propagate stably until a flaw size is reached at which the local stress intensity factor attains the  $K_{Ic}$  value for the composite or high-toughness regime. Only at this point will catastrophic failure occur. For loads less than the high-load end of the transition region, strength remains unaffected by changes in indentation load since the value of critical flaw size remains invariant with load. Stable growth of flaws does not occur for flaws present in the composite regime because this load region lies beyond the transition region. The expected strength behavior for both the low- and high-load regimes is shown schematically in Figure 21b.



(a)



(b)

Fig. 21. Schematic of fracture stress-load relation for material with dual-regime fracture toughness: a, initial flaw size model; and b, stable crack growth model.

Of the two approaches, examination of the strength-load curves for the large-crystallite heat-treatments (Fig. 19, b-d) shows that the stable crack growth hypothesis of Singh et al. and Evans best describes the strength behavior. The strength increase obtained at the end of the transition region for the 1200°C/8h sample would indicate, however, that some aspects of the initial flaw size model are valid in describing the strength behavior of the cordierite glass-ceramic and should be incorporated in the Singh et al. - Evans analysis.

An immediate result from the stable crack growth hypothesis is that, for surface damage from contact events of such low magnitude that flaws are confined to the matrix, critical flaw size and fracture strength will be independent of the starting flaw size. Although it is the toughness of the matrix which determines the size of flaws introduced at low levels of surface contact, the conditions for ultimate failure from these flaws are controlled by the composite. Only in the high-load regime will critical flaw size and strength be determined by the initial flaw size. The implications of this behavior to the microstructural design of brittle composites with optimal resistance to surface damage will be considered in a subsequent Section.

### 3. The slope of the strength loss curve

Once indentation load has attained a value associated with the high-load regime, the strength-load behavior for the large-crystallite samples becomes qualitatively similar to that of the two strength series (the original glass and the 1000°C/8h set) which do not have a transition region: strength begins to decrease with increasing indentation

load. The slope of this strength degradation curve is determined by the nature of the indentation flaw. For median cracks, the strength of indented samples should vary with load,  $P$ , according to  $\sigma_f \propto P^{-1/3}$ . The expected strength-load relationship for Palmqvist cracks is, however, known with less certainty.

Several approaches to predicting the  $\sigma_f$ - $P$  slope are possible with Palmqvist cracks. One possibility is to assume that the eccentricity or aspect ratio of the semi-elliptical configuration remains unchanged over the entire load range that Palmqvist cracks occur. As a result, flaw depth should be directly proportional to the measured surface dimension,  $\ell$ . Since  $P \propto \ell$  for Palmqvist cracks, then, from the Griffith-Irwin expression (Eq. IV-1), the strength of indented samples should vary according to  $\sigma_f \propto P^{-1/2}$ .

An alternative approach for Palmqvist cracks is to assume, as speculated by Niihara (118), that the variation in stress intensity factor with position along the crack front of a semi-elliptical surface crack will cause the eccentricity to vary with crack size, so that any direct proportionality between  $\ell$  and flaw depth will not be maintained over a wide range in crack size. Using this approach, Niihara (118) has obtained the following relationship between fracture stress and indentation load for Palmqvist cracks:

$$\sigma_f \propto P^{\frac{n-1}{4}} \quad (\text{IV-4})$$

where  $n$  is the exponent for the load-dependence of hardness (i.e.,  $H = kP^n$ ). Examination of the hardness data for several of the glass-ceramic samples shows a weak load-dependence, with  $0.04 \leq n \leq 0.12$ . These

end values give an expected slope (Eq. IV-4) for the  $\ln\sigma_f - \ln P$  relationship for Palmqvist cracks of  $-0.22$  to  $-0.24$ .

The linear regression data listed in Table XVI for the loss of strength curves show a slope of about  $-0.22$  for the large crystallite samples. This is in excellent agreement with the slope value predicted by Niihara's Palmqvist crack analysis. For the two sample sets that do not have a transition region, the slope data in Table XVI for the  $1000^\circ\text{C}/8\text{h}$  heat-treatment are particularly interesting. This heat-treatment results in hardness values (see Table XVII) near the maximum of the hardness curve discussed in the preceding Chapter, so that a wider range of  $c/a$  ratios may be obtained over a given load interval than for the other samples. At low loads ( $c/a \leq 2.2$ ) as seen in Table XVI, the strength data can be fitted to a linear regression curve with a slope of  $-0.20$ . At higher loads ( $c/a \geq 2.9$ ) the best-fit straight line has a slope of  $-0.39$ . This apparent changeover from Palmqvist to median crack indentation mechanics is consistent with the analysis of Niihara et al. (71,72) which predicts Palmqvist cracks at  $c/a \leq 2.5$ , and median cracks at  $c/a \geq 2.5$ . The same trend may also be observed for the strength data of the original glass, although the curve for the high-load region is based on data from only 2 indentation loads. No such slope change was suggested in the strength data of the large-crystallite samples, since  $c/a < 2.0$  for these samples over the whole load range investigated.

#### D. Comments on Measurement of Fracture Toughness of Brittle Materials

Fracture toughness values of brittle materials are most typically obtained by the double cantilever beam, double torsion, notched beam, or short rod tests. These methods may all be classified as macroscopic techniques since they involve measuring the material's resistance to the extension of a crack some several centimeters in length. Crack sizes as large as this must lie well beyond the transition region. As a result, the  $K_{Ic}$  values obtained from these procedures will not be appropriate for predicting the extent of surface damage from contact events corresponding to loads below the transition region.

Similarly, very different fatigue-failure parameters most likely would be measured depending on whether the crack was propagating in the high- or low-load regime. Experimental data for crack velocity as a function of stress intensity factor obtained by the double cantilever beam technique would, most likely, pertain to material behavior in the composite regime. This may well disagree with fatigue measurements (such as from the 4-point bend test) on flaws with sizes corresponding to the low-load regime. This discrepancy, indeed, has been observed by Pletka and Wiederhorn (87) for the cordierite glass-ceramic.

Because of the energy barrier to crack propagation represented by the increase in fracture toughness occurring within the transition region, it may well be that the transition region constitutes a natural obstacle to the introduction of large flaws. As a result, the flaw

size occurring at the start of the transition region may be that found in most ceramic materials which have experienced reasonable levels of surface contact. Support for this is provided by the study of Freiman et al. (119) who found that critical flaw size remained the same despite variations in the heat-treatment schedule for a barium silicate glass-ceramic. This same effect is suggested for the cordierite glass-ceramic in Table X, where flaw size at the start of the transition region is seen to vary by only a few microns for most of the samples, despite changes occurring with crystallization temperature.

#### E. Residual Stress Effects and the Determination of Fracture Toughness by the Indentation Method

The residual stress field constitutes the major driving force for radial cracks which form during unloading. Using a median crack model, Lawn and co-workers (115,116) have shown that median crack size and fracture toughness are related according to

$$K_{Ic} = \frac{\chi_r P}{c^{3/2}} \quad (IV-5)$$

where  $\chi_r$  is a proportionality constant related to the magnitude and spatial distribution of the residual stress field about the indentation. As defined previously in Eq. IV-3,  $\chi_r$  represents the product of  $\$V^R$ , a material-independent constant, and  $(E/H)^{0.5}$ . It is interesting that this latter term, which is the only material-dependent term to appear in this residual stress analysis, also appears in almost identical form (as  $(E/H)^{0.4}$ ) in indentation toughness expressions developed by Niihara et al (71,72) and Evans and Charles (69) from

curve-fitting and dimensional analysis of indentation and  $K_{Ic}$  data reported for a large number of brittle materials. This suggests that these latter approaches already incorporate residual stresses in their indentation mechanics.

Initially, during the development of Lawn's median crack model, an elastic, rather than an elastic-plastic, analysis was used to relate fracture toughness with crack size (120,121):

$$K_{Ic} = \frac{P}{\beta c^{3/2}} \quad (IV-6)$$

Although this expression appears qualitatively similar to Eq. IV-5, the proportionality constant  $\beta$  does not depend on any deformation response of the material, nor does it incorporate the effect of residual stresses. Instead,  $\beta$  is determined essentially by the half-angle of the indenter, with minor corrections made for Poisson's ratio of the indented material, frictional forces during indentation, and free surface effects.

Fracture toughness values determined both by the Palmqvist crack model (Eq. I-21b) developed by Niihara et al. and by the median crack expressions (both including and neglecting residual stresses) originated by Lawn and co-workers are shown in Table XX for several of the cordierite glass-ceramic samples. The reported value (116) of  $\frac{R}{V} = 0.016$  was used in the calculations to determine  $\chi_r$ . The value of  $\beta$  needed in Eq. IV-6 was determined empirically from this expression by fitting measured indentation values (reported in the preceding Chapter) for soda-lime-silica glass to the literature value of

TABLE XX. COMPARISON OF FRACTURE TOUGHNESS VALUES CALCULATED  
FOR SEVERAL SAMPLES OF CORDIERITE GLASS-CERAMIC

Heat-Treatment (Temp. and Time)	Indentation Load (g.)	c/a Ratio	Fracture Toughness ( $\text{MNm}^{-3/2}$ )		
			Median Crack Model		Palmqvist Crack Model (Eq. I-21b)
			Residual Stresses Included (Eq. IV-5)	Residual Stresses Neglected (Eq. IV-6)	
820°C/2h+1150°C/8h (strength series)	50	1.45	1.55	2.25	1.52
	75	1.53	1.57	2.24	1.54
	100	1.66	1.51	2.15	1.49
	125	1.44	1.93	2.75	1.93
	200	1.51	2.03	2.90	2.00
	500	1.73	3.08	2.92	2.08
	1000	1.91	2.13	3.00	2.22
Original Glass	50	1.60	1.22	2.13	1.25
	100	1.84	1.14	1.96	1.24
	200	2.20	1.05	1.39	1.21
	500	2.84	0.88	1.43	1.20
	1000	3.35	0.79	1.23	1.22
820°C/2h+1000°C/8h (strength series)	50	1.71	1.29	2.25	1.35
	100	1.84	1.35	2.28	1.44
	200	2.18	1.24	2.05	1.43
	350	2.88	0.92	1.50	1.28
	500	3.05	0.92	1.42	1.31
	750	3.21	0.94	1.45	1.39
	1000	3.31	0.95	1.45	1.44

$K_{Ic} = 0.758 \text{ MNm}^{-3/2}$  determined for this material by the double cantilever beam technique (39). A value of  $\beta = 14.0$  was obtained in this manner. The indentation data needed to calculate the  $K_{Ic}$  values listed in Table XX were all reported in the preceding Chapter.

Inspection of the toughness values for the sample crystallized at  $1150^\circ\text{C}$  for 8 hours shows excellent agreement existing between  $K_{Ic}$  determined by the Palmqvist model and that based on the residual stress-modified median crack approach. The toughness values for the median crack model which neglects residual stresses are substantially greater than those calculated by either of the other two approaches.

Note from Table XX that all of the indentation data for the  $1150^\circ\text{C}$  sample are for  $c/a \leq 1.9$ . Examination of the toughness values obtained by the different models for the original glass and the sample crystallized at  $1000^\circ\text{C}$  shows that the agreement between  $K_{Ic}$  determined by the Palmqvist model and that based on incorporating residual stresses into the median crack analysis does not exist at higher  $c/a$  ratio. Disagreement is seen to occur at  $c/a \geq 2.2$ . At the higher  $c/a$  ratios, relatively good agreement in toughness is obtained between the Palmqvist crack model and the median crack model which does not incorporate residual stresses.

It appears, then, that a unified median crack model is unable to give satisfactory fracture toughness values over a wide range of  $c/a$  ratios. It may be recalled that Niihara et al. (71,72) obtained satisfactory fracture toughness expressions from indentation data reported for a large number of brittle materials only by differentiating between 2 different regimes of  $c/a$  ratio: for  $c/a \leq 2.5$ , the Palmqvist crack model applied based on the crack size parameter,  $\ell$ ; for  $c/a \geq 2.5$ ,

the median crack model was most appropriate. The difficulties encountered when trying to fit either of the two median crack models discussed in this Section to the entire range of  $c/a$  ratios point out the inadequacies inherent in attempting to describe all sharp indenter fracture mechanics by means of a single crack geometry.

#### F. Crystallization Effects on the Vicker's Hardness

Trends similar to the maximum which was obtained for the Vicker's hardness as a function of heat-treatment temperature for the cordierite glass-ceramic have also been reported for density, strength, and thermal expansion in a nearly-identical cordierite glass-ceramic by Kumar and Nag (103). These investigators attributed this behavior to internal stress effects caused by density mismatch between any uncrystallized glass and crystalline phases present. However, Kumar and Nag provided no quantitative phase data to substantiate their hypothesis. Published reports (86, 91) contradict their analysis since essentially no residual glassy phase has been detected much beyond the 1000°C heat-treatment.

It seems more likely that the increase in hardness which occurs with initial heat-treatment of the original glass arises from dispersion-hardening of the glass by the stuffed quartz precipitates. Such an effect has been observed (122) for  $MgFe_2O_4$  precipitates in  $MgO$ . The hardness decrease which occurs with increasing heat-treatment beyond the 1100°C/1h treatment coincides with the stuffed quartz  $\rightarrow$   $\alpha$ -cordierite transformation. These heat-treatments result in progressive growth of  $\alpha$ -cordierite crystals from a fine-grained

crystalline matrix. The accompanying hardness decrease is most probably caused by Hall-Petch behavior. With this phenomenon, an increase in crystallite size of a polycrystalline metal or ceramic results in less grain boundary area present (per unit volume of sample) to hamper dislocation motion. As a consequence, the ability of the material to deform, at least on a microscopic basis, is increased, which results in a decrease in hardness.

#### G. Microstructural Design for Optimal Resistance to Surface Damage

Upon first consideration, it might be presumed that increased resistance to surface damage in a brittle composite could best be achieved by improving the resistance to surface damage of each of the various phases. Most likely, as part of this effort, special emphasis would be given to improving the fracture toughness of both the matrix and dispersed phases. However, based on the present analyses, such an approach would cause a deterioration, rather than an improvement, to occur in the material's ability to resist surface damage.

The primary criterion of resistance to surface damage is the ability of a material to withstand surface contact without sustaining some subsequent loss in mechanical performance. This can best be achieved by having a dual regime of fracture toughness such that the associated transition region extends over as wide a range of contact loads as possible. In this manner, the load region over which stable crack growth occurs is maximized, so that strength re-

mains unaffected by contact events over a wide range of contact loads.

Inspection of the several crack size-load curves shown in Figure 11 indicates that the width of the transition region may be extended by increasing the difference in  $K_{Ic}$  between the low- and high-toughness regimes. This is why the procedure suggested at the beginning of this Section (i.e., of increasing the fracture toughness of both the matrix- and composite-regimes) could well prove ineffective ( $K_{Ic}$  difference remains unchanged) or even detrimental ( $K_{Ic}$  difference is narrowed) to improving resistance to surface damage. By decreasing the fracture toughness of the matrix and increasing this property for the composite, the ability of the material to sustain surface damage should be improved. Although a larger size of flaws will be introduced at low levels of contact load, the capability of these same flaws to cause failure during subsequent loading will be drastically impaired. Equally important, this procedure will decrease the size of flaws introduced in the high-toughness regime where fracture strength is controlled by initial flaw size. To achieve a high  $K_{Ic}$  composite - low  $K_{Ic}$  matrix material, emphasis should be given to decreasing the particle size of the matrix so that any toughening interactions with cracks are eliminated and a continuum response to flaw introduction is achieved. Conversely, the particle size of the dispersed phase should be increased, with the stipulation that the particle size selected be below the critical value needed for spontaneous microcracking to occur.

#### H. Suggestions for Future Work

Stable growth of flaws under an applied stress has already been mentioned in this Chapter as the underlying failure mechanism for flaws introduced in the matrix regime for the large-crystallite samples. Since the transition region most likely limits flaws from many real contact events to the low-toughness regime, an investigation needs to be made of the various factors (such as microstructure) active in sub-critical crack growth behavior in a brittle composite. Information gained from this study could result in further improvement in designing ceramic components with maximum resistance to surface damage.

Finally, although the vast bulk of ceramic structures are composites, one major group is not: glasses. Failure from surface contact events is, of course, an everyday occurrence associated with these materials. Recently (109,123), it has been shown that phase separation can lead to substantial improvements in toughening for glasses. Phase separation has been observed (124) following heat-treatment for 2 commercially-important glass systems:  $\text{Na}_2\text{O}-\text{B}_2\text{O}_3-\text{SiO}_2$ , and  $\text{Na}_2\text{O}-\text{CaO}-\text{SiO}_2$ . Efforts should be directed at optimizing the phase separation microstructure so that maximum toughness and resistance to surface damage may be achieved. Obviously, this may prove to be detrimental to other engineering properties such as optical transmittance. It may be possible, however, by means of a higher-temperature heat-treatment process than is typically employed during the commercial glass-annealing operation for substructures to be developed

in silicate glasses which will give an improved resistance to surface damage, and yet will produce only minimal opalescence and loss of optical quality.

## V. CONCLUSIONS

1. The microhardness indentation technique was found to constitute a powerful tool for simulating damage from surface contact events and for permitting direct characterization of microstructural influences on the flaw introduction process.

2. Crack-crystallite interactions, consisting of crack pinning at flaw sizes approximately equal to the mean free path distance between dispersed phase crystallites and crack deflection at larger flaw sizes, were found to significantly affect fracture behavior in cordierite glass-ceramic samples comprised of a fine-grained matrix containing larger ( $\sim 1-2 \mu\text{m}$ ) crystallites ("large-crystallite" microstructure). These interactions were not present in the samples at flaw sizes less than the mean free path distance, and were not observed at all in the original glass or in samples heat-treated to yield only a uniform, fine-grained ( $< 0.1 \mu\text{m}$ ) microstructure.

3. The crack pinning interaction for the large-crystallite samples was shown to limit the size of introduced flaws, thus confirming the basic concept of the dispersion-strengthening model for brittle composites.

4. The crack deflection interaction for the large-crystallite samples was found to be microstructure-dependent, with fracture toughness increasing linearly with both increasing crystallite size and increasing mean free path of the dispersed phase. These toughness increases were not adequately described by existing models of crack-crystallite interaction.

5. The lack of any crack-crystallite interactions at small flaw sizes, combined with the extensive interactions which occurred as flaw size increased, gave rise to a crack size-dependent fracture toughness for the large crystallite samples. This phenomenon, since it required stable growth of precursor flaws to precede any structural failure, greatly enhanced the ability of the glass-ceramic samples to avoid potentially-damaging effects on strength from surface contact.

6. The overall effect of decreased flaw size from crack pinning and increased fracture toughness from crack deflection was to produce strength values for the large-crystallite cordierite glass-ceramic samples which were vastly superior to those of the original glass.

VI. LITERATURE CITED

1. P. W. McMillan, pp. 164-165 in Glass Ceramics, 2nd ed., Academic Press, NY (1979).
2. Muneo Watanabe, R. V. Caporali, and R. E. Mould, pp. 23-28 in Symposium on Nucleation and Crystallization in Glasses and Melts, ed. by Margie K. Reser, Geraldine Smith, and Howard Insley, American Ceramic Society, Columbus, OH (1962).
3. C. E. Inglis, Trans. Inst. Nav. Archit., 55 (1913) 219-230.
4. A. A. Griffith, Phil. Trans. Roy. Soc. (London), 221A (1920) 163-198.
5. E. Orowan, in Fatigue and Fracture of Metals, ed. by W. M. Murry, Wiley, NY (1958).
6. D. P. H. Hasselman, J. A. Coppola, D. A. Krohn, and R. C. Bradt, Mater. Res. Bull., 7 (1972) 769-772.
7. G. R. Irwin, in Handbuch der Physik, Vol. 6, Springer-Verlag, Heidelberg (1958).
8. G. C. Sih, Handbook of Stress Intensity Factors, Lehigh Univ. Press, Bethlehem, PA (1973).
9. D. Weyl, Ber. Deutsch. Keram. Ges., 36 (1958) 319-324.
10. Jorgen Selsing, J. Am. Ceram. Soc., 44 (1961) 419.
11. A. K. Khaund, V. D. Krstic, and P. S. Nicholson, J. Mater. Sci., 12 (1977) 2269-2273.
12. D. B. Binns, pp. 315-334 in Science of Ceramics, Vol. I, ed. by G. H. Stewart, Academic Press, NY (1962).
13. W. J. Frey and J. D. Mackenzie, J. Mater. Sci., 2 (1967) 124-130.
14. Marcus P. Borom, Anna M. Turkalo, and Robert H. Doremus, J. Am. Ceram. Soc., 58 (1975) 385-391.
15. F. Erdogan, pp. 245-267 in Fracture Mechanics of Ceramics, Vol. 1, ed. by R. C. Bradt, D. P. H. Hasselman, and F. F. Lange, Plenum, NY (1974).
16. R. R. Tummala and A. L. Friedberg, J. Am. Ceram. Soc., 52 (1969) 229-229.

17. J. C. Swearingen, E. K. Beauchamp, and R. J. Eagan, pp. 973-987 in Fracture Mechanics of Ceramics, Vol. 4, ed. by R. C. Bradt, D. P. H. Hasselman, and F. F. Lange, Plenum, NY (1978).
18. Marcus P. Borom, *J. Am. Ceram. Soc.*, 60 (1977) 17-21.
19. R. W. Davidge and T. J. Green, *J. Mater. Sci.*, 3 (1968) 629-634.
20. Megumi Tashiro, *Glass Ind.*, 47 (1966) 428-435.
21. Yoshikazu Utsumi and Sumio Sakka, *J. Am. Ceram. Soc.*, 53 (1970) 286-287.
22. A. J. Stryjak and P. W. McMillan, *J. Mater. Sci.*, 13 (1978) 1794-1804.
23. J. N. Goodier, *J. Appl. Mech.*, 1 (1933) 39-44.
24. D. P. H. Hasselman and R. M. Fulrath, *J. Am. Ceram. Soc.*, 50 (1967) 399-404.
25. J. C. Swearingen and R. J. Eagan, *J. Mater. Sci.*, 11 (1976) 1857-1866.
26. F. F. Lange, *Phil. Mag.*, 22 (1970) 983-992.
27. A. G. Evans, *Ibid.*, 26 (1972) 1327-1344.
28. F. F. Lange, *J. Am. Ceram. Soc.*, 54 (1971) 614-620.
29. David J. Green, Patrick S. Nicholson, and J. David Embury, *J. Mater. Sci.*, 14 (1979) 1657-1661.
30. Arup K. Khaund and Patrick S. Nicholson, *Ibid.*, 15 (1980) 177-187.
31. F. F. Lange, pp. 1-44 in Composite Materials, Vol. 5, ed. by Lawrence J. Broutman, Academic Press, NY (1974).
32. David J. Green, Patrick S. Nicholson, and J. David Embury, *J. Mater. Sci.*, 14 (1979) 1413-1420.
33. J. S. Nadeau and R. C. Bennett, pp. 961-972 in Fracture Mechanics of Ceramics, Vol. 4, op. cit.
34. J. S. Nadeau and J. I. Dickson, *J. Am. Ceram. Soc.*, 63 (1980) 517-523.
35. D. J. Green and P. S. Nicholson, pp. 945-960 in Fracture Mechanics of Ceramics, Vol. 4, op. cit.

36. Mark A. Stett and R. M. Fulrath, *J. Am. Ceram. Soc.*, 53 (1970) 5-13.
37. I. M. Stewart, I. Brough, and L. Green, *J. Mater. Sci.*, 2 (1967) 63-69.
38. K. T. Faber and A. G. Evans, Paper 126-B-81, presented at Annual Meeting, Am. Ceram. Soc., Wash., DC (1981).
39. S. M. Wiederhorn, *J. Am. Ceram. Soc.*, 52 (1969) 99-105.
40. R. A. Palmer, W. R. Lindberg, and L. L. Hench, *Ibid.*, 62 (1979) 319-320.
41. B. R. Lawn, E. R. Fuller, and S. M. Wiederhorn, *Ibid.*, 58 (1975) 193-197.
42. B. R. Lawn, S. M. Wiederhorn, and H. H. Johnson, *Ibid.*, 58 (1975) 428-432.
43. A. G. Evans, pp. 303-331 in Fracture Mechanics of Ceramics, Vol. 3, ed. by R. C. Bradt, D. P. H. Hasselman, and F. F. Lange, Plenum, NY (1978).
44. A. G. Evans, pp. 1-68 in Treatise on Science and Technology, Vol. 16, ed. by C. M. Preece, Academic Press, NY (1972).
45. A. G. Evans, pp. 1-14 in The Science of Ceramic Machining and Finishing, II, ed. by B. J. Hockey and R. W. Rice, National Bureau of Standards Special Publication, U.S. Govt. Printing Office, Wash., DC (1979).
46. H. P. Kirchner, P. M. Gruver, and D. M. Richard, pp. 23-42, *Ibid.*
47. D. P. H. Hasselman and R. M. Fulrath, *J. Am. Ceram. Soc.*, 49 (1966) 68-72.
48. R. L. Fullman, *Trans. AIME*, 197 (1953) 447-452.
49. B. R. Lawn and D. B. Marshall, pp. 205-229 in Fracture Mechanics of Ceramics, Vol. 3, op. cit.
50. R. P. Wahí and B. Ilschner, *J. Mater. Sci.*, 15 (1980) 875-885.
51. S. W. Freiman and L. L. Hench, *J. Am. Ceram. Soc.*, 55 (1972) 86-90.
52. D. I. H. Atkinson and P. W. McMillan, *J. Mater. Sci.*, 11 (1976) 994-1002.

53. P. Hing and P. W. McMillan, *Ibid.*, 8 (1973) 1041-1048.
54. N. Miyata and H. Jinno, *Ibid.*, 7 (1972) 973-982.
55. H. Hertz, Miscellaneous Papers, MacMillan, NY (1896).
56. D. Tabor, p. 112-113 in The Hardness of Metals, Clarendon Press, Oxford, England (1951).
57. C. M. Perrott, *Wear*, 45 (1977) 293-309.
58. A. G. Evans, pp. 112-135 in Fracture Mechanics Applied to Brittle Materials, ed. by S. W. Freiman, Special Technical Pub. 678, American Society for Testing and Materials, Philadelphia, PA (1979).
59. B. R. Lawn, A. G. Evans, and D. B. Marshall, *J. Am. Ceram. Soc.*, 63 (1980) 574-580.
60. B. R. Lawn and M. V. Swain, *J. Mater. Sci.*, 10 (1975) 113-122.
61. B. R. Lawn, A. G. Evans, and D. B. Marshall, *J. Am. Ceram. Soc.*, 63 (1980) 574-581.
62. S. Palmqvist, *Jernkontorets Ann.*, 141 (1957) 300.
63. V. W. Dawihl and G. Altmeyer, *Z. Metallk.*, 55 (1964) 231-237.
64. James Lankford and David L. Davidson, *J. Mater. Sci.*, 14 (1979) 1662-1668.
65. M. V. Swain and J. T. Hagan, *J. Phys. D., Appl. Phys.*, 9 (1976) 2201-2214.
66. J. T. Hagan and M. V. Swain, *Ibid.*, 11 (1978) 2091-2102.
67. J. T. Hagan, M. V. Swain, and J. E. Field, pp. 15-21 in The Science of Ceramic Machining and Finishing, II, op. cit.
68. A. G. Evans and T. R. Wilshaw, *Acta Metall.*, 24 (1976) 939-956.
69. A. G. Evans and E. A. Charles, *J. Am. Ceram. Soc.*, 59 (1976) 370-371.
70. J. E. Blendell, Sc. D. Thesis, Massachusetts Institute of Technology, Cambridge, MA (1979).
71. K. Niihara, R. Morena, and D. P. H. Hasselman, *J. Mater. Sci.* (to be published, 1981).

72. K. Niihara, R. Morena, and D. P. H. Hasselman, presented at International Symposium on Fracture Mechanics of Ceramics, University Park, PA (July 1981).
73. B. R. Lawn and A. G. Evans, *J. Mater. Sci.*, 12 (1977) 2195-2199.
74. M. A. Moore and F. S. King, *Wear*, 60 (1980) 123-140.
75. Samuel R. Scholes, pp. 311-328 in Modern Glass Practice, Industrial Publ., Chicago (1935).
76. J. J. Hammel, pp. 1-9 in Advances in Nucleation and Crystallization in Glasses, ed. by L. L. Hench and S. W. Freiman, American Ceramic Society, Columbus, OH (1971).
77. R. Becker, *Ann. Phys.* 32 (1938) 128 (cited in ref. 1, p. 31).
78. H. R. Swift, *J. Am. Ceram. Soc.*, 30 (1947) 165-169.
79. Stanley D. Stookey, U. S. Patent 2,920,971 (1960).
80. Werner Vogel and Klaus Gerth, pp. 11-22 in Symposium on Nucleation and Crystallization in Glasses and Melts, op. cit.
81. S. M. Ohlberg, H. R. Golob, and D. W. Strickler, pp. 55-62, *Ibid.*
82. S. D. Stookey and R. D. Maurer, pp. 78-101 in Progress in Ceramic Science, Vol. 2, ed. by J. E. Burke, Pergamon, NY (1962).
83. P. W. McMillan, pp. 97-153 in Glass Ceramics, op. cit.
84. D. R. Stewart, pp. 83-90 in Advances in Nucleation and Crystallization in Glasses, op. cit.
85. Girraj K. Bansal and Winston Duckworth, *J. Am. Ceram. Soc.*, 60 (1977) 304-310.
86. K. Chyung, G. E. Youngblood, and D. P. H. Hasselman, *Ibid.*, 61 (1978) 530.
87. B. J. Pletka and S. M. Wiederhorn, pp. 745-759 in Fracture Mechanics of Ceramics, Vol. 4., op. cit.
88. R. C. De Vekey and A. J. Majumder, *Min. Mag.*, 37 (1970) 771-779.
89. R. D. Maurer, *J. Appl. Phys.*, 33 (1962) 2133-2139.
90. W. Schreyer and J. F. Schairer, *J. Petrology*, 2 (1961) 324-406.
91. A. G. Gregory and T. J. Veasey, *J. Mat. Sci.*, 6 (1971) 1312-1321.

92. T. I. Barry, J. M. Cox, and R. Morrel, *Ibid.*, 13 (1978) 594-610.
93. M. D. Karkhanavala and F. A. Hummel, *J. Amer. Ceram. Soc.*, 36 (1953) 389-392.
94. K. Chyung to D. P. H. Hasselman, written communication (May 5, 1978).
95. J. L. Lytton, "Operating Instructions for JEOLCO JSM-2", Dept. of Materials Engineering, Virginia Polytechnic Institute and State University, Blacksburg, VA (August, 1979).
96. J. E. Hilliard, pp. 45-76 in Quantitative Microscopy, ed. by Robert T. DeHoff and Frederick N. Rhines, McGraw-Hill, NY (1968).
97. W. D. Kingery, H. K. Bowen, and D. R. Uhlman, pp. 526-530 in Introduction to Ceramics, 2nd ed., Wiley, NY (1976).
98. J. E. Ritter, Jr., K. Jakus, A. Batakis, and N. Bandyopadhyay, pp. 419-424 in Proceedings of XII International Conference on Glass, ed. by R. H. Doremus, W. C. LaCourse, J. D. Mackenzie, J. R. Varner, and W. W. Wolf, North-Holland, NY (1980).
99. J. B. Wachtman, Jr., Webster Capps, and J. Mandel, *J. of Materials*, 7 (1972) 188-194.
100. Standard F394-78, pp. 783-789 in Annual Book of ASTM Standards, Part 43, Amer. Soc. for Testing and Materials, Philadelphia, PA (1978).
101. A. F. Kirstein and R. M. Woolley, *J. Res. Nat. Bur. Stnd.*, 71C (1967) 1-10.
102. K. Chyung to D. P. H. Hasselman, written communication (June 4, 1980).
103. S. Kumar and B. B. Nag, *Trans. Indian Ceram. Soc.*, 22 (1963) 30-36.
104. See, for example, Wilfred J. Dixon and Frank J. Massey, Jr., pp. 150-187 in Introduction to Statistical Analysis, 3rd ed., McGraw-Hill, NY (1969).
105. Prabhat K. Gupta and Nancy J. Jubbs, *J. Am. Ceram. Soc.*, 64 (1981) C-112 - C-114.
106. S. Smith, P. Magnusen, and B. J. Pletka, to be published in ASTM Symposium on Fracture Mechanics for Ceramics, held in Chicago, 1980.

107. Minutes of Subcommittee Meeting E24-07, Amer. Soc. for Testing and Materials, held in Pittsburgh, Nov. 1, 1979.
108. David Lewis III, J. Am. Ceram. Soc., 64 (1981) 82-86.
109. C. J. Brinker and J. J. Mecholsky, Paper 9-JV-80 presented at Annual Meeting, Am. Ceram. Soc., Chicago (1980).
110. K. T. Faber, A. G. Evans, and M. D. Drory, "A Statistical Analysis of Crack Deflection as a Toughening Mechanism in Ceramic Materials," paper presented at International Symposium on Fracture Mechanics of Ceramics, University Park, PA (July, 1981), to be published in Fracture Mechanics of Ceramics, Vol. 5 and 6, ed. by R. C. Bradt, A. G. Evans, D. P. H. Hasselman, and F. F. Lange, Plenum, NY (1981).
111. Vladimir V. Krstic, Patrick S. Nicholson, and Richard G. Hoagland, J. Am. Ceram. Soc., 64 (1981) 499-504.
112. A. G. Evans, A. H. Heuer, and D. L. Porter, pp. 525-556 in Fracture 1977, Vol. 1, ed. by D. M. R. Taplin, Univ. of Waterloo Press, Waterloo, Ontario, Canada (1977).
113. A. G. Evans and K. T. Faber, J. Am. Ceram. Soc., 64 (1981) 394-398.
114. Brian R. Lawn, "The Indentation Crack as a Model Surface Flaw", paper presented at International Symposium on Fracture Mechanics of Ceramics, Univ. Park, PA (1981), to be published in Fracture Mechanics of Ceramics, Vol. 5 and 6, op. cit.
115. G. R. Anstis, P. Chantikul, B. R. Lawn, and D. B. Marshall, J. Am. Ceram. Soc., 64 (1981) 533-538.
116. J. P. Singh, A. V. Virkar, D. K. Shetty, and R. S. Gordon, *Ibid.*, 62 (1979) 179-183.
117. A. G. Evans, *Ibid.*, 63 (1980) 115-116.
118. K. Niihara to R. Morena, written communication (Oct. 20, 1981).
119. S. W. Freiman, G. Y. Onoda, Jr., and A. G. Pincus, J. Am. Ceram. Soc., 57 (1974) 8-12.
120. B. R. Lawn and M. V. Swain, J. Mater. Sci., 10 (1975) 113-122.
121. B. R. Lawn and E. R. Fuller, *Ibid.*, 10 (1975) 2016-2024.
122. E. W. Kruse III and M. E. Fine, J. Am. Ceram. Soc., 55 (1972) 33-37.

123. N. Miyata and H. Jinno, *J. Mater. Sci.*, 16 (1981) 2205-2217.
124. D. R. Uhlmann and A. G. Kolbeck, *Phys. Chem. of Glasses*, 17 (1976) 146-158.

**The vita has been removed from  
the scanned document**

EFFECTS OF CRACK-CRYSTALLITE INTERACTION  
ON THE FRACTURE BEHAVIOR OF A CORDIERITE GLASS-CERAMIC

by

Robert M. Morena

(ABSTRACT)

Crack-microstructure interactions occurring during the flaw introduction process were studied in a model brittle composite, a cordierite glass-ceramic. Microstructural effects associated with the repropagation of the introduced flaws under the imposition of a mechanical load were also examined.

Two general types of crystallized microstructures were investigated for samples heat-treated from the original glass: a fine structure composed of a uniform precipitation of very small ( $< 0.1 \mu\text{m}$ ) crystallites, and a coarser structure characterized by crystallites  $\sim 1-2 \mu\text{m}$  in diameter dispersed within a much finer-grained ( $< 0.1 \mu\text{m}$ ) crystalline matrix. Surface damage was simulated by the Vicker's microhardness technique, with indentations being made over a wide load range to duplicate varying degrees of severity in the contact events. Direct measurement of the indentation flaws was made by calibrated scanning electron microscopy. Fracture toughness values were determined by direct calculation from the indentation parameters. The repropagation of the indentation flaws was investigated by strength tests performed in biaxial flexure.

The results indicated that flaw introduction, as well as strength, fracture toughness, and the magnitude of strength loss sustained from surface damage, were all significantly affected by crack interactions with the crystallites in the glass-ceramic samples. The crack-crystallite interactions were extensive in the coarse microstructure samples. Crack pinning by the dispersed phase crystallites occurred at flaw sizes approximately equal to the mean free path distance between the dispersions, while at larger flaw sizes, crack deflection around the dispersed crystallites took place. Crack-microstructure interactions were absent in these same samples at flaw sizes less than the mean free path distance, and were not observed at all in the original glass or in samples heat-treated to yield only the fine microstructure.

In the coarse microstructure samples, the size of flaws introduced by surface contact was found to be limited by the crack pinning interaction, thus confirming the basic concept of the dispersion-strengthening model for brittle composites. A substantial toughening effect in these same samples was realized from the crack deflection. Fracture toughness for the coarse microstructure samples exhibited a crack size-dependency, with toughness values corresponding to that of the matrix measured at small flaw sizes, and to that of the composite, at larger flaw sizes. The phenomenon was not present in either the original glass or in the fine microstructure samples.

The crack-crystallite interactions occurring in the coarse microstructure samples greatly improved mechanical performance. The com-

combination of decreased flaw size from crack pinning and increased fracture toughness from crack deflection resulted in strength values which were superior to those of the original glass. The crack size-dependent fracture toughness enhanced the ability of the coarse microstructure samples to avoid potential strength losses following surface contact.